Phase-averaged analysis of an oscillating water column wave energy converter

Alan Fleming, BEng (Hons)

National Centre for Maritime Engineering and Hydrodynamics

Australian Maritime College

Submitted in fulfilment of the requirements for the degree of Doctor of Philosophy

University of Tasmania, September 2012

DECLARATIONS

AUTHORITY OF ACCESS

This thesis may be made available for loan and limited copying and communication in accordance with the Copyright Act 1968.

STATEMENT OF ORIGINALITY

This thesis contains no material that has been accepted for a degree or diploma by the University or other institution. To the best of my knowledge and belief, this thesis contains no material previously published or written by another person, except where due acknowledgement is made in the text.

Signed: _____

Alan Fleming

Date:_____

STATEMENT OF CO-AUTHORSHIP

Chapters 2-4 of this thesis have been prepared as scientific papers. In all cases experimental design, experimentation, data analysis and interpretation, and manuscript preparation were the primary responsibility of the candidate. However work was performed in collaboration with supervisors and co-authors. Details of contributions are outlined below:

Chapter 2 (paper 1)

(Phase-averaged flow analysis in an oscillating water column wave energy converter)

Laurie Goldsworthy provided technical knowledge and support in PIV experimental setup, acquisition and post-processing. Gregor Macfarlane provided testing facility support and manuscript preparation assistance. Tom Denniss provided intellectual property. Irene Penesis and Neil Bose contributed to data interpretation and manuscript preparation.

[Candidate 82%, Penesis 4%, Goldsworthy 4%, Macfarlane 4%, Bose 4%, Denniss 2%]

Chapter 3 (paper 2)

(Phase-averaging of velocity fields in an oscillating water column using splines)

Irene Penesis, Gregor Macfarlane and Neil Bose contributed to manuscript preparation and phase-averaging algorithm design. Scott Hunter provided intellectual property.

[Candidate 83%, Penesis 5%, Macfarlane 5%, Bose 5%, Hunter 2%]

Chapter 4 (paper 3)

(Energy balance analysis for an oscillating water column)

Irene Penesis, Gregor Macfarlane and Neil Bose contributed to manuscript preparation and conducted extensive discussions on the energy balance. Tom Denniss contributed intellectual property and valuable feedback.

[Candidate 85%, Penesis 5%, Macfarlane 5%, Bose 3%, Denniss 2%]

We the undersigned agree with the above stated "proportion of work undertaken" for each of the above published (or submitted) peer-reviewed manuscripts contributing to this thesis:

Signed: _____ _____

Dr Irene Penesis	Assoc. Prof. Giles Thomas
Supervisor	Acting Director
National Centre for Maritime Engineering and Hydrodynamics	National Centre for Maritime Engineering and Hydrodynamics
University of Tasmania	University of Tasmania

Date:_____

ACKNOWLEDGEMENTS

Firstly I thank my supervisors (Neil Bose, Irene Penesis and Gregor Macfarlane) who provided me the direction necessary to win the initial scholarship to begin my study as a PhD candidate and finish my candidature in the three and a half years permitted by the University of Tasmania (UTAS).

I appreciate not only the latitude they gave me but also their guidance in bringing me back on course when I ventured too far off topic. I thank them for identifying future opportunities and apply for and winning an Australian Research Council (ARC) Linkage grant which (all going to plan) will provide me with post-doctoral employment.

I thank Scott Hunter and Tom Denniss from Oceanlinx for financial support and technical discussions. I also acknowledge that this research was partially supported by the ARC Linkage grant [LP110200129].

I thank Trevor Lewis for providing technical advice regarding surfactants, and the generous loan of laboratory facilities and equipment (some of which did not survive my experimental methodology) that enabled the manufacture of sufficient fluorescing particles necessary to complete PIV experimentation.

I thank Laurie Goldsworthy for the loan of fragile PIV equipment and also for his assistance with PIV calibration, acquisition and post-processing. Without his expertise I am sure the PIV data would have been far less reliable.

I thank the AMC towing tank technical support staff for 'getting the job done' by using initiative to provide solutions to sometimes vague requests. In particular I thank Tim Lilienthal for his assistance in data acquisition and complying with my demanding experimental schedule without complaint.

Finally I thank my family for their support. My mother Ann– thanks for the care packages of delicious fruit cake and chili sauce. My father Keith - thanks for technical advice and the occasional proof-read. Sonia, Jason and the boys (Oscar and Floyd) thanks for the distractions necessary to maintain my sanity and wellbeing.

ABSTRACT

The work described in this thesis is concerned with the application of phase-averaging to experimental data obtained for a forward-facing bent-duct oscillating water column (OWC) wave energy converter. Experiments were performed on a three-dimensional model of the OWC in monochromatic waves. The research includes the development of new curve-fitting and ensemble-averaging phase-averaging algorithms designed to phase-average two-dimensional particle-imaging velocimetry (PIV) data. The phase-averaged PIV velocity fields were then used for qualitative and quantitative analysis. Qualitatively - visualisation of the velocity fields as vectors over a wave cycle shows the average flow field phenomena including bulk flow, water column slosh, front wall swash and downwash, vortices and an outflow jet. Quantitatively – two-dimensional kinetic energy and vorticity was calculated from the phase-averaged velocity fields and used in an energy balance analysis.

Experimental and theoretical data were combined in an energy balance analysis of the OWC to map the flow of energy from the incoming waves to intermediate stores and finally to sinks, which importantly permits the inclusion of non-linear phenomena. Using the energy model it was found that for the OWC model tested that the phase-averaged energy dissipated by the power-take-off was greater during water outflow than during water inflow. Phase-averaged experimental analysis of OWCs is an additional tool suitable for the design of underwater geometry of OWCs with potential application to other wave energy converters.

TABLE OF CONTENTS

LIST OF FIGURES

LIST OF TABLES

ABBREVIATIONS

2D	Two-dimensional
AMC	Australian Maritime College
ARC	Australian Research Council
BBDB	Backward bent-duct buoy
CCD	Charge coupled device (digital camera)
CFD	Computational fluid dynamics
FFT	Fast Fourier Transform
FOV	Field of view
ITTC	International Towing Tank Conference
OWC	Oscillating water column
PIV	Particle imaging velocimetry
PTO	Power-take-off
RMS	Root mean squared
SG	Specific gravity
UTAS	University of Tasmania
WEC	Wave energy converter

NOMENCLATURE

$C_{balance}$	Balance type conditioner
$C_{distribution}$	Distribution type conditioner
C_{x_i}	Conditioner, an array with a mean of Unity
C_g	Wave group celerity (m/s)
dx	Phase interval, (s)
dx	Pixel width (mm)
dy	Pixel height (mm)
E_t	Total kinetic energy (J/m)
f	Wave frequency (Hz)
$frames$	Number of velocity fields in a set
H	Wave height (m)
k	Wave number (m^{-1})
M	Slope
n	Number of independent data points/ Number of elements in an array
nx	Number of vertical pixels in an image/velocity field (height)
ny	Number of horizontal pixels in an image/velocity field (width)
p	Phase array of shape $(frames)$ $\left(\frac{t}{T}\right)$
t	Time (s)
t_{image}	Time image recorded
t_{zero}	Time of zero crossing of immediate wave
t_{zero+1}	Time of zero crossing of end of immediate wave
T	Wave period (s)
$u(x_i)$	Standard uncertainty
u_{E_t}	Uncertainty of total kinetic energy (J/m)
$u_{RMS_{(x,y)}}$	RMS uncertainty calculated by DaVis (velocity field) (m/s)
u_u	Combined uncertainty of PIV velocity (m/s)
$\bar{u}_{v_x}$	Average uncertainty in x velocity component (m/s)
$\bar{u}_{v_y}$	Average uncertainty in y velocity component (m/s)
v	Velocity field array of shape $(frames, ny, nx)$ (m/s)
V_{avg}	Average velocity of a set of velocities, (m/s)
V_{RMS}	Root-mean-squared deviation of velocity of a set of velocities, (m/s)
V_x	Horizontal velocity component, (m/s)
V_{xi}	Horizontal velocity component at pixel position i, (m/s)
$V_{(x,y)}$	Velocity field array of shape (x, y) (m/s)
V_y	Vertical velocity component, (m/s)
V_{yi}	Vertical velocity component at pixel position i, (m/s)

w	Weighting array
w_c	Weighting array with conditioners applied
W	Model width (m)
x	Horizontal position (mm)
y	Vertical position (mm)
γ	Angular phase
γ_{FH}	First harmonic phase shift
∇	Volumetric flow rate of air through orifice
ϵ	Viscous dissipation (W/m)
λ	Wave length (m)
ρ_w	Water density (kgm-^{3})
ω	Wave phase (rads^{-1})

1

GENERAL INTRODUCTION

"The world's energy system is at a crossroads. Current global trends in energy supply and consumption are patently unsustainable — environmentally, economically, socially. But that can — and must — be altered; there's still time to change the road we're on."

(International Energy Agency, 2008)

Ever since the oil crisis of the 1970s there has been increasing demand for the development of renewable energy technology including – ocean renewable energy (Palmer, 2008). Ocean waves are a concentrated form of solar energy and presently mostly untapped renewable energy resource. The average power flux for wave energy is 2-3 kW/m^2 compared to 0.1-0.3kW/m^2 for solar energy (Falnes, 2007). The development of ocean renewable technology is considered to be lagging wind energy by approximately ten to fifteen years (Mueller and Wallace, 2008). However, unlike how wind energy technology converged on a single solution (the three bladed horizontal axis turbine) wave energy is not expected to converge on a single solution (Cruz, 2008). There already exist hundreds of patents for different designs of wave energy devices and also many books and reviews on the current status of wave energy (Clément *et al*., 2002; Brooke, 2003; Falnes, 2007; Cruz, 2008; Palmer, 2008; Aqua-RET, 2009).

Wave energy converters are classified by both their location and principal mode of extraction (EMEC, 2009). Locations include: onshore, near-shore and offshore. The principal modes of extraction types are (EMEC, 2009):

- Attenuator (Figure 1.1 upper left) – arranged parallel to the direction of wave propagation. Differences in buoyance cause bending moments which are extracted by a power-take-off

- Point absorber (Figure 1.1 upper right) – relative movement caused by wave action between a floating structure and other reference point is extracted by a power-take-off;

- Oscillating wave surge converter (Figure 1.1 centre left) – Surge in water waves activates this device, best utilised in intermediate to shallow water where wave surge is increased relative to heave;

- Oscillating water column (Figure 1.1 centre right) – Analogous to a blowhole, the wave action causes the flow of air through a bi-directional turbine (the power-take-off);

- Overtopping (Figure 1.1 lower left) – water from the waves overtop the device and is temporarily stored as potential energy in a reservoir on the device. The energy is extracted via low head turbines.

- Submerged pressure differential (Figure 1.1 lower right) – a submerged device utilises differences in pressure induced by the passing wave to extract energy;

- Other – other unique designs which do not fall into the above categories.

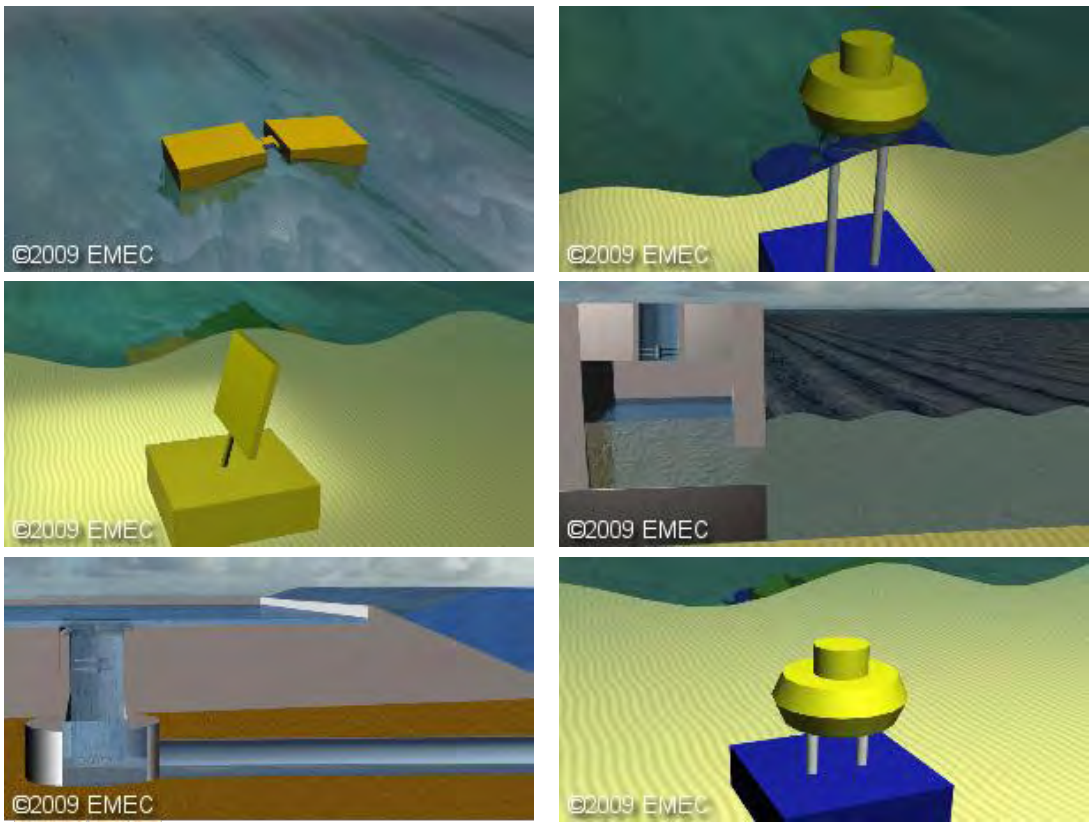

Figure 1.1 Wave energy converter modes of operation, reproduced with permission (EMEC, 2009)

The Oscillating Water Column (OWC) device is the subject of this research and is one of the most extensively studied types of wave energy converters. The OWC is heavily studied due to the perceived advantage of having a single moving part, the turbine, which is mounted above the water - clear from the corrosive seawater, providing easier access for maintenance and longevity of components.

The operation of OWCs has been demonstrated at full and large scale for several OWC designs (eg. PICO, LIMPET, Energex/Oceanlinx). However the devices are still in the prototype stage and still require optimisation. One way to improve operational efficiency of OWCs is to optimise the underwater geometry. The underwater geometry is important in the operational efficiency of an OWC since there is direct interaction between the incoming wave field and the water contained in the OWC. Obtaining quality flow field information inside and around the OWC for this purpose is non-trivial due to the presence of non-linear phenomena and oscillating flow. Computational fluid dynamics (CFD) is a mature means of obtaining flow field information but still requires validation through experimentation.

This research was motivated by collaboration between the Australian Maritime College and Oceanlinx, an Australian based wave energy company. The objective was to address some perceived deficiencies around model testing of wave energy devices, specifically models of OWC's with geometry of interest to Oceanlinx.

Model test experimentation remains an important tool in the development of wave energy converters due to the complicated nature of real world condition (Cruz, 2008). Two-dimensional particle imaging velocimetry (PIV) is an optical based experimental technique for obtaining quantitative spatial flow field information in a plane (Schröder, Andreas and Willert, 2008). 2D PIV is a mature technology with multiple commercial solutions available. Even though the technology is mature and has been applied in hydrodynamic research extensively (Felice and Pereira, 2008), there still remain several hurdles precluding the common use of PIV (2D or otherwise) in model test experiments including:

- Relatively high equipment costs
- Additional safety requirements (the method involves the use of a high intensity laser [class 4 laser] easily capable of causing blindness)
- Considerations in experimental design
    - Require optical access for both a laser sheet and camera requiring that the model is optically transparent in those directions
    - Positioning of the model to allow optical access and calibration of PIV equipment
    - Lower rates of data acquisition/test turnover
    - Large data storage requirement and additional post processing of data

Once the hurdles to conducting PIV tests have been addressed the experimental outcomes from acquiring PIV data are rewarding. Velocity vector representation of velocity fields provides a powerful visualisation tool which gives the experimenter valuable insight into complex fluid structure interaction. PIV is particularly useful for flow visualisation in reversing/oscillating flow where steady flow visualisation techniques cannot be used (Müller and Whittaker, 1995). The velocity fields can also be used for CFD validation and quantitative analysis. The spatial averaging due to the PIV post-processing must be duly considered when using such results.

The main research questions for this thesis were:

- How can 2D PIV be applied in the design of wave energy converter underwater geometry design?
- How can the velocity fields be used in the design and performance assessment of OWC's?

The aim of this thesis is to present phase averaged experimental data for a model of a forward-facing bent-duct OWC and to use the data in an energy balance analysis. The experimental analysis obtained the following types of data for four different monochromatic wave frequencies (f=0.44, 0.50, 0.57, 0.77Hz) at a wave height of H = 0.07m which was acquired in a single experimental series of three week duration:

- Two-dimensional PIV data at the centreline plane of the OWC (at seven different positions)
- An array of wave probe data inside the OWC chamber
- Air pressure inside the OWC

This thesis is in *chapterised* format meaning that the chapter may have been published elsewhere. Where the chapter has been published it is clearly indicated on the first page of the chapter. The chapter body is then the most recent version provided for publication. The structure of the thesis is as follows:

- Chapter 2 provides details on the PIV experimentation of the OWC and presents some initial results.
- Chapter 3 presents a curve-fitting phase-averaging method using splines which was developed in response to the nature of the data collected during experimentation. Additional velocity fields are presented using the new phase-averaging technique.
- Chapter 4 utilises the phase-averaged velocity fields calculated using Chapter 3 to conduct an energy balance assessment for the wave energy converter. The energy sources, stores and sinks in the wave energy conversion process are considered.
- Chapter 5 presents a further phase-averaging hybrid ensemble-averaging method which was developed to conduct an error analysis of the curve-fitting method presented in Chapter 3.
- Chapter 6 states the main conclusions and provides some ideas for further work.
- Uncertainty analysis corresponding to Chapter 2 is provided in Appendix A.
- A complete set of phase-averaged velocity fields are provided in Appendix B for the four wave conditions tested.

2

PHASE-AVERAGED FLOW ANALYSIS IN AN OSCILLATING WATER COLUMN WAVE ENERGY CONVERTER

This chapter was originally presented as a paper at OMAE 2011 by the candidate (Fleming *et al*., 2011) and has been accepted for publication in the *Journal of Offshore Mechanics and Arctic Engineering*. This chapter is the first revision of the OMAE conference paper which has been submitted for further review based on reviewers' comments provided by the *Journal of Offshore Mechanics and Arctic Engineering*.

The citation for the conference paper is:

Fleming, A., Penesis, I., Goldsworthy, L., Macfarlane, G., Bose, N., Denniss, T., 2011. Phase-averaged Flow Analysis in an Oscillating Water Column Wave Energy Converter, in: Proceedings of the ASME 2011 30th International Conference on Ocean, Offshore and Arctic Engineering (OMAE 2011). Rotterdam, The Netherlands.

The conference paper has also been cited in Chapters 3 and 4.

ABSTRACT

This paper presents the application of phase-averaging to experimental data obtained during scale model testing of a forward-facing bent-duct oscillating water column (OWC). Phase-averaging is applied to both wave probe data and a two-dimensional velocity field at the centreline plane of the OWC model obtained using PIV. Results are presented for one monochromatic wave condition. The influence of varied wave frequency is briefly discussed.

INTRODUCTION

The oscillating water column (OWC) is a wave energy conversion device which at its simplest consists of a wall which penetrates the sea surface to form a chamber. Air enclosed by the chamber and the free surface is connected to the atmosphere via a bi-directional turbine (commonly a Wells turbine). The water inside the chamber oscillates due to external wave action which in-turn causes the air to flow in and out of the chamber via the turbine.

Generally, experimental studies to assess the performance of a scale model of OWC geometry involve monitoring the chamber air pressure and water levels to determine the rate of air flow passing through an orifice due to the wave action on the OWC. Mean power of the air flow can be calculated and compared with the incoming wave power as an assessment of the performance of the OWC. The analysis has been done in both regular and irregular seas.

Non-experimental design of OWC geometry commonly uses the following tools: numerical modeling (mass damper model, often based on linear theory), and computational fluid dynamics (CFD). Experimentally valuable flow field information can be obtained using optical techniques.

Müller and Whittaker (1995) performed flow visualization on a 1/36 scale two-dimensional model of the Islay OWC prototype. The flow was visualized by introducing heat-treated polystyrene beads (diameters of 0.25mm - 0.35mm and SG of ~ 1.0) and images were recorded on photographic film. They observed important phenomena including front wall swash and down-wash, and water column slosh. They concluded that significant losses occurred in vortices generated by the sharp edges of the front lip.

Folley and Whittaker (2002) performed further flow visualization experiments on a 1/40 scale two-dimensional model of the LIMPET shoreline OWC (the 2nd full scale OWC built on the island of Islay) with modified geometry based on the results of their first test (Müller and Whittaker, 1995). The modifications included a rounded front lip and sloping back wall. They used colored water to provide a contrast so that the free-surface and entrained air could be identified. They presented an energy distribution model which outlined the transformation and distribution of energy between the incoming wave and all other considered energy sources and sinks and suggested that viscous dissipation might be a significant loss.

Standard particle imaging velocimetry (PIV) is an optical technique which provides two-dimensional velocity flow field information in a plane. When applied to experimental analysis of OWCs it can be used to reveal phenomena associated with the transformation of the oscillatory flow of the wave, to the two-dimensional (or near two-dimensional) oscillation of the free surface within the OWC.

The first known application of PIV to the study of flow in an OWC was by Morrison (1995). The experimentation was performed on a simplified scale model of an onshore type OWC in a purpose built wave tank at the University of Belfast. Using state of the art PIV techniques the 2D velocity field was obtained for an arbitrary measurement window centered on the front lip of the OWC. Assuming two-dimensional flow Morrison calculated the kinetic energy and dissipation of the flow through the opening of the OWC model. Morrison found the viscous dissipation rate to be significant and on average was eight percent of the input wave power.

Graw, Schimmels & Lengricht (2000) performed PIV with a similar experimental setup to Morrison (1995) but at a different model scale. They also investigated geometry changes by varying the lip shape, submersion and angle. They also concluded that dissipation rates were significant.

Imai *et al*. (2008) performed PIV analysis on a floating 2D model of a backward bent-duct buoy (BBDB) and obtained velocity vectors around the mouth of the OWC. The PIV results they presented were for flow visualization purposes only.

The primary purpose of this paper is to:

- Outline the process used in these tests to conduct PIV experiments on a generic OWC;
- Describe the technique used to analyze the experimental data;
- Present and discuss a limited number of the results;
- Show that this data may be used to investigate the energy transfer within an OWC.

EXPERIMENTAL METHODOLOGY

The experiments were conducted in the Towing Tank at the Australian Maritime College (National Centre for Maritime Engineering and Hydrodynamics) Launceston, Tasmania, Australia. The facility is 3.5m wide, 1.5m deep and 100m long. Waves were generated with a bottom hinged hydraulically driven wave paddle.

The tests were conducted on a model of a generic forward-facing bent-duct OWC (the profile of the geometry can be seen in Figure 2.3). The water surface profile inside the chamber was recorded with an array of copper strip and stainless steel wire resistance type wave probes monitored by Churchill Controls wave probe monitors; the arrangement of the wave probes inside the OWC chamber is shown in Figure 2.2. The model was made from 6mm clear acrylic sheet to provide optical access for the PIV equipment.

A phase wave probe was also mounted in line with the front face of the OWC, but offset to avoid disturbed flow induced by the model (position shown in Figure 2.1). The intersection of the front face of the OWC and the waterline is taken as the datum and direction of wave

propagation is always from the right corresponding to the physical experimental setup. Experimental data was obtained for four different monochromatic wave conditions, all with a nominal height of 0.07m, the wave frequencies were 0.44Hz, 0.50Hz, 0.57Hz and 0.77Hz. The results presented in this paper refer to the 0.44Hz frequency wave unless otherwise specified. The wave frequencies selected span the expected operational frequency and the wave height is a typical operational height. The power-take-off was simulated by an orifice plate as recommended by Folley and Whittaker (2002). The orifice diameter was 58mm.

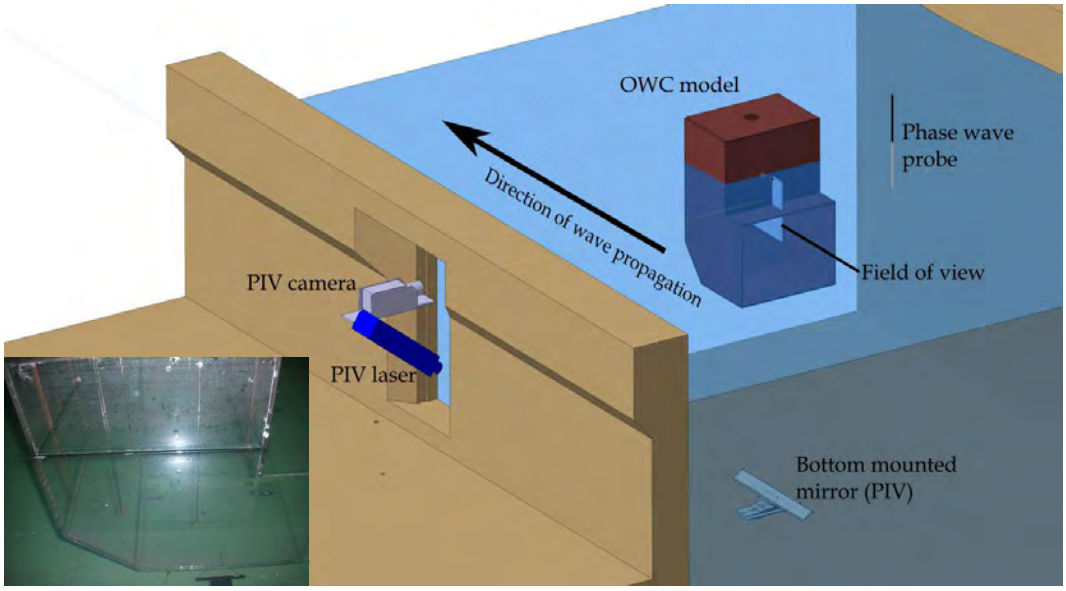

Figure 2.1 Experimental setup including PIV apparatus mounted in front of the window of the towing tank. Lower left is a photograph of the model in situ; the bottom mounted mirror is the dark shape below the model.

Two-dimensional PIV data was obtained with a commercial system provided by LaVision GmbH consisting of a double pulsed Nd:YAG laser with an energy of 120mJ per pulse (New Wave Solo 120) and a LaVision Imager Intense dual frame, 12bit CCD camera, with 1376×1024 pixels. The light sheet was generated by expanding the laser beam with a cylindrical lens attached to the front of the laser. The light sheet was directed through a quartz insert mounted in the window in the side of the towing tank and then deflected into the vertical plane off a front surface mirror mounted on the floor of the towing tank. The light sheet was aligned with the centerline plane of the OWC orthogonal to the direction of wave propagation for the duration of the tests. The CCD was fitted with a 35mm lens which provided a field of view (FOV) of 345mm×256mm. During testing the FOV was varied between seven different positions (for all wave conditions) to cover the entire chamber and entrance of the OWC as shown in Figure 2.3.

Seeding particles were self-produced consisting of Carnauba wax doped with Rhodamine 6G following a method adapted from Turney *et al.* (2009). Seeding was performed by premixing the particles in a 100 liter tank using a circulating pump and introducing the seeded water into

OWC model. PIV Calibration was achieved by inserting a calibration plate at the centerline of the model. Further details on PIV calibration and PIV data post-processing are provided in Table 3.2.

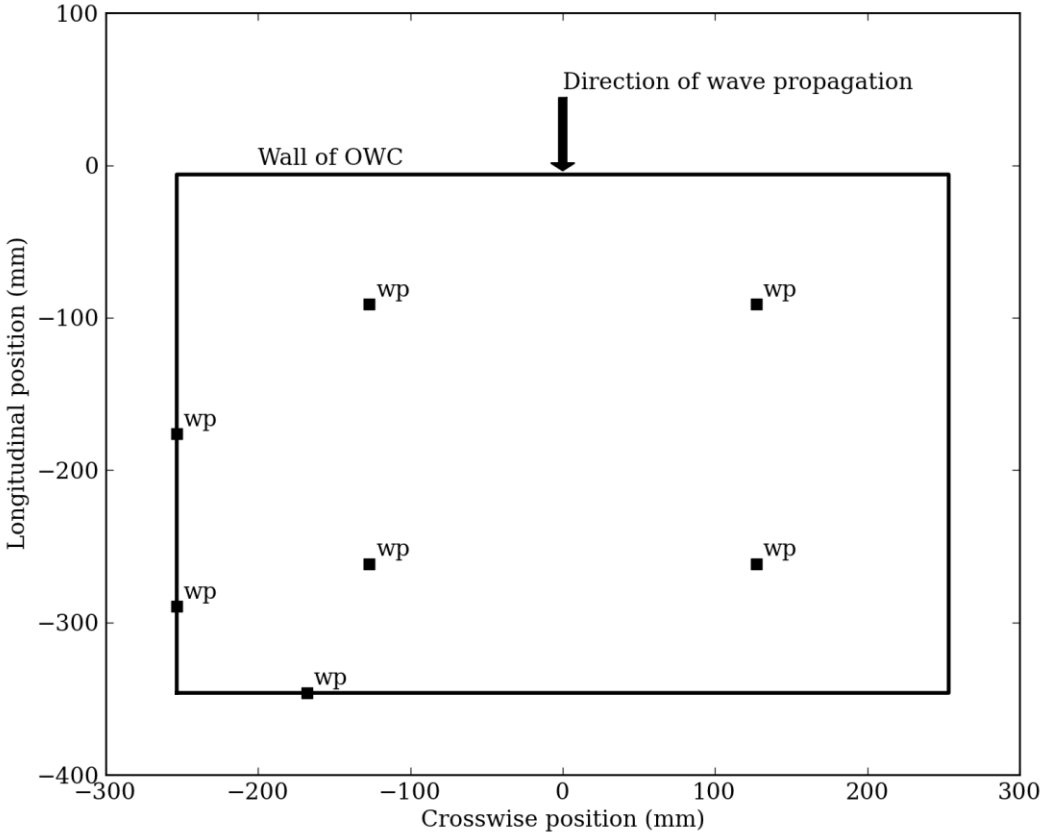

Figure 2.2 Location of wave probes inside OWC chamber (looking down) with waves approaching from the top

Each run involved the following procedure: Step 1 - water seeded with particles, step 2 - particle seeding density verified with the PIV system, step 3 - wave maker initiated and step 4 - data recorded. For a typical run up to 200 image pairs were obtained at a rate of up to 5Hz. The recording duration was limited to about one minute due to wave reflections from the beach at the far end of the tank. Runs were repeated to capture sufficient images expected to produce statistically reliable results.

DATA REDUCTION

Due to hardware limitations it was not possible to acquire data at a rate necessary to conduct temporal analysis (from observation the image acquisition rate would need to be approximately 100Hz in single frame mode), hence the analysis of the PIV data was analyzed by phase-averaging. To perform phase-averaging it is necessary that the flow field is cyclic; the profile of

both the incident waves and those within the OWC were acquired using wave probes. Inspection of these records confirmed that both were inherently cyclic.

Phase-averaging is an analysis procedure by which time series data is reduced into phases and frequencies. Phase-averaging is commonly applied in the analysis of PIV results (for an extensive list of phase-averaged PIV papers see Longo *et al*. (2007)). Simple time series reduction of monochromatic data is based on the following assumptions:

- Data is monochromatic
- Each cycle is sufficiently *similar* to adjacent cycles
- The wave frequency is the average of the individual cycle frequencies ($\frac{1}{T}$)
- All experimental phenomena are *phase locked* (oscillate at the same frequency or multiples thereof).

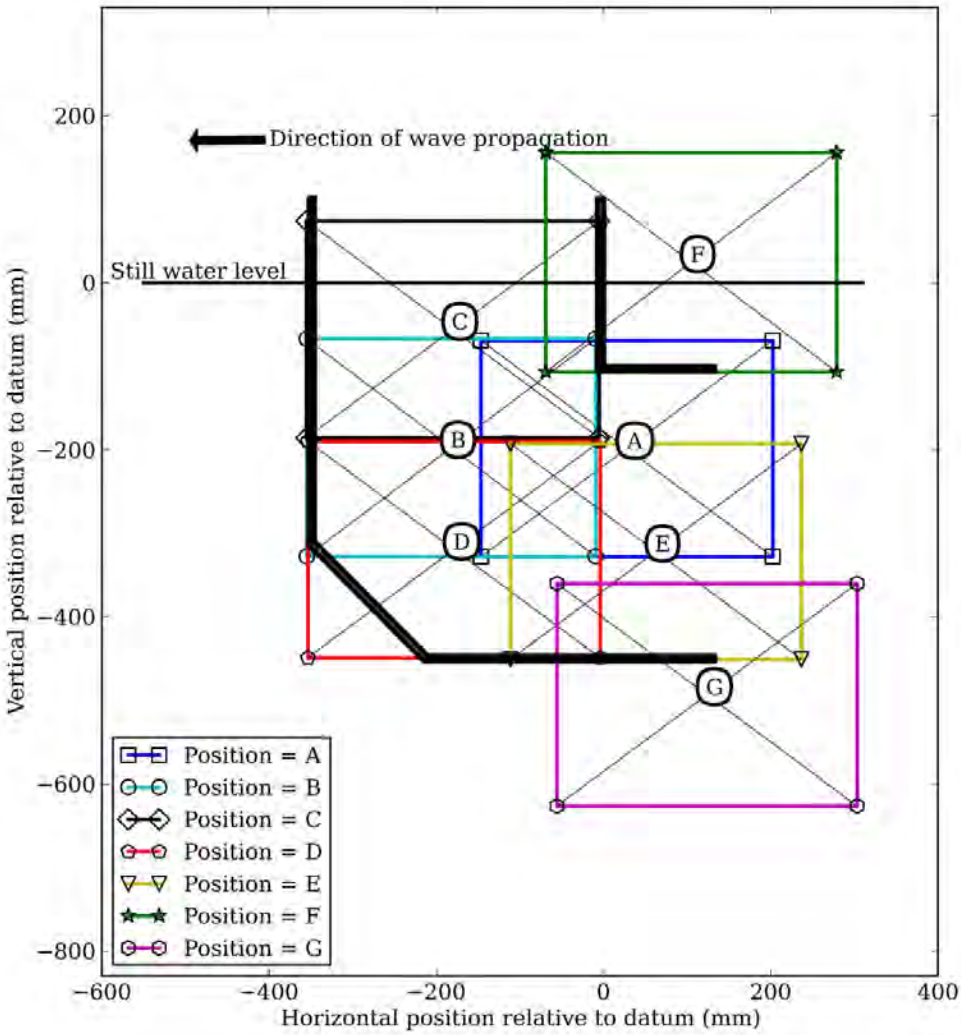

Figure 2.3 Locations of different FOV for PIV data acquisition during experiment, all positions were obtained for all wave conditions.

The time of the time-series data is non-dimensionalized by substituting the actual time with a phase ($\frac{t}{T}$) which is illustrated in Figure 2.4 and described by the following process:

1. The time series is divided into segments of repeating cycles (typical methods common to ocean engineering include zero-up-crossing and peak-to-peak).
2. The phase of a data point is allocated by subtracting the previous adjacent zero-up-crossing time and dividing by the current wave period.

$$\frac{t}{T} = \frac{T_{image} - T_{zero}}{T_{zero+1} - T_{zero}}, where\ 0 < \frac{t}{T} \leq 1 \tag{2.1}$$

In linear theory the wave profile can be written as:

$$\eta = \frac{H}{2}\cos(kx - \omega t) \tag{2.2}$$

where $k = \frac{2\pi}{\lambda}$ is the wave number, and $\omega = \frac{2\pi}{T}$ is the wave phase. The angular phase is related to wave phase by $\gamma = \omega t$, hence, the phase is found to be $\left(\frac{t}{T}\right) = \frac{\gamma}{2\pi}$.

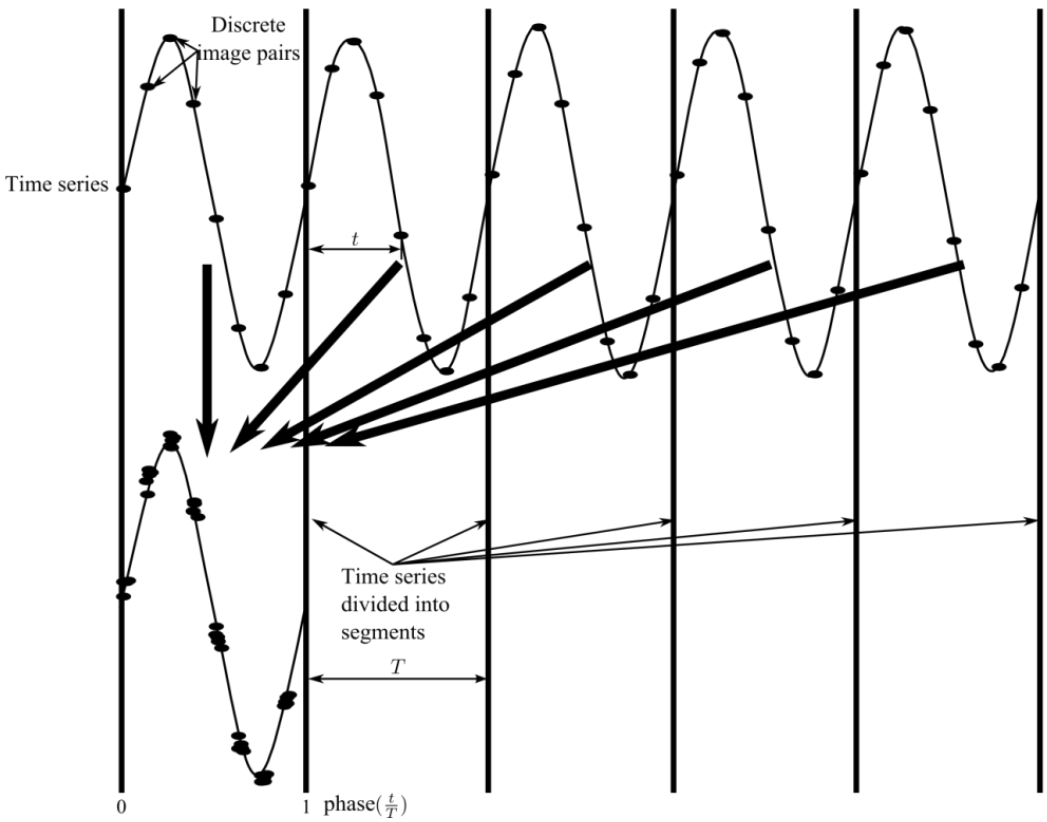

Figure 2.4 Visual representation of the division of time series data into segments for phase-averaging

The phase wave probe (physical position shown in Figure 2.1) data was used as the reference signal for phase-averaging of all synchronized data. Internal wave probes were considered as a synchronizing source, however, the presence of water column slosh meant that on average, the phase wave probe provided the best periodic signal. Phase-averaging data points were limited to data points corresponding to PIV image pairs. The zero-up-crossing method was chosen in preference to the peak-to-peak method since a comparison of the experimental data found that the zero-up-crossing method provided cycle durations with a standard deviation consistently less than the peak-to-peak method. Wave probe data was visually inspected for conformance, inconsistent data was not included in analysis. Furthermore, any test run whose phase wave probe data had a mean wave height outside the range 0.07m $\pm$0.005m was excluded from analysis.

The final step in phase-averaging is to discretize data points to produce common phases (by rounding to the nearest discrete phase) sixteen equally spaced phase divisions between 0 and 1 were used for this test series. All data points with the same phase were then averaged to give the phase-averaged result. An alternate method to discretizing data and averaging is to fit curves to the data by treating the phase as the x-axis and the corresponding magnitude as the y-axis. The curve-fitting process offers the advantage of interpolation in regions of sparse data, but introduces an added complication for the processing of PIV vector files.

RESULTS

Results presented hereafter are phase-averaged unless otherwise specified, furthermore; the data points used for phase-averaging are only those which correspond with a PIV image pair.

The wave probe elevation inside the OWC chamber and the phase wave probe elevation are shown in Figure 2.5. The phase lag in itself is not significant due to dependency on the position of the phase wave probe. The difference in amplitudes however is significant since the amplitude of response is an indication of the 'chamber power'. As can be seen, the mean chamber amplitude is greater than the phase wave probe amplitude.

The profile inside the chamber is shown in Figure 2.6, which was obtained by applying a first order least squares fit to the discrete wave probe elevation which was first interpolated into a regular grid at the centerline plane using a nearest neighbor method. For the 0.44Hz wave there is only a small amount of 'sloshing', sloshing can be defined as the deviation of the surface profile from the horizontal, this supports the commonly used numerical modeling assumption first stated by Evans (1978) which assumed a 'mass-less' piston sits atop the water in the chamber keeping the water surface level.

The surface profiles for the wave frequency f=0.77Hz (Figure 2.7) show a noticeably different story; sloshing is both significant and occurring at twice the frequency of the incoming wave frequency.

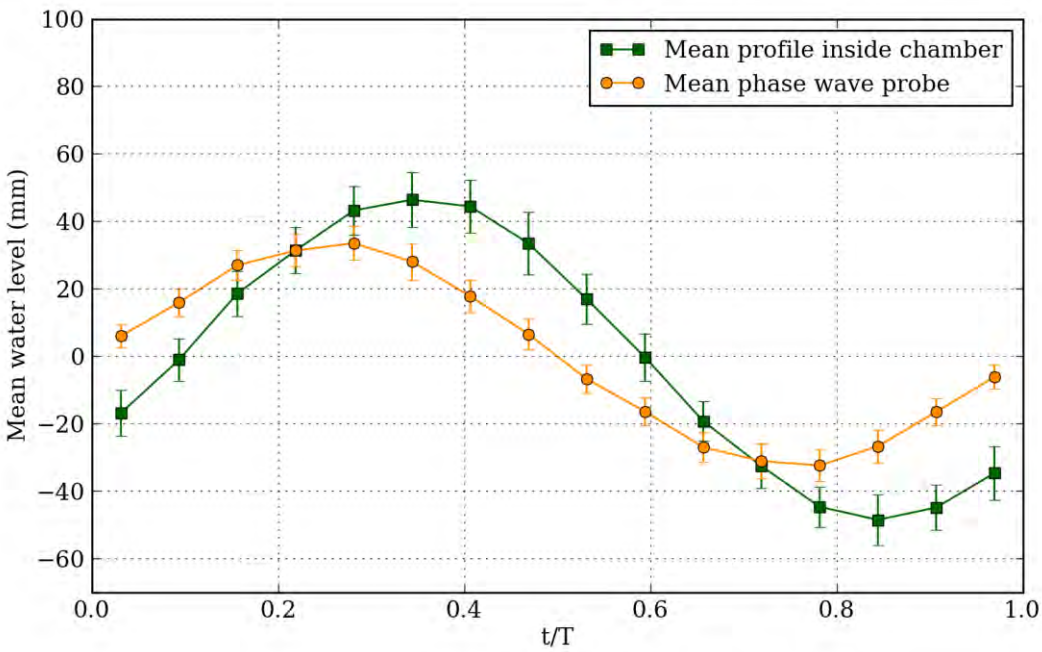

Figure 2.5 Phase-averaged elevations for wave condition H=0.07m and f=0.44Hz, error bars indicate $\pm$ 1 standard deviation (uncertainty) of the corresponding signal.

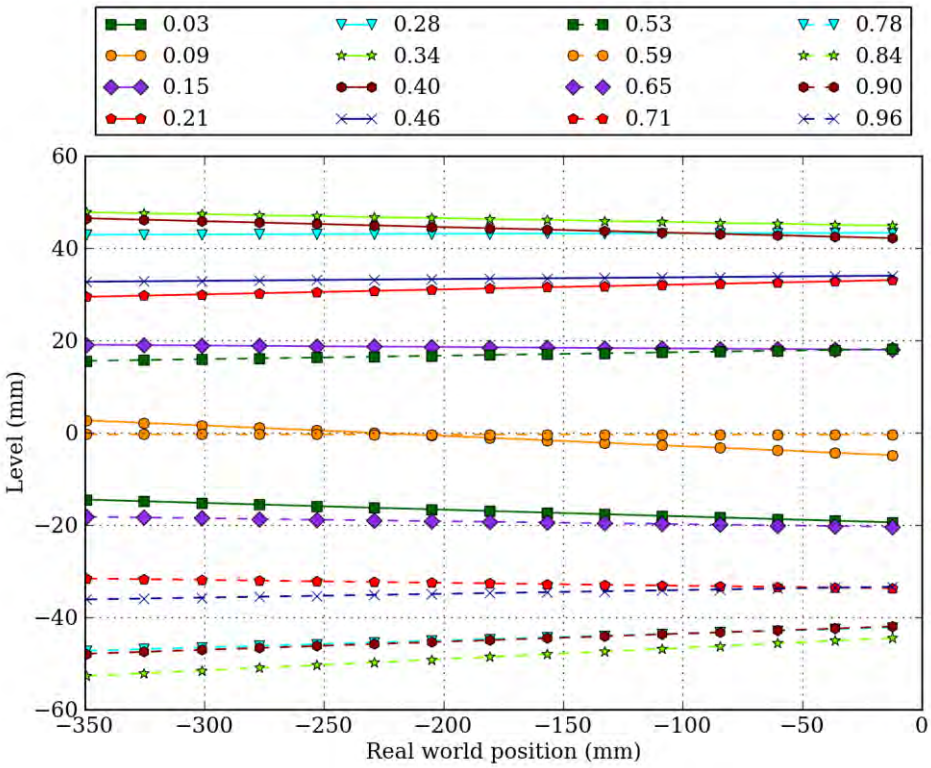

Figure 2.6 Phase-averaged surface profile at the centerline plane inside the OWC chamber for the wave condition *H*=0.07m and *f*=0.44Hz the phase $\left(\frac{t}{T}\right)$ is shown in the legend

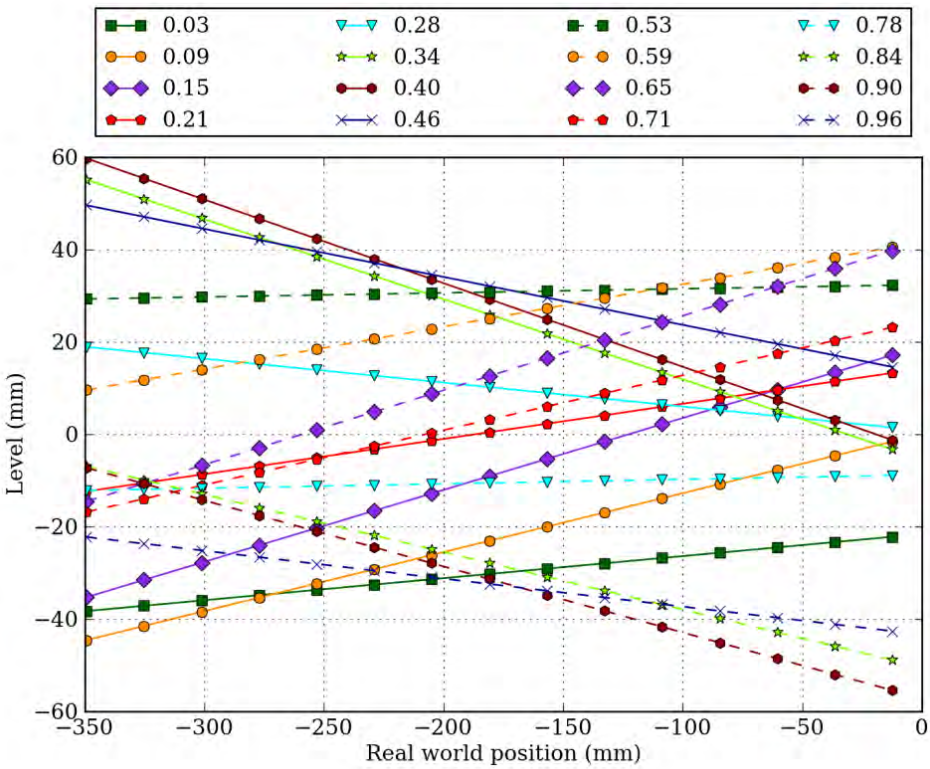

Figure 2.7 Phase-averaged surface profile at the centerline plane inside the OWC chamber for the wave condition *H*=0.07m and *f*=0.77Hz the phase $\left(\frac{t}{T}\right)$ is shown in the legend

THE VELOCITY FIELD

Image pairs were sorted into corresponding folders and then processed using the LaVision PIV software DaVis version 7.2 (2009) to produce velocity vectors for each image pair. The velocity vectors of the same discretized phase were then averaged to produce phase-averaged velocity vectors for an individual position. The phase-averaged velocity vectors from all available positions were merged to produce a patchwork of phase-averaged velocity vectors covering the union of the positions (see Figure 2.3 for positions and Figure 2.8 for an example of the merged velocity field). The phase-averaged velocity field provides a powerful visualization and analytical tool when viewed in an infinitely looping sequence (as an animated gif or video) the bulk flows and other interesting phenomena (at the centerline plane) are plainly visible. A sequence composed of every second phase of the entire phase-averaged velocity field is provided in Figures 2.9 and 2.10, a description of the flow inside the chamber over one wave cycle is now provided:

The description will begin at a transitional stage which has minimal translational velocities both into and out of the chamber; this occurs at approximately $\frac{t}{T} = 0.84$ and is reflected in Figure 2.5 which can be recognized as the minima of the mean water elevation inside the OWC chamber. Significant flow can be observed past the lower lip upward and to the right which will inevitably form a vortex since the flow is past a sharp lip (visible in Figure 2.10(c & d)). The remainder of outflow at the upper lip curls around the upper side of the top lip as it interacts with the inward flow field imposed by the wave flow field; resulting in a low intensity swirling flow above the upper lip.

$\frac{t}{T} = 0.03$ (Figure 2.9(a)): The vortex at the lower lip continues to build and strengthen as inflow continues into the device (maximum vorticity=$18s^{-1}$). Flow past the forward corner of the chamber (behind the upper lip) begins to form a clockwise rotating vortex ($-12s^{-1}$).

$\frac{t}{T} = 0.28$ (Figure 2.9(c)): Inflow is just past the maximum (Figure 2.5) and the clockwise vortex at the forward corner is now fully established ($-15s^{-1}$), the anti-clockwise rotating vortex at the lower lip begins to migrate to the right.

$\frac{t}{T} = 0.41$ (Figure 2.9(d)): Inflow has finished outflow is beginning. The anti-clockwise vortex at the lower lip has migrated further to the right and is contributing to an outflow jet and a clockwise rotating vortex ($-14s^{-1}$) below the lower lip. The clockwise vortex at the forward corner of the chamber has diminished significantly and is positioned so that that its rotation is partially contributing to outflow. Wave reflection off the front face of the OWC generates flow above the front lip in the same direction as outflow; the flow above the lip exceeds the flow

below the lip resulting in the generation of a relatively small clockwise rotating vortex below the upper lip.

$\frac{t}{T} = 0.53$ (Figure 2.10(a)): Outflow is now well established and the anti-clockwise rotating vortex at the lower lip has virtually transformed entirely into the outflow jet and clockwise rotating vortex below the lower lip. Flow past the forward corner of the chamber begins to separate and form a low intensity anti-clockwise rotating vortex which curls along the upper lip migrating to the right with outflow. Outflow above and below the top lip equalizes causing the clockwise vortex located below the top lip to translate with the outflow.

$\frac{t}{T} = 0.66$ (Figure 2.10(b)): The majority of outflow is passing through the upper half of the opening. The clockwise rotating vortex below the lower lip is maintaining position. Flow is beginning below the lower lip toward the right.

$\frac{t}{T} = 0.78$ (Figure 2.10(c)): There is little flow inside the chamber with exception of continued outflow at the upper lip which is combining with the inflow of the subsequent wave. The anti-clockwise rotating vortex below the upper lip is maintaining position. Flow from beneath the lower lip is beginning to curl up in combination with the existing clockwise rotating vortex to begin forming the vortex described at the start of the cycle. The clockwise rotation beneath the lower lip, while contributing to the inflow migrates to the right and upwards.

$\frac{t}{T} = 0.91$ (Figure 2.10(d)): The highest velocity flow of approximately 0.4m/s can be seen at the lower lip as flow is directed upward and to the right (against the direction of wave propagation but in a direction expected in unimpeded water particle motion considering the phase of the wave cycle). Separation at the sharp edged lower lip forms an anti-clockwise rotating vortex (maximum vorticity=$15s^{-1}$) while the majority of flow direction is upwards and inwards.

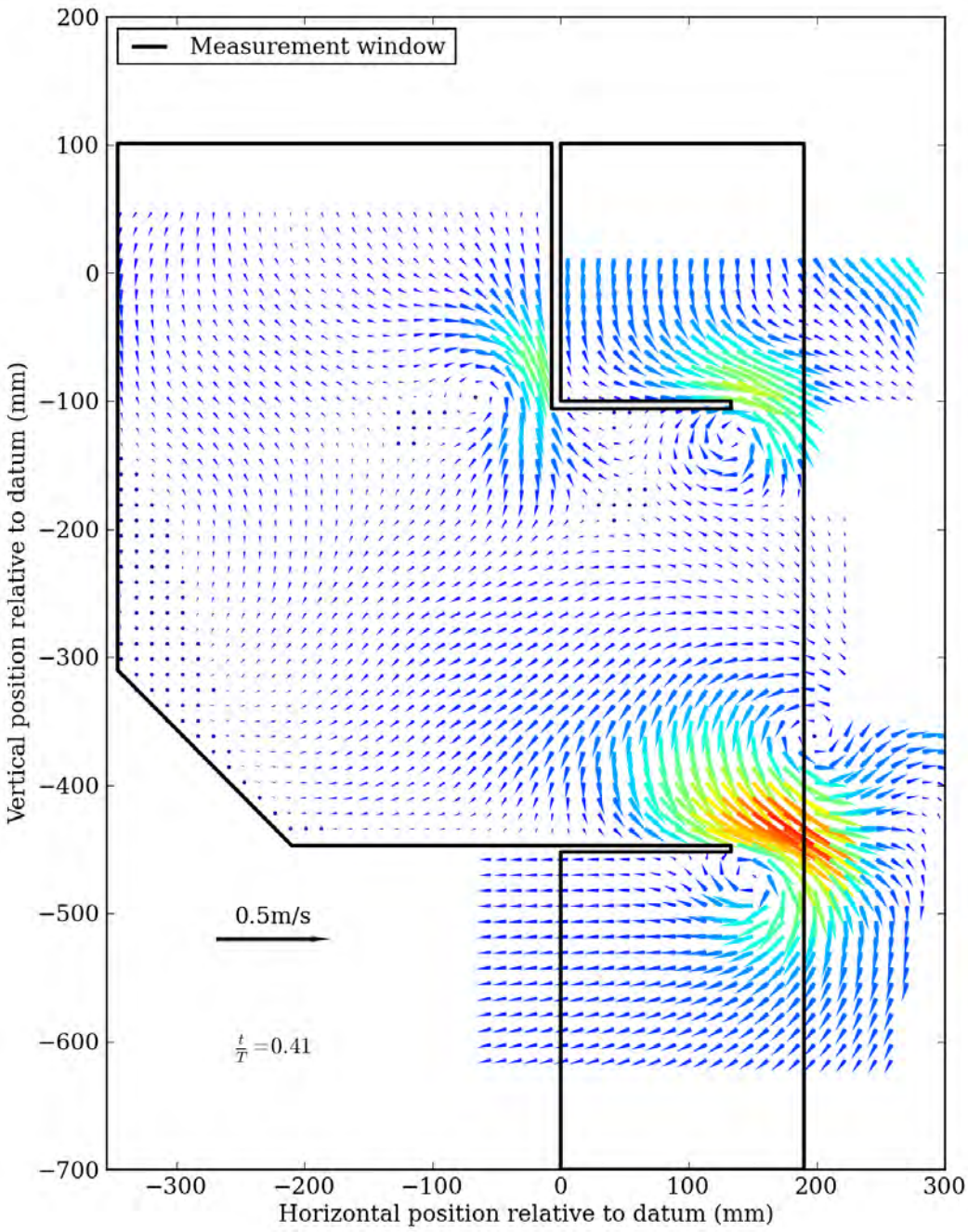

Figure 2.8 Velocity field inside and outside the OWC device with ½ of vectors hidden for clarity (*H*=0.07m and *f*=0.44Hz)

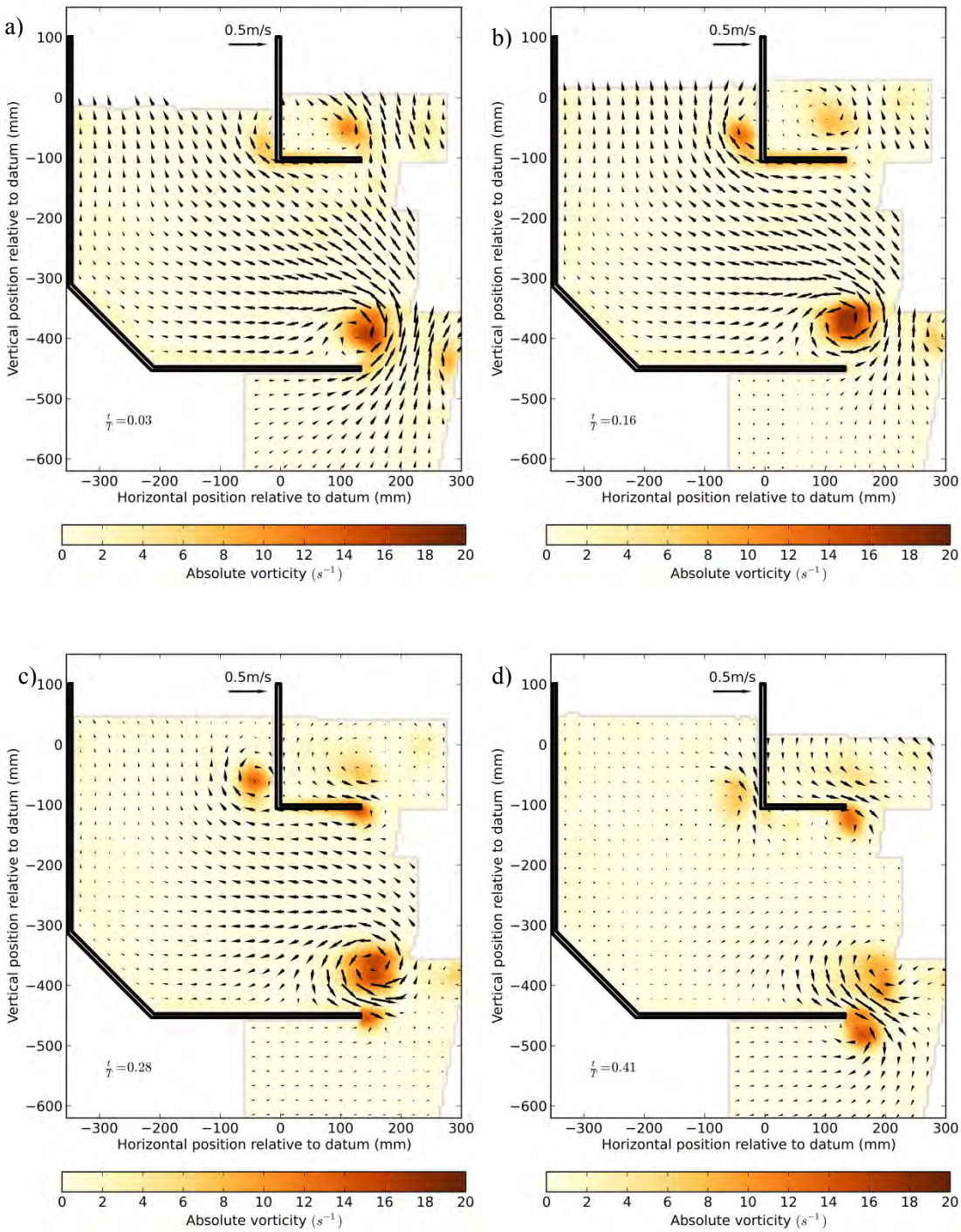

Figure 2.9 Velocity and vorticity field inside and outside the OWC device for the first half of cycle with ¾ of vectors hidden for clarity. (*H*=0.07m and *f*=0.44Hz)

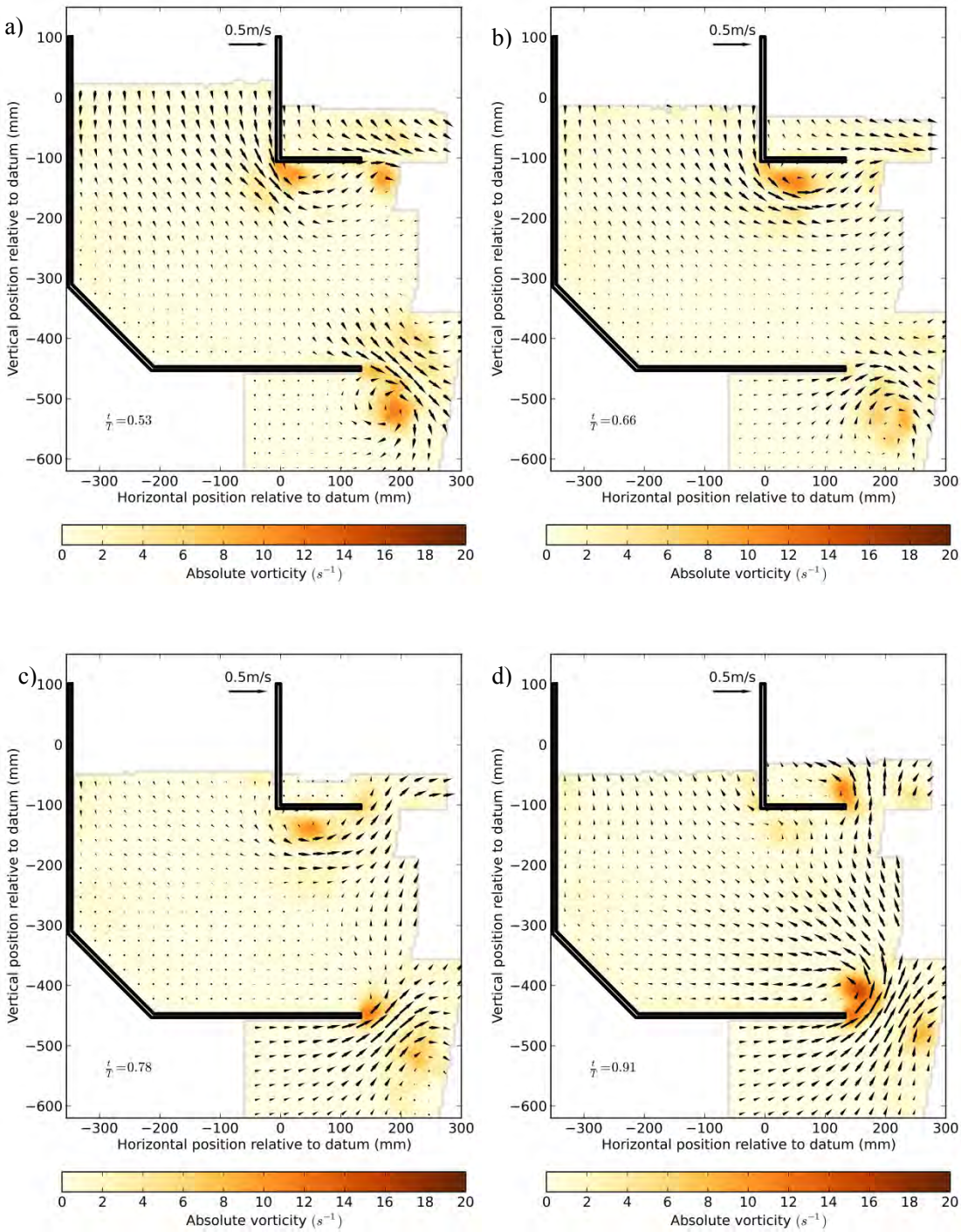

Figure 2.10 Velocity and vorticity field inside and outside the OWC device for the second half of cycle with ¾ of vectors hidden for clarity. (*H*=0.07m and *f*=0.44Hz)

KINETIC ENERGY AND VISCOUS DISSIPATION

Both Morrison (1995) and Graw *et al*. (2000) provide the following formulae for calculation of kinetic energy (3) and viscous dissipation (4) for a 2D velocity field:

$$E_t = \frac{1}{2}\rho_w W \text{ d } \text{ d y} \sum_{x,y} V_{(x,y)}^2 \tag{2.3}$$

$$\epsilon = W \text{ d } \text{ d y } \rho_w \nu \sum_{x,z} \left\{ \left(\frac{\partial V_x}{\partial y} + \frac{\partial V_y}{\partial x} \right)^2 + 2\left[\left(\frac{\partial V_x}{\partial x} \right)^2 + \left(\frac{\partial V_y}{\partial y} \right)^2 \right] \right\} \tag{2.4}$$

where ρ_w is the water density, W is the width of the device dx is pixel width, dy is pixel height, $V_{(x,y)}$ is the component of the of the velocity vector and ν is kinematic viscosity.

For comparison of results it is possible to present results in three different forms: absolute, per unit width (divide both sides by W) and specific (divide both sides by $m = W \text{ dx dy} \rho_w$). Results presented in this paper are per unit width. Results produced from these calculations are highly sensitive to the measurement window.

A velocity field was produced using linear wave theory to simulate water particle motions at the same positions as the experimental velocity field with the same wave height and frequency but without the geometry in place, and is referred to as the undisturbed velocity field. Figure 2.11 shows a comparison of total kinetic energy per unit width of the undisturbed velocity field with the phase-averaged velocity field. Both are restricted to the measurement window which is drawn as an overlay on Figure 2.8.

Observations include:

- There are two peaks for the experimental energy curve where one is significantly larger than the other; the troughs correspond to the minima and maxima of the mean water level inside the chamber shown in Figure 2.5;
- The magnitude of the experimental kinetic energy is on average greater than the magnitude of the undisturbed wave kinetic energy.

Viscous dissipation of the experimental velocity field was calculated by Equation (2.4) with two independent methods used to obtain and verify the calculated strains $\left(\frac{\partial V_i}{\partial j} \text{ with } i \in \{x, y\} \text{ and } j \in \{x, y\}\right)$(LaVision GmbH, 2009). The mean dissipation over one wave cycle is 1.1×10^{-3}W/m and is several orders of magnitude less than the incoming wave energy flux of 12.7W/m (calculated with linear wave theory).

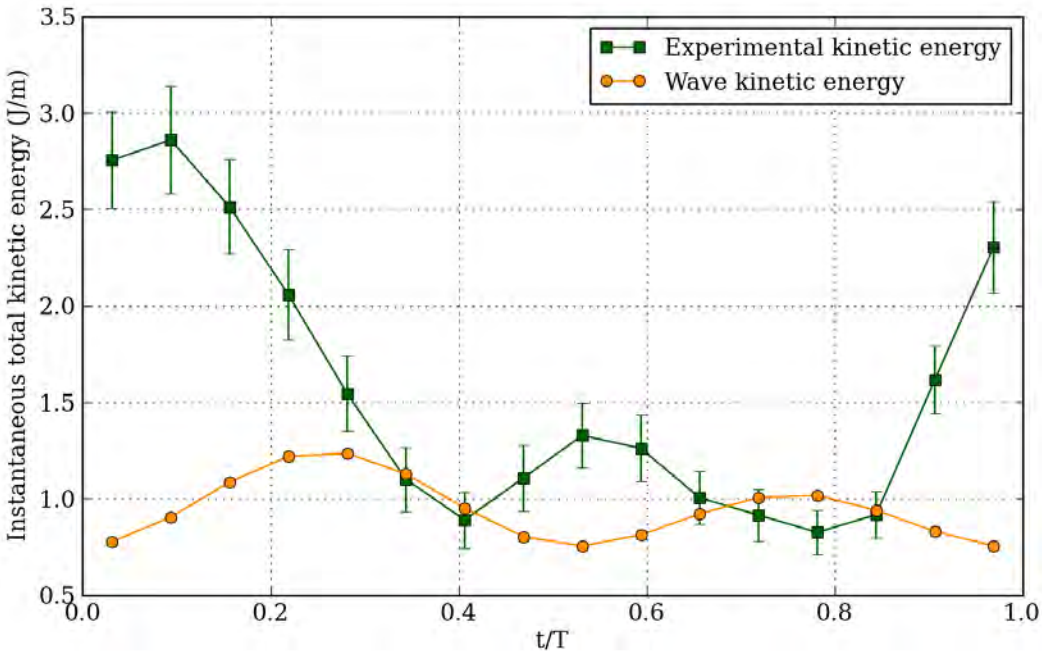

Figure 2.11 Comparison of kinetic energy of an undisturbed flow field with the OWC flow field (*H*=0.07m and *f*=0.44Hz)

UNCERTAINTY ANALYSIS

Uncertainty in the PIV velocity fields was found using the International Towing Tank Conference (ITTC) uncertainty analysis guidelines (ITTC, 2008a) and the procedure for PIV uncertainty assessment (ITTC, 2008b). Uncertainty in the phase-averaged velocity fields was found using:

$$\mathrm{u}_{v_{(x,y)}} = \sqrt{u_u^2 + \left(\frac{k.\,u_{RMS(x,y)}}{\sqrt{n}}\right)^2} \tag{2.5}$$

where $u_u = 4.45$mm/s is type B standard uncertainty in the PIV velocity fields (see Appendix A), $k = 2$ is the coverage factor corresponding to a 95 percent confidence interval, $u_{RMS(x,y)}$ is the RMS velocity fields which were calculated simultaneously with average velocity field using DaVis7.2 and n is the average number of images at the corresponding phase of all positions used to generate the average and RMS results.

The data reduction equation for total kinetic energy is given in Equation (2.3) the uncertainty of the total kinetic energy is the sum of the uncertainty for each pixel. The uncertainties for this analysis are reported in Table 2.1.

DISCUSSION

A major observation is that viscous dissipation is low (virtually negligible) which conflicts with the findings of both Morrison (1995) and Graw *et al*. (2000) who found viscous dissipation to be significant. The possible causes for the discrepancy between findings are:

- The results presented here are phase-averaged;
- The experimental setups may not be geometrically similar enough for a direct comparison (though one might still expect viscous dissipation to be significant);
- The wave height used in Morrison (1995) was 20mm, Graw *et al*. (2000) did not provide a wave height, a wave height of 70mm was used in this experimental series which might indicate that viscous dissipation is more significant for lower amplitude waves (scaling effects are discussed by Cruz (2008)). Also Morrison (1995) reported maximum vorticity of $125s^{-1}$ but a maximum of $18s^{-1}$ was found in this test series;
- Graw *et al*. (2000) provides a method for conversion of kinetic energy to kinetic power (for a measurement window) as follows: "the mean kinetic power is achieved by multiplying the mean kinetic energy with the according frequency", without further description the term 'according frequency' is likely to be interpreted as 'wave frequency', however, further investigation reveals that the according frequency is sensitive to the width of the measurement window. To account for the width of the measurement window a frequency (1/s) for conversion of kinetic energy (Joules) to kinetic energy flux (Watts) (commonly called power) can be found by dividing the rate of energy propagation (m/s) by the measurement window width (m). For an undisturbed wave flow field the rate of energy propagation is known to be the wave group velocity (C_g). If the 'according frequency' is taken to be the wave frequency; the resultant sum of the wave power will vary depending on the chosen width of the measurement window, which is obviously incorrect and can either exaggerate or diminish the actual result.

Table 2.1 Uncertainties for kinetic energy components

Parameter	Value	Uncertainty
dx	6.01mm	0.5 mm
dy	6.01mm	0.5 mm
Density (ρ)	999.1kg/m^3	2kg/m^3
$V_{(x,y)}$	Variable	See Table 2.2

Table 2.2 Summary of specific uncertainty for the velocity field and resultant total kinetic energy over a wave cycle (*H*=0.07m and *f*=0.44Hz)

$\frac{t}{T}$	n	$\bar{u}_{Vx}$ (m/s)	$\bar{u}_{Vy}$ (m/s)	u_{E_t} (J/m)	$\frac{u_{E_t}}{E_t} \times 100$ (%)
0.03	40.7	0.0069	0.0062	0.25	9.2
0.09	33.9	0.0071	0.0067	0.28	9.7
0.16	42.4	0.0069	0.0064	0.24	9.8
0.22	32.4	0.0072	0.0067	0.24	11.5
0.28	42.9	0.0069	0.0065	0.20	12.6
0.34	33.0	0.0074	0.0067	0.17	15.2
0.41	42.1	0.0073	0.0066	0.15	16.4
0.47	33.3	0.0072	0.0071	0.17	15.4
0.53	41.4	0.0068	0.0064	0.17	12.6
0.59	34.0	0.0069	0.0066	0.17	13.7
0.66	40.7	0.0066	0.0063	0.14	13.9
0.72	33.4	0.0068	0.0065	0.13	14.7
0.78	39.9	0.0067	0.0062	0.11	13.9
0.84	34.9	0.0069	0.0068	0.12	13.3
0.91	40.4	0.0069	0.0062	0.18	10.9
0.97	33.7	0.0072	0.0065	0.24	10.3
Average	**37.4**	**0.0070**	**0.0065**	**0.19**	**12.7**

CONCLUSION

A preliminary analysis has been conducted which provides phase-averaged (ensemble-averaged) results for a forward-facing bent-duct oscillating water column in a monochromatic wave of height 0.07m and frequency 0.44Hz. Visualization of the velocity fields reveals the bulk flow regime (including water column heave, vortices and an outflow jet) at the centerline plane of the model which will prove useful in the future design of OWC geometry. The phase-averaged velocity field data can also be used for the validation of CFD results and energy balance investigations. It is unlikely that direct calculation of dissipation from PIV velocity fields produces meaningful results due to the spatial averaging inherent in the derivation of the PIV results and the scale at which dissipation physically occurs.

REFERENCES

Cruz, J. (Ed.), 2008. Ocean Wave Energy: Current Status and Future Perspectives. Springer Verlag.

Evans, D.V., 1978. The Oscillating Water Column Wave-energy Device. IMA Journal of Applied Mathematics 22, 423 –433.

Folley, M., Whittaker, T., 2002. Identification of Non-Linear Flow Characteristics of the Limpet Shoreline OWC, in: Proceedings of the Twelfth (2002) International Offshore and Polar Engineering Conference, May 26,2002 - May 31,2002, Proceedings of the International Offshore and Polar Engineering Conference. International Society of Offshore and Polar Engineers, Kitakyushu, Japan, pp. 541–546.

Graw, K.U., Schimmels, S., Lengricht, J., 2000. Quantifying Losses Around the Lip of an OWC by Use of Particle Image Velocimetry (PIV). Presented at the Fourth European Wave Energy Conference, LACER-Leipzig Annual Civil Engineering Report, Aalborg, Denmark.

Imai, Y., Toyota, K., Nagata, S., Setoguchi, T., Oda, J., Matsunaga, N., Shimozono, T., 2008. An E p erimental Study of Negative Drift Force Acting on a Floating OWC "Backward Bent-duct Buoy", in: ASME Conference Proceedings. pp. 871–879.

ITTC, 2008a. Guide to the Expression of Uncertainty in Experimental Hydrodynamics, ITTC Guide 7.5-02-01-01, Revision 01, ITTC – Recommended Procedures and Guidelines.

ITTC, 2008b. Uncertainty Analysis: Particle Imaging Velocimetry, ITTC Procedure 7.5-01-03-03, ITTC – Recommended Procedures and Guidelines.

LaVision GmbH, 2009. Product-Manual for DaVis 7.2. LaVision GmbH, Göttingen, Germany.

Longo, J., Shao, J., Irvine, M., Stern, F., 2007. Phase-Averaged PIV for the Nominal Wake of a Surface Ship in Regular Head Waves. J. Fluids Eng. 129, 524–540.

Morrison, I.G., 1995. The Hydrodynamic Performance of an Oscillating Water Column Wave Energy Converter (PhD thesis).

Müller, G., Whittaker, T., 1995. Visualisation of Flow Conditions Inside a Shoreline Wave Power-Station. Ocean engineering 22, 629–641.

Turney, D.E., Anderer, A., Banerjee, S., 2009. A Method for Three-Dimensional Interfacial Particle Image Velocimetry (3D-IPIV) of an Air-Water Interface. Measurement Science and Technology 20.

3

PHASE-AVERAGING OF VELOCITY FIELDS IN AN OSCILLATING WATER COLUMN USING SPLINES

This chapter has been accepted for publication with 'Proceedings of the Institution of Mechanical Engineers, Part M: Journal of Engineering for the Maritime Environment', has been published online. The citation for the research article is:

Fleming, A., Penesis, I., Macfarlane, G., Bose, N., Hunter, S., 2012. Phase-averaging of Velocity Fields in an Oscillating Water Column Using Splines. *Proceedings of the Institution of Mechanical Engineers, Part M: Journal of Engineering for the Maritime Environment*

ABSTRACT

The principal objective of this paper is to present a phase-averaging method by curve-fitting using B-splines. The method was designed specifically to process phase-clumped and discontinuous periodic data. Phase-averaging by ensemble-averaging of data clumped in phase will cause phase bias error if the mean phase of the clumped data does not equal the desired phase. The curve-fitting method presented here avoids phase bias error. The performance of the curve-fitting method was compared favourably with the ensemble-averaging method when processing phase-clumped experimental data. Generally, the curve-fitting method exceeded the performance of ensemble-averaging method when the data was clumped in phase and matched the performance of ensemble-averaging method when the data was randomly distributed in phase. Experimentally obtained phase-clumped two-dimensional velocity fields at the centreline of a forward-facing bent-duct oscillating water column (OWC) were processed using the curve-fitting method. The phase-averaged velocity fields were combined for visualisation purposes in the form of animated gifs to show the velocity fields over a wave cycle. The gifs correspond to the four separate monochromatic wave frequencies tested and accompany the online version of this paper. The gifs reveal the two-dimensional phase-averaged flow characteristics at the centreline of the model with phenomena including: oscillating flow, water column heave and slosh, front wall swash and down wash, an outflow jet and vortices. It was concluded that phase-averaging using splines finds a niche for the phase-averaging of data which is dispersed (or clumped) in phase.

INTRODUCTION

The oscillating water column is a wave energy conversion device which at its simplest consists of a wall which penetrates the sea surface to form a chamber. Air enclosed by the chamber and the free surface is connected to the atmosphere via a bi-directional turbine (commonly a Wells turbine (Brooke, 2003)). The water inside the chamber oscillates due to external wave action which in-turn causes the air to flow in and out of the chamber via the turbine.

There exist two (at least) distinct methods to phase average periodic data. The first is where 'like' data is simply averaged in a discrete manner by assuming that each data point in the collection is captured at the same phase. The second method recognizes that the data is continuous (without interruption) and a curve is fitted to the data. The first method, often described as *ensemble-averaging*, is best suited to highly repeatable and predictable events, namely rotary motion where an encoder (or other suitable angular reference) can be utilised to initiate the capture of data with excellent precision. The *curve-fitting* method is employed in phase-averaged analysis of events which have some variability in time and are not completely repeatable, for example waves propagating in a wave tank. Both methods will eventually have a discrete number of phases. The number of phases for ensemble-averaging is set during experimental design and is generally fixed, whilst the curve-fitting method has no limit to the number of phases and is decided at the discretion of the researcher during data analysis.

Ensemble-averaging of particle imaging velocimetry (PIV) (Grue *et al*., 2004; Raffel *et al*., 2007) data has been applied extensively in wave tanks and circulating water channels including the study of: ship and propeller wake analysis in which the phase signal is recorded by an encoder tracking the propeller shaft angle (Felli *et al*., 2009, 2010), breaking waves (Kimmoun and Branger, 2007; Ryu et al., 2007; Huang et al., 2009), wave-structure interaction (Jung *et al*., 2005) and velocity fields in an oscillating water column (Fleming *et al*., 2011).

Longo *et al*. (2007) applied curve-fitting phase-averaging to wake analysis of a ship in regular seas fitting data points with a fifth order polynomial least squares reduction technique (following some data conditioning). Harmonic components were then extracted with Fast Fourier Transform (FFT) analysis up to the tenth harmonic.

The authors presented an ensemble phase-averaged analysis of a two-dimensional flow field at the centreline plane inside a scale model of a forward-facing bent-duct oscillating water column (Fleming *et al*., 2011). The model was exposed to monochromatic waves for the wave conditions of height 0.07m and frequency 0.44Hz based on a mosaic of seven separate fields of view which provided the entire velocity field inside the OWC at the centreline plane. Experimental data was also obtained for the additional wave frequencies corresponding to a wave height of 0.07m for 0.50Hz, 0.57Hz and 0.77Hz, but it was found that clumping of data

(clusters of data points in the phase domain) for some of the experimental positions prevented the calculation of the ensemble average for some of the position/phase combinations. A curve-fitting method using B-splines was developed specifically to handle the clumped data and is described in detail in this paper. The method was applied to two-dimensional velocity fields, but is equally applicable to three or more dimensions.

Two separate types of results are presented in this paper. First, the performance of curve-fitting phase-averaging is compared with ensemble-phase-averaging when applied to clumped data. Second, the curve-fitting phase-averaged velocity fields over a wave cycle by curve-fitting for the 0.07m 0.77Hz wave are presented. The velocity fields were incomplete when using the ensemble-averaging method and also possess the greatest differences to the velocity fields presented in (Fleming *et al*., 2011) which were for the 0.07m 0.77Hz wave. Accompanying the online version of this paper are four animated gifs which visualise the flow inside and around the OWC at its centreline for the wave conditions tested.

METHODS

EXPERIMENTAL SETUP

Experiments were conducted in the Australian Maritime College Towing Tank with a length of 100m, width of 3.55m and depth of 1.5m (http://www.amc.edu.au/maritime-engineering/towing-tank). A scale model of a generic forward-facing bent-duct oscillating water column wave energy extraction device (profile outlined in Figure 3.1) was tested in monochromatic seas for the conditions listed in Table 3.1. The model was 500mm wide and was fitted with a 58mm diameter orifice. The model was positioned in the middle of the towing tank crosswise in front of a viewing window approximately midway lengthwise between the wave maker and beach. Image pairs were obtained at seven separate positions (Figure 3.1) using standard PIV equipment at the resolution of 1376×1024 pixels to create a mosaic of the area of interest. Image acquisition was synchronised to commence at the next wave crest as monitored by a resistance wave probe mounted adjacent to the front face of the OWC model using a real-time Labview peak detection program. Image pairs were acquired at a frequency of $8f$ for the wave frequencies 0.44Hz, 0.50Hz and 0.57Hz and $6f$ for the 0.77Hz wave, where f is the wave frequency. Experiments were run for a maximum duration of 100 seconds to minimise wave reflection interference from the beach end of the towing tank. Experiments were repeated to increase the number of image pairs. Further details on experimental setup are detailed in Fleming *et al*. (2011).

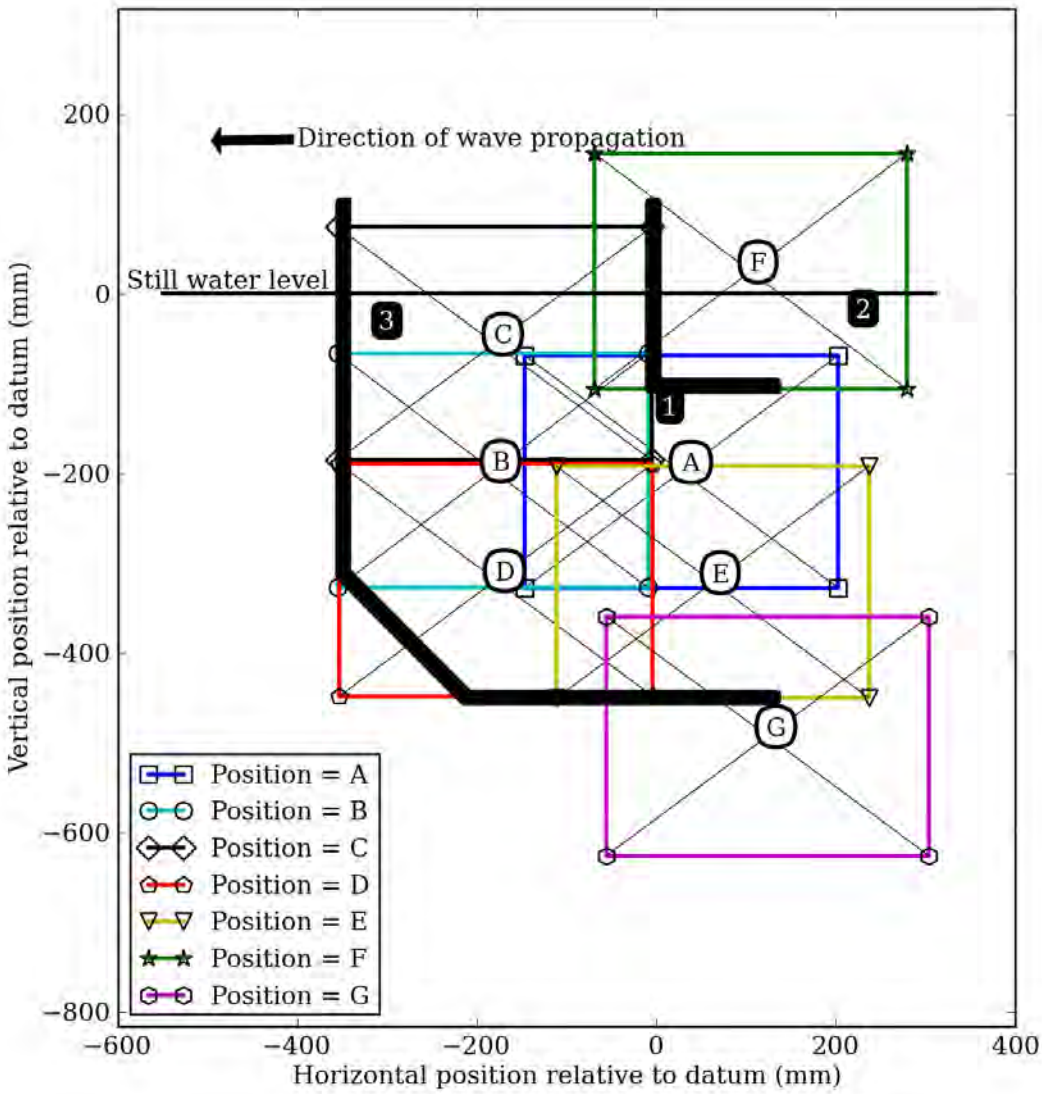

Figure 3.1 Field of view for experimental data, OWC geometry is outlined in black, sample locations are numbered (1-3)

An unfortunate (though initially intended) side effect of setting the PIV image acquisition rate equal to an integer fraction of the wave frequency meant data clumped around 6 or 8 central phases, a function of the acquisition rate, which resulted in a variable bias error in phase for ensemble-averaged data (see Figures 3.6 and 3.7) when data failed to clump equal around the central phase.

Velocity fields were calculated from the image pairs using DaVis7.2 (LaVision GmbH, 2009). The processing sequence is outlined in Table 3.2. The axis system used in the PIV data is a standard Cartesian coordinate system, with the datum being located at the intersection of the front face of the OWC and the waterline. A pixel corresponds to a position in space and is interchangeable between images and velocity fields, with a corresponding reduction in the pixel resolution of the velocity field depending on the final multi pass mode. For these velocity fields, the reduction (known as Vector Grid in DaVis7.2) is $32 - 32 \times 25\% = 24$.

Table 3.1 Test matrix

Position	Wave height (m)	Wave frequency (Hz)
A, B, C, D, E, F, G	0.07m	0.44Hz (λ=7.1m, slope =0.031) 0.50Hz (λ=5.8m, slope =0.038) 0.57Hz (λ=4.7m, slope =0.047) 0.77Hz (λ=2.6m, slope =0.084)

Table 3.2 PIV post processing sequence (using DaVis7.2)

Operation	Description
Mask from text (position C only)	Custom function (for masking above free surface)
Manual masking (position F only)	Manually masked sorted images (16 bins)
Image correction	3rd order polynomial mapping
Image pre-processing	High Pass(64) + Subtract(10)
Correlation mode	Cross Correlation
Multi pass mode	1x(64x64,50%), 2x(32x32,25%)
Vector post-processing	Median filter (5) Fill missing Smoothing

DATA REDUCTION

Velocity field data was phase-averaged in two steps: in the first step each velocity field, which corresponds to an experimentally obtained image pair, was assigned a phase, the second step was to sort the data into ascending phase (technically not essential) and to average through data for the same phase bin either by curve-fitting or ensemble-averaging.

A resistance wave probe positioned adjacent to the front face of the OWC was used as the synchronisation signal and is referred to as the 'phase wave probe'. Each velocity field was assigned a phase using the phase expression given by

$$\frac{t}{T} = modulo\left(\frac{\gamma_{FH}}{2\pi} + \frac{t_{image} - t_{zero}}{t_{zero+1} - t_{zero}}, 1\right) \tag{3.1}$$

where γ_{FH} is the phase shift of the first harmonic using Fourier series analysis of the current wave, t_{image} is the image acquisition time, t_{zero} is the time of preceding zero up crossing and t_{zero+1} is the time of the following zero crossing, $modulo$ is the remainder after division by the second argument which is unity in this case.

Equation (3.1) is the same as presented in (Fleming *et al.*, 2011) with an additional phase correction term $\left(\frac{\gamma_{FH}}{2\pi}\right)$, the phase correction term previously employed by (Longo *et al.*, 2007). The phase correction causes a left or right phase shift equal to the FFT first harmonic phase angle of the current wave profile; affecting a more even distribution of uncertainty across the wave profile. Figure 3.2 shows an example of phase sorted data without and with phase correction respectively. The standard deviation is shown as columns with the magnitude shown on the right vertical axis. The standard deviation is more constant when phase correction is used (the right side) and is also generally the case. The phase correction was found to reduce the standard deviation of ensemble-averaged phase wave probe amplitude for the current data set by an average of 7.8%, a minimum of -1.5% and a maximum of 18.1% over the periodic cycle $\left(\frac{t}{T} = 0 \ldots 1\right)$ for all the experimental data used.

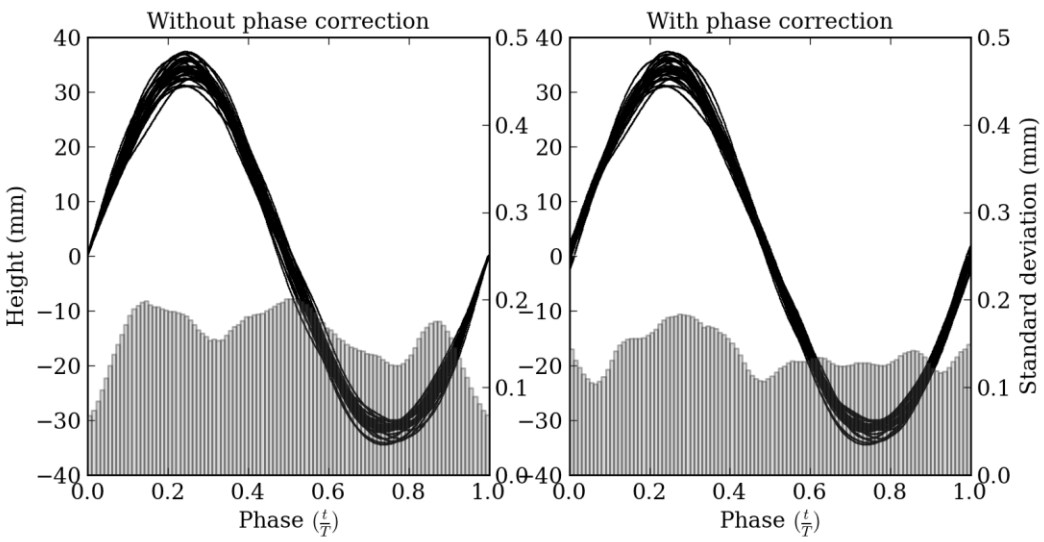

Figure 3.2 Demonstration of the effect of the phase correction term applied to phase wave probe data. The curves represent the instantaneous profile and bars represent the standard deviation (12.4% reduction in mean standard deviation of amplitude for this example)

ENSEMBLE-PHASE-AVERAGING

Ensemble-phase-averaging was performed using DaVis7.2 (LaVision GmbH, 2009) for sixteen non-overlapping windows of equal width in the phase range $0 \leq \frac{t}{T} < 1$. The central phase is taken as the centre of the window and is likewise between zero and unity (0.032, 0.094,..., 0.97). The average and RMS velocity fields are (LaVision GmbH, 2009):

$$V_{avg} = \frac{\sum_{i=1}^{n} V_i}{n} \tag{3.2}$$

$$V_{RMS} = \sqrt{1/(n-1)\sum_{i=1}^{n}\left(V_i - V_{avg}\right)^2} \tag{3.3}$$

where V_i is the velocity component and n is the number of source vectors. Two additional processing options were used: the first was to accept only those vectors in the range $-2\left(V_{avg} - V_{RMS}\right) \leq V_i \leq 2\left(V_{avg} - V_{RMS}\right)$ which required a second iteration for calculation; the second was to perform the averaging only if five or more valid vectors exist.

CURVE-FITTING PHASE-AVERAGING

N-dimensional B-splines provide the flexibility necessary to handle clumped, periodic and discontinuous data through the following features:

- Periodic and non-periodic modes - The periodic mode ensures that the curves overlap at the start and finish and is used when data is continuous. The non-periodic mode is used when the data is discontinuous and it is not possible to ensure an overlap. An example of discontinuous data is when the water level drops below the pixel position, over that duration the vectors are not defined.
- Control over smoothing - When based on the immediate standard deviation of nearby data; smoothing is necessary to isolate unwanted noise from the signal.
- N-dimensional (x, y ...) – The curve is in n-dimensional space for which the components are solved simultaneously.

Curve-fitting calculations were performed with the programming language Python 2.7 (Van Rossum and Drake, 1995) (available at www.python.org). Velocity field data was fitted using third order B-spline curves in two-dimensions. The phase-averaging process described here was performed on a pixel by pixel basis and has two distinct steps: the first step prepared mean and weighting values for processing with the spline function for which x,y components are obtained independently; the second step fitted mean and weighting values simultaneously with the spline function. If data was found to be discontinuous the spline was fitted for each valid segment of data.

The method for preparation of the mean and weighting values is now described in detail. All velocity fields from a single position with matching wave conditions (height and frequency) were sorted in ascending phase using Equation (3.1). The vectors were then duplicated at each end using Equation (3.4) extending the phase range to $-0.5 < \frac{t}{T} < 1.5$; analogous to having two identical periodic cycles starting at $\frac{t}{T} = -0.5$ with the purpose being to provide the same amount of data for polynomial fitting.

$$\begin{cases} 0.5 \geq \frac{t}{T} > 1.0, \frac{t}{T} - 1 \\ 0.0 \geq \frac{t}{T} > 1.0, \frac{t}{T} \\ 0.0 > \frac{t}{T} \geq 1.0, \frac{t}{T} + 1 \end{cases} \tag{3.4}$$

Average and weighting values were determined for 201 equal sized non-overlapping windows in the range $0 \leq \frac{t}{T} \leq 1$, with a window width of 0.005 (equivalent to 1.8 degrees) by 41 iterations at 41 equally spaced central phases (0, 0.025, …, 1; see Figure. 3.3) with four adjacent phases (two above and two below the central phase). There were four adjacent phases outside the range $0 \leq \frac{t}{T} \leq 1$ (i.e. -0.01, -0.005, 1.005, 1.01) which were calculated but discarded.

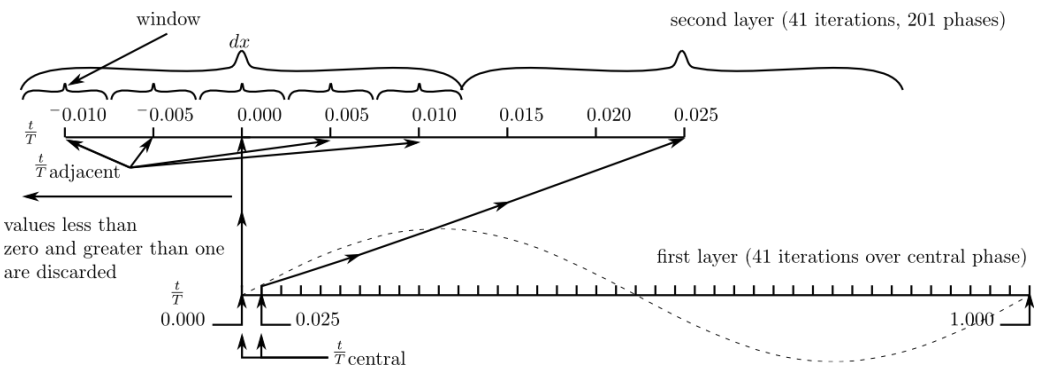

Figure 3.3 Layers of subdivision of phases

Iterating over the 41 central phases, an adaptive sliding window was used to select data points which match the following criteria:

(a) At least the nearest n data points of the total number of data points (set at a constant 8.4% for the results presented here and chosen based on the number of clumps) ;
(b) All data points were within $\pm$ half the spacing between central phases (shown as dx in Figure 3.3).
(c) For each window; only those data points within two standard deviations of the mean amplitude of the same window were used.

From the selected data the mean value for the central phase and four adjacent phases were determined. A quadratic fit was used provided at least four out of five windows were occupied with data; otherwise a linear fit was used. Figures 3.4 and 3.5 demonstrate the selection of data and polynomial fits, only data (+) with halos were used for curve-fitting. The central phase is marked with a vertical dashed line, the fit of the central phase and four adjacent phases are shown as squares, solid vertical lines separate the windows. The logic behind this is as follows: the quadratic fit was used where possible to minimise the flattening of peaks; the linear fit was used only when insufficient information was available to make conclusions on the trends of the

data other than the slope. Figure 3.4 shows a linear fit which was used to interpolate across a region of sparse data: weighting conditioners (detailed in the following paragraphs) were used to diminish the contribution of fits where data was missing. Figure 3.5 shows a fit when the conditions stated above was satisfied to use a quadratic fit.

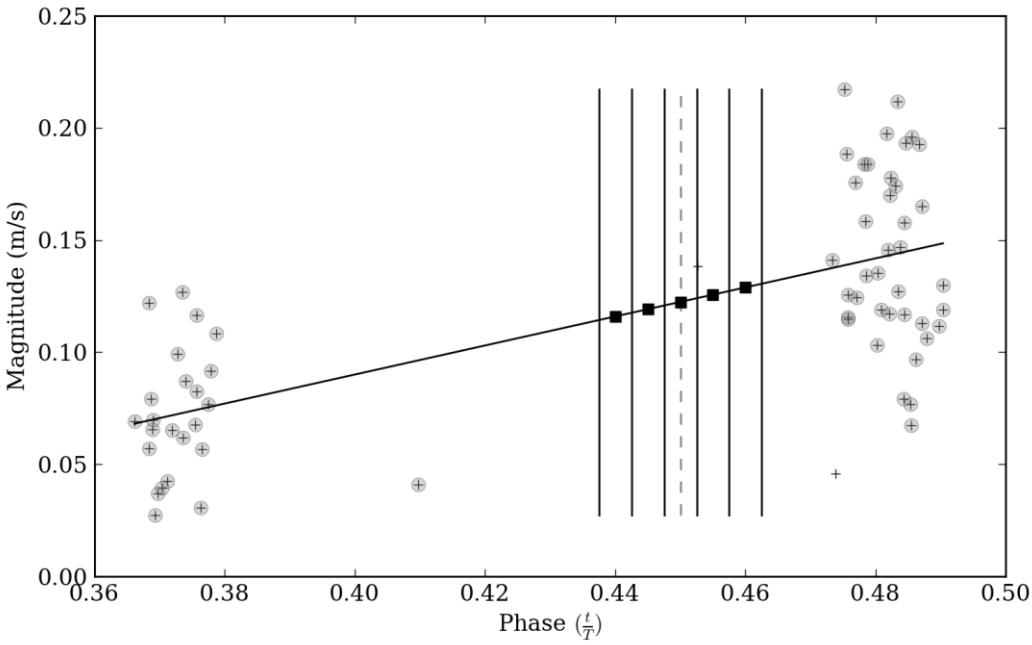

Figure 3.4 Linear fit applied to selected data (with halos)

The weighting for each phase (201 in total) was calculated by Equation (3.5)

$$w = \frac{5}{\sigma_{201}} \tag{3.5}$$

where the value for σ_{201} was the standard deviation of valid data in the window provided at least two valid data points existed. If there was less than two valid data points in the window; ¼ of standard deviation of all data points was used.

Two weighting conditioners were developed to further reduce or enhance the weightings based on distribution of the data to respond to the clumping of data in phase. The weighting conditioners were applied to the weighting using Equation (3.6) to give a conditioned weighting (w_c). Each array of conditioners had a mean of unity ($\frac{1}{201}\sum_{i=1}^{201} C_{x_i} = 1$, where C_{x_i} is the conditioner). When data is randomly distributed in phase (not clumped), each element of either conditioner approaches unity ($w_i \rightarrow 1$), nullifying the effect of the conditioner.

$$w_c = w \times C_{distribution} \times C_{balance} \tag{3.6}$$

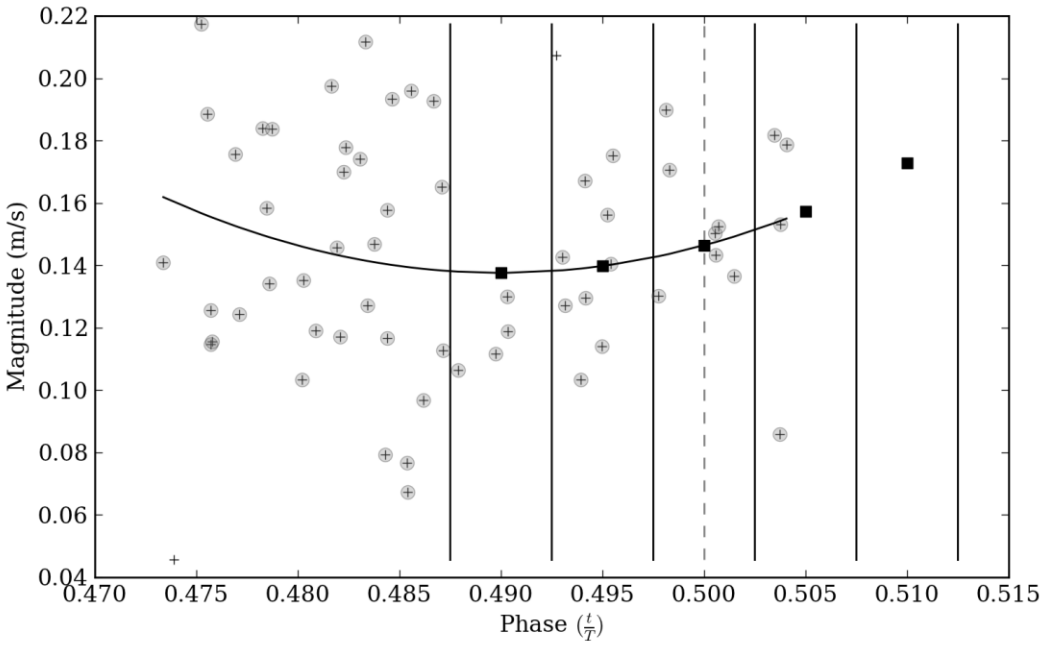

Figure 3.5 Quadratic fit applied to selected data (with halos)

The global distribution weighting conditioner ($C_{distribution}$) considered the distribution of data across the wave cycle and the calculation performed was a normalised histogram with 41 equal width, non-overlapping windows between -0.0125 and 1.0125 (bin width = dx). The result of the histogram corresponds to the 41 central phase, each value for the central phase was used for the four adjacent phases of each central phase, providing an array of 201 conditioners.

The balance weighting conditioner ($C_{balance}$) considered the offset of the data selection window about the central phase, the premise being that the closer the data, the better the estimate. A linear fit was used to evaluate the balance weighting conditioner over 41 iterations of the central phase (calculated at the same time as the means) and is given by:

$$C_{balance} = Mx + 1$$

$$\text{for } x = (-1, -0.5, 0, 0.5, 1)$$

$$M = \frac{1}{dx}\left(2\frac{t}{T_{central}} - \frac{t}{T_{lower}} - \frac{t}{T_{upper}}\right) \tag{3.7}$$

where $dx = 5 \times 0.005 = 0.025$, $\frac{t}{T_{lower}}$ is the lower extent of the data selection window and $\frac{t}{T_{upper}}$ is the upper extent of the data selection window, x maps to the current adjacent phases and central phase. The central phase maps $x = 0$ so the corresponding $C_{balance}$ will always equal unity. An equally balanced window has the same difference between the lower phase limit

and central phase as the upper phase limit and central phase, the slope (M) is zero making $C_{balance}$ equal to unity for the four adjacent phases in addition to the central phase.

The mean and weighting preparation process yields five arrays $\left(\frac{t}{T}, V_x, w_x, V_y, w_y\right)$ with 201 values each when applied to each velocity component. The second step of curve-fitting was to process the prepared data with the spline fitting function. The B-spline functions were accessed from a Python wrapped version of the FORTRAN subroutines written by Dierckx (1993) which are smoothing splines with automatic knot selection (Fortran code at http://www.netlib.org/dierckx/). The Python wrapped version was accessed using the SciPy package FITPACK (www.scipy.org). Two functions from FITPACK were used: *splprep* and *splev*. First the function *splprep* was used to calculate the knot points and coefficients (curve-fitting) for both velocity components simultaneously (more dimensions are permitted). Second the function *splev* was used to evaluate the knot points and coefficients to obtain the fitted velocity components for the specified phases.

Without smoothing, spline fitting forces a curve through each data point, the consequence being that point to point fluctuations (noise) will be exaggerated causing curve-fitting instability. The smoothing parameter, s, is used to trade-off between the closeness and smoothness of fit, the amount of smoothing is determined by satisfying the condition $\sum w(y - g(x))^2 \leq s$, where w is the weighting, y is the data points and $g(x)$ is the smoothed interpolation of (x, y) (Jones *et al.*, 2001). When weightings are based on the inverse of the standard deviation, good values of s can be found in the range $m - \sqrt{2m} < s < m + \sqrt{2m}$ (Jones *et al.*, 2001). The smoothing parameter used for curve-fitting was left as the default:

$$s = m - \sqrt{2m} = 201 - \sqrt{2 \times 201} \cong 181 \tag{3.8}$$

where m is the number of elements in the array.

Non-continuous data was identified by the following method: The phase sorted data was divided into 41 equally spaced windows between zero and unity, the data was considered non-continuous if more than half of the data in any window was invalid. Contiguous regions in non-continuous data were defined as being: regions where there were at least two adjacent regions of valid data, which ensured a minimum of ten data points, corresponding to two central phases and eight adjacent phases, for spline evaluation.

When the data was continuous the knot points and coefficients were calculated using the function *splprep* with the periodic switch enabled. Knot points and coefficients were then stored for the phase range $0 \leq \frac{t}{T} \leq 1$. When the data was non-continuous the knot points and coefficients were evaluated for each region of validity in an iterative manner using *splprep* with the periodic switch disabled and passing data corresponding to the range of validity. The region of validity, knot points and coefficients were stored. Storing the region of validity, knot points and coefficients meant that the splines could be quickly evaluated for any phase in the range of validity at a later time.

UNCERTAINTY

Uncertainty of phase-averaged (monochromatic) data exists in two dimensions; both phase and magnitude. Variance in magnitude is a function of the experimental methods including PIV uncertainty which has been characterised as approximately 1/10th of a pixel (Felli *et al.*, 2002) and experimental phenomena including, differences from wave to wave and the presence of turbulence. Variance in phase is also a function of data acquisition. Ensemble-averaging of randomly acquired data will produce variance that is a constant function of the bin width and will approach a constant standard deviation of $\frac{dx}{2c}$ where dx is the bin width, c = 2 for 95th percentile with an uncertainty $\pm 2\sigma$. Clumped data in phase may produce a standard deviation in phase either better or worse than this depending on the precision of synchronisation system and associated experimental variance. The uncertainty in phase is not a function of the number of data points and when using the spline averaging method is reduced to experimental uncertainty alone.

VELOCITY FIELD MOSAIC

Velocity fields with the same wave parameters and phase were merged to create a mosaic covering union of all positions by the following process: The result velocity field extents (Figures 3.9 and 3.10) was the smallest rectangle which encloses all positions. The vector spacing was taken as the vector spacing for the velocity field of position ‘A’ (see Figure 3.1). Each velocity field was resized using two-dimensional cubic spline interpolation to the shape and spacing of the result velocity field. The result velocity field was populated by taking the weighted average of the interpolated positions, the weighting for each position was a two-dimensional Gaussian distribution with a width of one standard deviation centred on the centre of the position of the source velocity field in both directions.

RESULTS AND DISCUSSION

CURVE-FITTING PERFORMANCE

Depending on the grid location (position in space), the instantaneous two-dimensional flow fields (V_{x_i,y_i}) displayed significant variations in both profile and distribution over a wave cycle associated with the localised phenomena including: vortices, turbulence, and water column slosh. Three separate examples are presented to demonstrate the performance differences between the ensemble-averaging and the curve-fitting methods.

Details of the samples are provided in Table 3.3, the physical locations are shown as the numbered patches on Figure 3.1. The fits for the samples are shown in Figures 3.6, 3.7 and 3.8 and explained in the following dot points:

- The point markers represent the instantaneous data;
- The grey filled curve with peaks extending from the bottom of each figure is the normalised weighting (absolute magnitude is not important here) ($w/\overline{w}$);
- The grey curve with small square markers shows the 201 means which were calculated using the polynomial fit;
- The square markers show the ensemble average fit;
- The dashed curve traces the spline average.

Table 3.3 Sample information

Sample	Patch No. (Figure 3.1)	Wave parameters height, frequency (m),(Hz)	Position (FOV)	Coordinates (x,y) (mm)	Data points	Figure
Vortex transit	1	0.07, 0.57	A	(9, -135)	230	3.6
Discontinuous	2	0.07, 0.50	F	(223, -27)	501	3.7
Sloshing	3	0.07, 0.77	C	(-307, -40)	915	3.8

The vortex transit sample (Figure 3.6) was taken from below the upper lip of the OWC (sample location 1 on Figure 3.1). The scatter in magnitude of the data points for both velocity components is greater for the phase range $0.6 < \frac{t}{T} < 0.8$ (only shown for the horizontal component) which is explained by turbulence associated with separation of flow from the sharp corner between the front wall of the chamber and upper lip. Due to the clumping of data in phase, the ensemble phase average is missing every second data point. The spline averaging curve is continuous showing that missing regions have been interpolated. The effect of the smoothing can be seen for the spline fit around $\frac{t}{T} = 0.66$ where the spline average curve maintains a good trend while the 201 means curve had a rapid change in magnitude, an artifice introduced by the algorithm. The peaks of the weightings (grey filled peaks) correspond with the presence of data and are further amplified by the distribution conditioner. The slopes of the weightings (making peaks) are caused by a combination of the standard deviations and balance weighting conditioner. Overall, both methods are in close agreement over the wave cycle. Where an ensemble average result exists (half is missing), the phase bias error is low since the average of the phase for the data averaged is close to the phase used. The periodic switch of the spline fitting function has ensured alignment at the beginning and end of the spline, and the use of weightings and smoothing provide appropriate interpolation over the wave cycle.

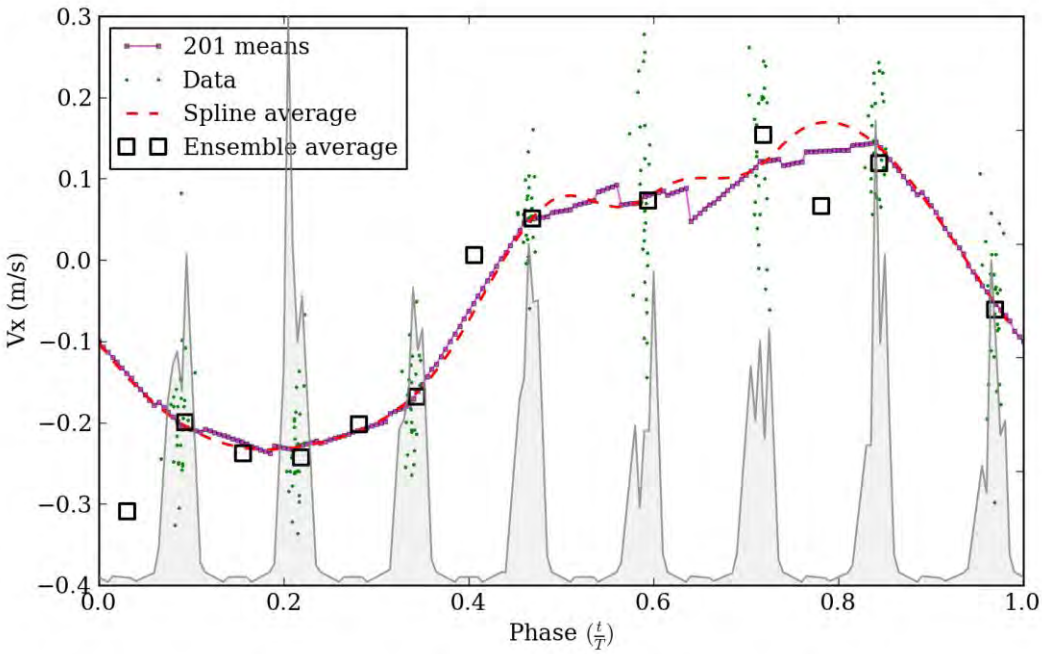

Figure 3.6 Vortex transit (sample 1) Spline average and ensemble average fit (horizontal component)

The discontinuous region sample (Figure 3.7) was taken from outside and above the upper lip of the OWC and is below the still water level (sample location 2 on Figure 3.1). The free surface drops below the pixel position for the phase range $0.45 < \frac{t}{T} < 0.98$ which is illustrated by the absence of data. Since the data is discontinuous, the spline fit was performed iteratively in non-periodic mode. The trend of the data was quite simple to follow and presented little problem to the spline, however there was some small instability but performance is still better than by ensemble-averaging. Furthermore the spline curve is only present in the regions of valid data. Clumping of the data in phase caused significant bias error of ensemble-averaged data for this particular data set; which is most obvious for the third, fifth and seventh square markers from the left. The error can be seen as the horizontal difference between the ensemble average point and the concentration of data nearby, which was used to calculate the ensemble average. The bias error was due to clumping of data at one end of the averaging window which, as previously mentioned, was a direct result of the data acquisition frequency being an integer fraction of the wave frequency.

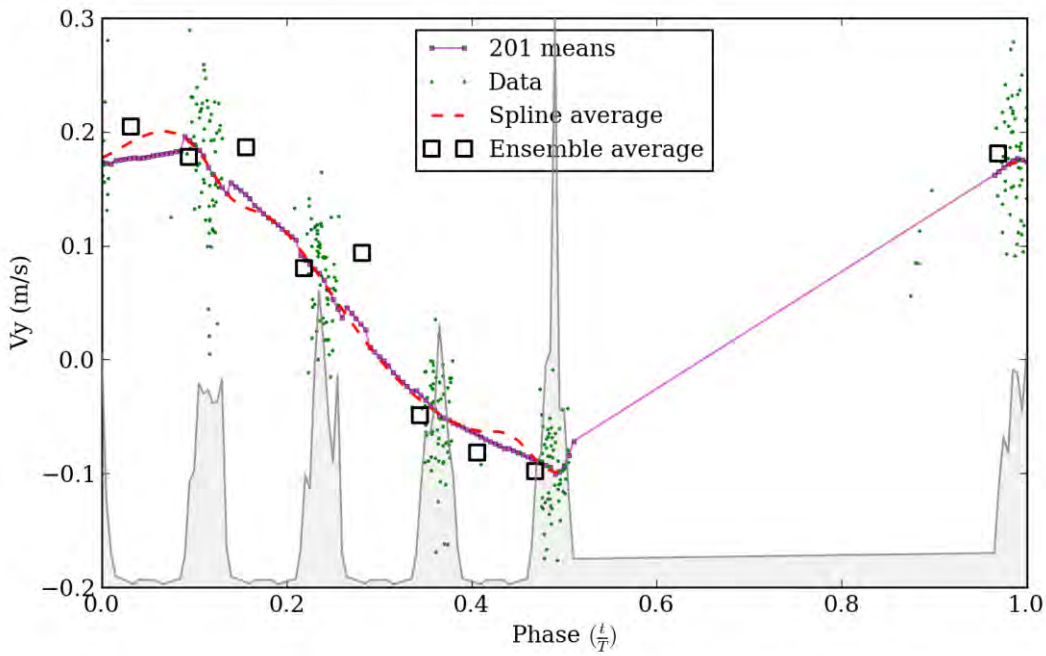

Figure 3.7 Discontinuous data (sample 2) spline average and ensemble average fit (vertical component)

The water column slosh sample (Figure 3.8) was taken from inside the OWC chamber below the still water level (sample location 3 on Figure 3.1). The effect of sloshing can be seen as multiple flow reversals in both velocity components (only horizontal component shown). The spline fit follows the data trends well, importantly the spline is able to cope with multiple reversals over a cycle (which had been problematic for higher order polynomials) and is periodic ensuring the ends meet. The ensemble average fit is reasonable (but suffers from phase bias error due to the uneven distribution of data in phase which is not as visually apparent as in Figure 3.7) and deviates from the 201 means curve, implying phase bias error.

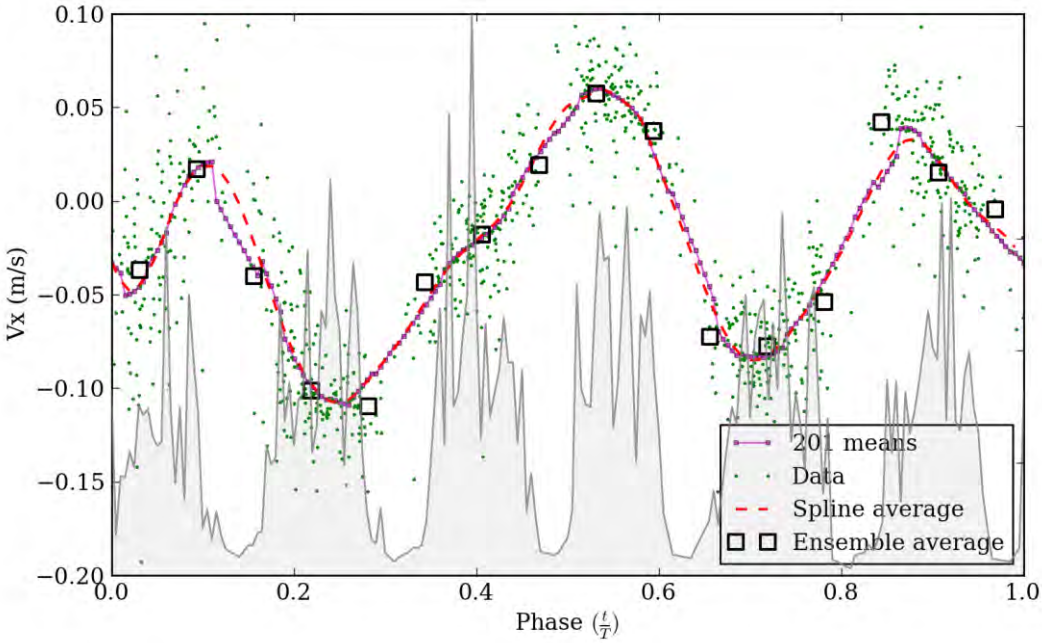

Figure 3.8 Water column slosh (sample 3) spline average and ensemble average fit (horizontal component)

VELOCITY FIELDS

As mentioned in the introduction, it was not possible to obtain reliable phase-averaged velocity fields at the higher frequency waves (0.50, 0.57, 0.77Hz) by ensemble-averaging due to clumping of data in phase. The curve-fitting method was successful at ensemble-averaging for all frequencies (with the same data). The phase-averaged velocity fields for the 0.07m 0.77Hz wave are presented in Figure 3.9 and 3.10 over one wave cycle; which had the most contrast compared to those of the 0.07m 0.44Hz wave (ensemble-averaged) that are reported in Fleming *et al*. (2011). The main differences are:

- Water column slosh is significant and obvious for the 0.07m 0.77Hz wave;
- The vortices at the lower lip are smaller and of lower intensity for the 0.07m 0.77Hz wave;
- For the 0.07m 0.77Hz wave, flow at the upper lip is more pronounced and energetic; specifically referring to flow above the upper lip: for $\frac{t}{T} = 0.03$ flow appears to be forming a plunging breaker, while at $\frac{t}{T} = 0.06$ shows the water impacting with the front face.

Absolute two-dimensional vorticity $\left(\frac{1}{2}\left(\frac{\partial v}{\partial x} - \frac{\partial u}{\partial z}\right)\right)$ (Graw *et al*., 2000) is included in the background of each velocity field to highlight the presence of vortices. For visualisation purposes the images are best viewed in sequence.

Accompanying the online version of this paper are four animated gifs corresponding to the wave conditions tested. The gifs show a looped sequence of the velocity vectors and vorticity similar to that shown in Figures 3.9 and 10 over a wave cycle. The gifs were configured to playback at real-time speeds corresponding to the wave frequency and clearly show the average two-dimensional flow-field phenomena occurring at the centreline of the OWC including: oscillating flow, water column heave and slosh, front wall swash and down wash, an outflow jet and vortices.

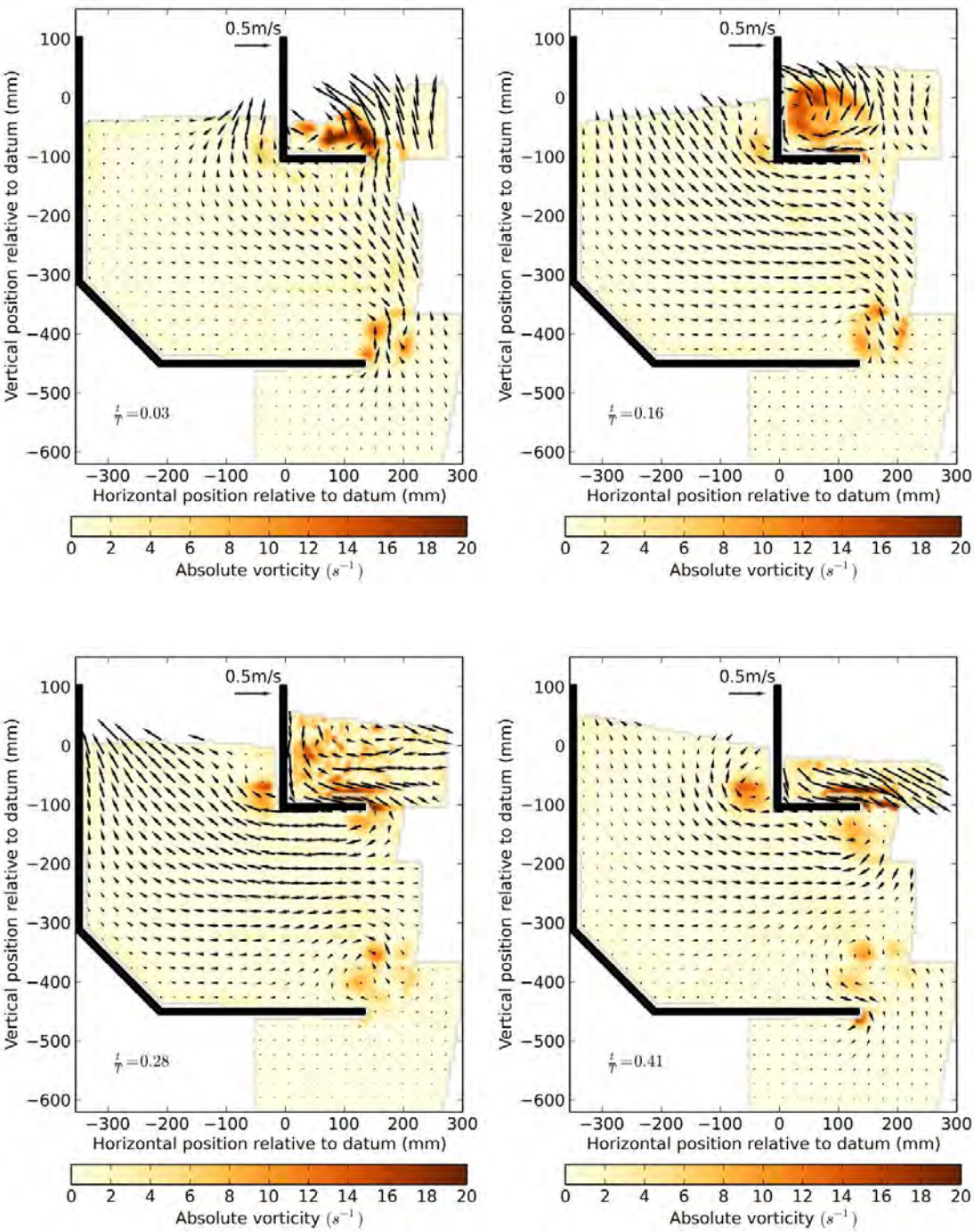

Figure 3.9 Velocity and vorticity field inside and outside the OWC device for the first half of cycle with ¾ of vectors hidden for clarity (*H*=0.07m and *f*=0.77Hz)

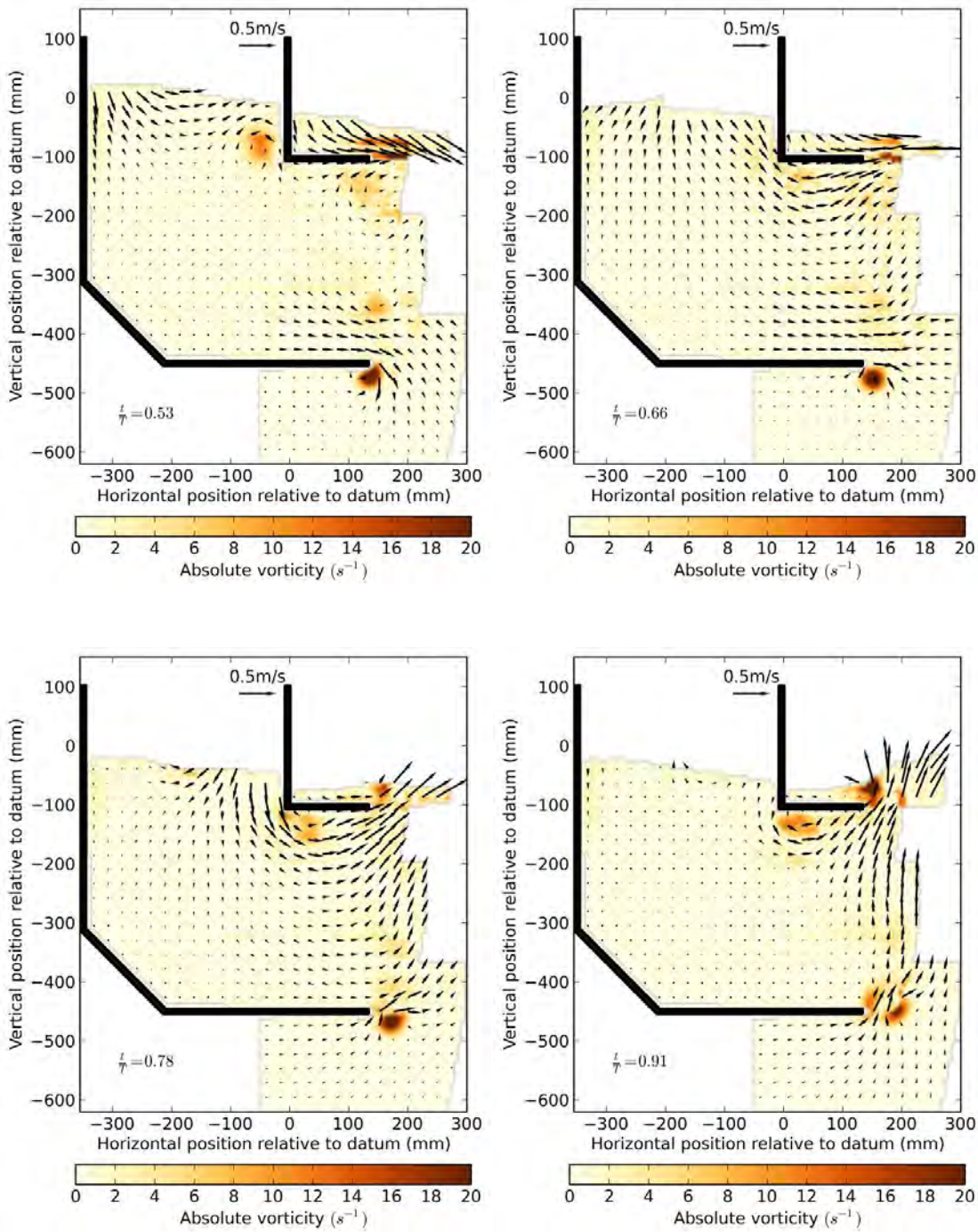

Figure 3.10 Velocity and vorticity field inside and outside the OWC device for the second half of cycle with ¾ of vectors hidden for clarity (*H*=0.07m and *f*=0.77Hz)

CONCLUSIONS

Phase-averaged analysis by curve-fitting with B-splines offer the following advantages over ensemble-averaging when processing data that is clumped in phase:

1. Reduced uncertainty in phase;
2. Removal of phase bias error;
3. Automatic interpolation/smoothing;
4. A consistent method for handling discontinuous data.

Generally, the curve-fitting method is more suitable than the ensemble-averaging method for phase-averaging of randomly acquired data whose acquisition cannot be easily synchronised with the phasing signal (not encoded), where the data acquisition rate is relatively slow or the data storage requirements are high such that increasing the number of phase bins becomes inhibitive, namely PIV velocity fields. The curve-fitting method does this by using trends in the data (the slope of the curves) to eliminate phase bias error. The expense is longer processing time and an algorithm that may require some fine tuning. A key point to highlight is that the curve-fitting method presented here has permitted the use of data which otherwise would have been unusable, or at the very least of a lower quality via ensemble-averaging.

The curve-fitting method presented has been used to obtain two-dimensional phase-averaged velocity fields at the centreline plane of the OWC for different incident wave frequencies over a monochromatic wave cycle. The velocity fields were used for qualitative (visualisation) purposes but can also be used for quantitative purposes; of particular interest is the total kinetic energy calculated from the velocity fields which can be used in an energy analysis.

Phase-averaged analysis of OWCs and wave energy converters promises to be of immediate use in terms of geometry design and optimisation but is limited to monochromatic waves. The phase-averaging method may be extended to the analysis of periodic pseudo-irregular seas but is reliant on the repeatability of experimental conditions and the determination of the phase signal.

REFERENCES

Brooke, J. (Ed.), 2003. Wave Energy Conversion, 1st ed, Elsevier Ocean Engineering Book Series. Elsevier, Boston, MA, United states.

Dierckx, P., 1993. Curve and surface fitting with splines. Oxford University Press, USA.

Felli, M., Falchi, M., Pereira, F., 2010. Distance effect on the behavior of an impinging swirling jet by PIV and flow visualizations. Experiments in Fluids 48, 197–209.

Felli, M., Pereira, F., Calcagno, G., Di Felice, F., 2002. Application of Stereo-PIV: Propeller Wake Analysis in a Large Circulating Water Channel, in: 11th International Symposium on Applications of Laser Techniques to Fluid Mechanics. Lisbon, Portugal.

Felli, M., Roberto, C., Guj, G., 2009. Experimental analysis of the flow field around a propeller–rudder configuration. Experiments in Fluids 46, 147–164.

Fleming, A., Penesis, I., Goldsworthy, L., Macfarlane, G., Bose, N., Denniss, T., 2011. Phase Averaged Flow Analysis in an Oscillating Water Column Wave Energy Converter, in: Proceedings of the ASME 2011 30th International Conference on Ocean, Offshore and Arctic Engineering. Rotterdam, The Netherlands.

Graw, K.U., Schimmels, S., Lengricht, J., 2000. Quantifying Losses Around the Lip of an OWC by Use of Particle Image Velocimetry (PIV). Presented at the Fourth European Wave Energy Conference, LACER-Leipzig Annual Civil Engineering Report, Aalborg, Denmark.

Grue, J., Liu, P.L.F., Pedersen, G.K. (Eds.), 2004. PIV and water waves, Advances in coastal and ocean engineering. World Scientific, New Jersey, London.

Huang, Z.-C., Hsiao, S.-C., Hwung, H.-H., Chang, K.-A., 2009. Turbulence and energy dissipations of surf-zone spilling breakers. Coastal Engineering 56, 733–746.

Jones, E., Oliphant, T., Peterson, P., others, 2001. SciPy: Open source scientific tools for Python.

Jung, K., Chang, K., Huang, E., 2005. Two-dimensional flow characteristics of wave interactions with a free-rolling rectangular structure. Ocean Engineering 32, 1–20.

Kimmoun, O., Branger, H., 2007. A particle image velocimetry investigation on laboratory surf-zone breaking waves over a sloping beach. J. Fluid Mech. 588.

LaVision GmbH, 2009. Product-Manual for DaVis 7.2. LaVision GmbH, Göttingen, Germany.

Longo, J., Shao, J., Irvine, M., Stern, F., 2007. Phase-Averaged PIV for the Nominal Wake of a Surface Ship in Regular Head Waves. J. Fluids Eng. 129, 524–540.

Raffel, M., Wereley, S., Willert, C., Kompenhans, J., 2007. Particle image velocimetry : a practical guide, 2nd ed. Springer, Heidelberg, New York.

Van Rossum, G., Drake, F.L. (Eds.), 1995. Python reference manual. PythonLabs, Virginia, USA.

Ryu, Y., Chang, K.-A., Mercier, R., 2007. Runup and green water velocities due to breaking wave impinging and overtopping. Experiments in Fluids 43, 555–567.

4

ENERGY BALANCE ANALYSIS FOR AN OSCILLATING WATER COLUMN

This chapter has been published with 'Ocean Engineering'; the version presented here is a modified version incorporating reviewer comments, which was submitted for publication. The citation for the research article is:

Fleming, A., Penesis, I., Macfarlane, G., Bose, N., Denniss, T., 2012. Energy balance analysis for an oscillating water column wave energy converter. Ocean Engineering 54, 33.

ABSTRACT

The principle objective of this paper is to outline the energy transfer processes occurring in a forward-facing bent-duct oscillating water column (OWC). Phase-averaged data obtained from model scale experiments conducted in monochromatic waves was used in conjunction with linear wave theory to investigate the various energy sources, stores and sinks associated with the three-dimensional OWC geometry. The analysis was restricted to energy transfer from the incoming wave and through the device, the intermediate storage mechanisms and losses, and hydraulic work performed on the power-take-off (which was simulated by an orifice plate). Results based on phase-averaged data presented include kinetic and potential energy for both an undisturbed wave and a wave interacting with the OWC geometry and power dissipated by the orifice. Two-dimensional velocity fields experimentally obtained via particle imaging velocimetry (PIV) were used to examine the kinetic energy and vorticity inside and around the device at its centreline. The main conclusion was that damping caused by the orifice (simulated power-take-off) diverts a proportion of the incoming energy around the device during the water inflow part of the cycle.

INTRODUCTION

Model test experiments provide the opportunity to examine the non-linear effects on performance of wave energy converters. An energy model is a useful tool that can be easily applied in the analysis of experimental results that is used to trace the flow of energy from sources into stores, and then into sinks. Folley and Whittaker (2002) highlighted the benefits of using a conservation of energy approach for the study of experimental data on an OWC, the most important benefit being the opportunity to include all non-linear phenomena. The work they presented included two energy models, the first energy model was for a 2D heaving terminator, the second energy model was for the LIMPET onshore oscillating water column. Video footage of a two-dimensional scale model experiment of the LIMPET device permitted the identification of three energy stores: water column heave, water column slosh, and front wall swash and down wash. Water column slosh was found to oppose the flow of energy to the power-take-off (PTO). They conclude that in shallow water it was more difficult to capture wave energy due to the non-linearity of the wave (based on Ursell number [$Ur = h.\lambda^2/d^3$ where h is wave height, λ is wave length and d is water depth]), with an exaggerated uneven delivery of energy over the wave cycle. They also conclude that "an effective design of an OWC requires that this kinetic energy be converted into a change in the water column heave with a minimum amount of energy being diverted into other motions." Furthermore; a conservation of energy principle could form the basis of an additional tool in the analysis of the performance of wave energy converters.

This paper utilises a combination of phase-averaged experimental data and linear wave theory to conduct a similar energy balance investigation on a forward-facing bent-duct oscillating water column intended for near-shore operation. Two-dimensional particle imaging velocimetry, an established visual technique for obtaining two-dimensional velocity fields, forms part of the information utilised in the analysis.

METHODS

The experimental setup was described in detail in Fleming *et al*. (2011) (see: Chapter 2) while the type of data used, the method of phase-averaging, and usage of the data are detailed in Table 4.1. The experimental layout is shown in Figure 4.1 and was conducted for the regular wave conditions of 0.07m and 0.44, 0.50, 0.57 and 0.77Hz. The power take-off (PTO) was simulated by a 58mm diameter orifice. The model was positioned at the centreline of the towing tank adjacent to a viewing window approximately midway between the wave maker and wave damping beach. A typical phase-averaged velocity field (two-dimensional) which is later used for calculation of vorticity and total kinetic energy is shown in Figure 4.2.

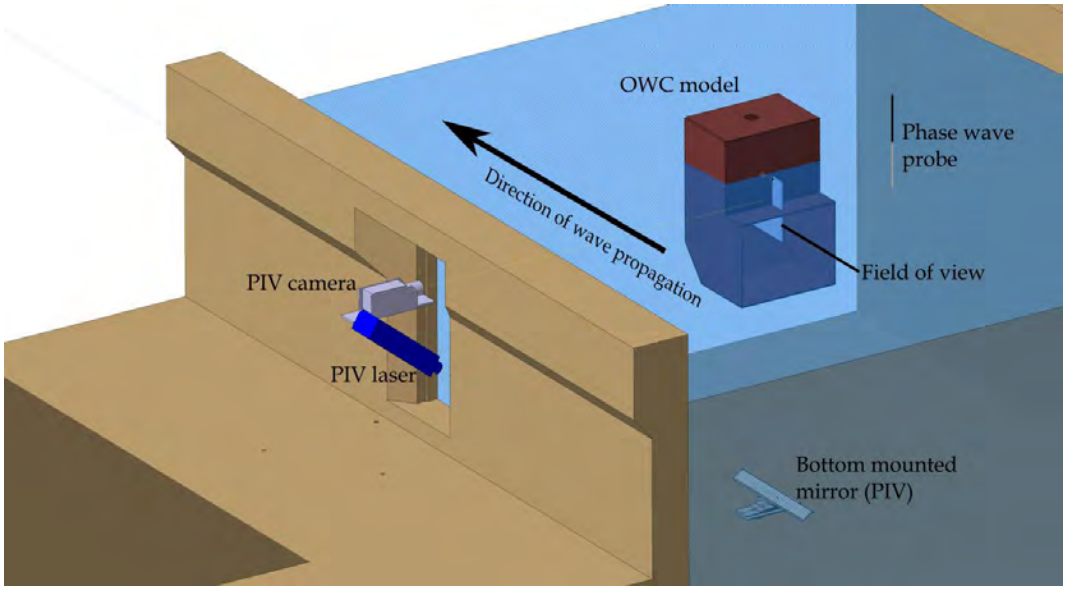

Figure 4.1 Experimental layout

Table 4.1 Experimental data and usage

Data source	Usage	Method of phase-averaging	Reference/Details
OWC chamber wave probes [Array of 7 probes]	2D water profile inside column - 1. power at power-take-off 2. Chamber potential energy	Ensemble average (100 bins , 5 random experimental sets)	(Fleming *et al.*, 2011)
Phase wave probe	Phase-averaging signal	Source of phase-averaging signal	See Figure 4.1
2 x chamber pressure transducers	Power at power-take-off	Ensemble average (100 bins , 5 random experimental sets)	2 x Omega pressure transducers PX277-05D5V
2D PIV velocity fields at the centreline plane	Experimental total kinetic energy	Spline fitting: n_min = 0.084 (has relevance to the reference only)	(Fleming *et al.*, 2012)
Undisturbed wave velocity field (linear theory)	Undisturbed wave kinetic energy	N/A	Section: Methods →Undisturbed wave

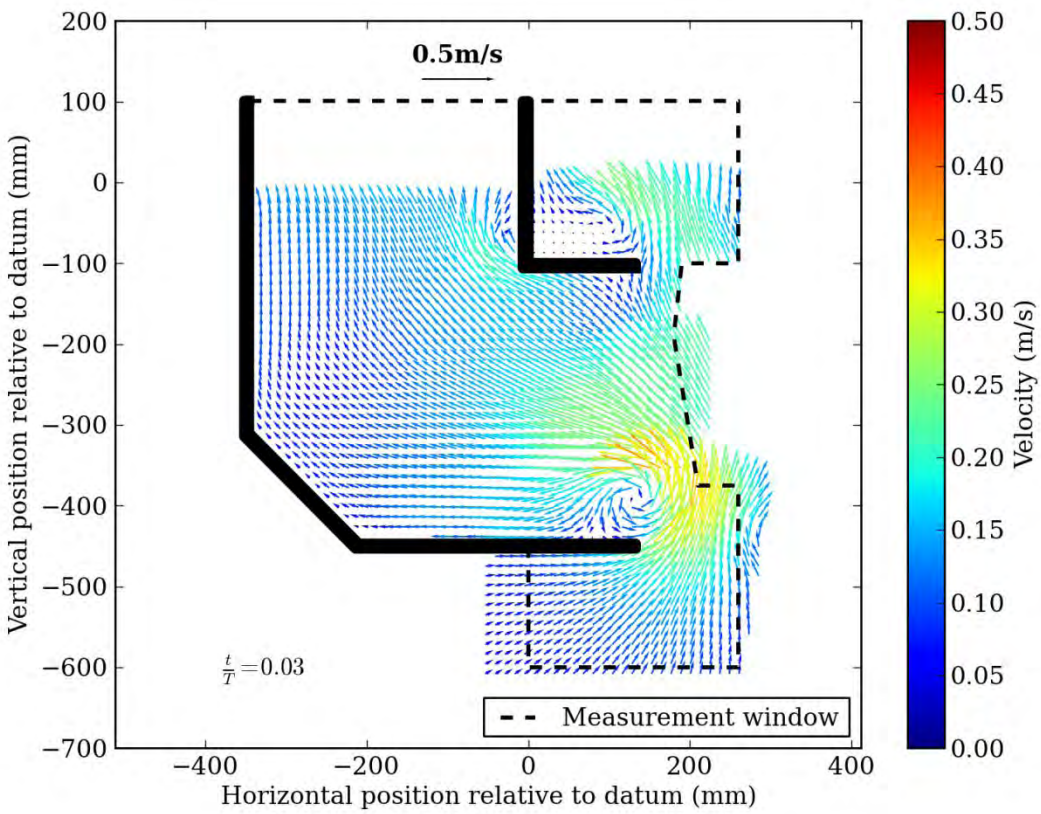

Figure 4.2 Example of a phase-averaged velocity field made from a mosaic of seven separate fields of view (3/4 of vectors hidden for clarity)

ENERGY BALANCE

The primary purpose of this paper was to investigate the energy transfer process in and around the OWC geometry over a monochromatic wave cycle by analysing experimental and numerical data. The energy model observes the premise that energy can be neither created nor destroyed and traces the flow of energy through the system in the form of a block diagram; from sources to stores and finally into sinks. Figure 4.3 shows the energy model being considered for the fixed near-shore oscillating water column used in this paper. This approach follows the method of Folley and Whittaker (2002) with the following modifications:

- "Pressure difference" has been inserted between water column heave and the power take-off (PTO) to show that energy transferred to the PTO is in the form of a pressure difference between the inside of the chamber and the atmosphere. This is facilitated by the change in volume inside the chamber due to the rise and fall of the free surface caused by wave action. The addition permits the connection of water column slosh directly to the pressure difference which is argued to be a separate phenomenon to water column heave;
- Vortices have been added as a storage mechanism to allow the possibility of wave energy being converted into vortices and then transported away with the vortex or dissipated locally as turbulence or viscous losses;
- Dashed lines have been introduced to indicate connections of a lower anticipated energy content.

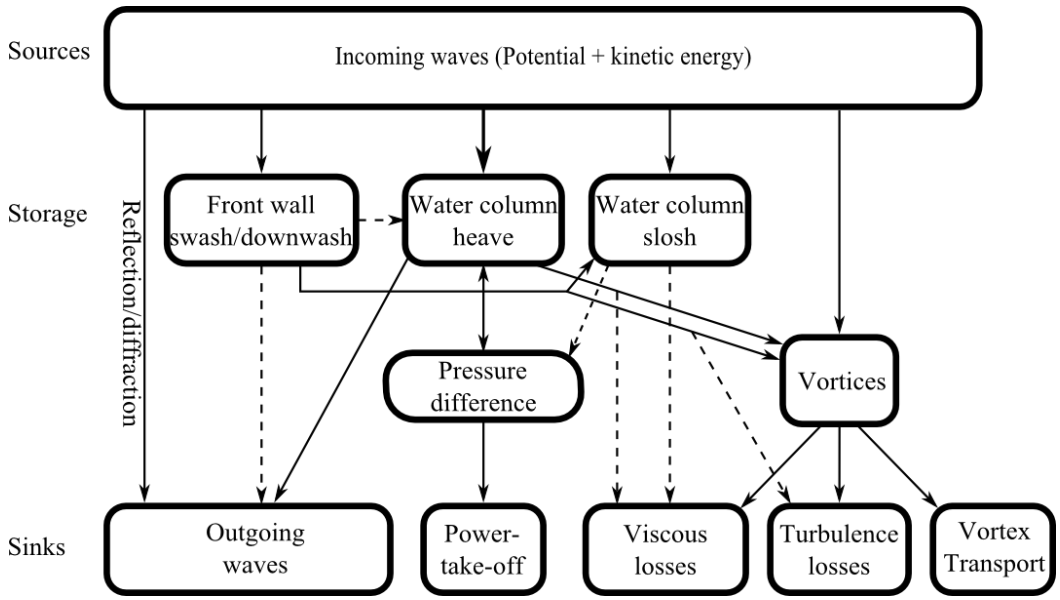

Figure 4.3 Energy model for fixed oscillating water column

The main mechanism for the transfer of energy from the incoming wave to the PTO was through the pressure differential associated with water column heave. There were two other minor connections via front wall swash/downwash and water column slosh which were considered to have lower energy content. Vortices have no outgoing connection to either water column heave or pressure differential so any energy passing into vortices cannot pass to the PTO.

UNDISTURBED WAVE

Undisturbed monochromatic waves were modelled using modified linear wave theory to match height and frequency of the waves used in experimentation. The horizontal and vertical velocity components were calculated with the same vector grid and measurement window as the 2D PIV experimental velocity fields. With the purpose to examine the effect the geometry has on the velocity fields at the centreline of the model.

Stokes' linear wave theory (Demirbilek and Vincent, 2002) was modified with the inclusion of two constants which enabled phase synchronisation of the calculated velocity field with experimental velocity field. The first constant changed the direction of propagation $\left(\mathrm{A} = \begin{cases} -1, \text{propagation to left} \\ 1, \text{propagation to right} \end{cases}\right)$, the second constant $\left(B = \frac{-\pi}{2}\right)$ was a phase shift term to make the wave zero-up-crossing with reference to time at the front face of the OWC:

$$\eta = \frac{H}{2}\cos(\theta)$$

$$\theta = kx - A\omega t + B$$

$$k = \frac{2\pi}{\lambda}, \qquad \omega = \frac{2\pi}{T} \tag{4.1}$$

$$(\omega^2 = gk\tanh(kd))$$

$$\lambda = \frac{gT^2}{2\pi}\tanh(kd)$$

where η is the wave profile, H is wave height, T is wave period, θ is the phase angle, k is wave number, ω is wave frequency, λ is wave length and is solved iteratively, d is water depth and x is the horizontal position relative to the datum.

The horizontal and vertical velocity components are given by

$$u = \frac{\pi H}{T}\frac{\cosh[k(z+d)]}{\sinh(kd)}\cos\theta$$
$$w = \frac{\pi H}{T}\frac{\sinh[k(z+d)]}{\sinh(kd)}\sin\theta \tag{4.2}$$

where z is the vertical water particle position relative to the datum.

Wave group velocity is given by

$$C_g = \frac{C}{2}\left(1 + \frac{2kd}{\sinh 2kd}\right) \tag{4.3}$$

where $C = \frac{\lambda}{T}$ is wave celerity.

2D VELOCITY FIELD CALCULATIONS

Velocity field equations provided here were used to calculate the energy for both experiment derived and undisturbed wave velocity fields. Two-dimensional total kinetic energy of the velocity field per unit width for a measurement window is given by (Graw *et al.*, 2000)

$$E_{k_{mw}} = \frac{1}{2}\rho_w \,\mathrm{dx}\,\mathrm{dz}\sum_{x,z} V_{(x,z)}^2 \tag{4.4}$$

where ρ_w is the water density, dx is pixel width, dz is pixel height and $V_{(x,z)}$ is the velocity vector component and assumes the third velocity component is zero.

Using the same assumption, two-dimensional vorticity is given by (Graw *et al.*, 2000)

$$vor = \frac{1}{2}\left(\frac{\partial v}{\partial x} - \frac{\partial u}{\partial z}\right) \tag{4.5}$$

where the strains $\frac{\partial v}{\partial x}$ and $\frac{\partial u}{\partial z}$ were calculated separately by a two-dimensional gradient function with central difference in the interior and first differences at the boundary (Oliphant and Ascher, 2001).

It was also desirable to report energy in terms of the rate of propagation of energy (energy flux). In linear wave theory it is well know that energy propagates at the rate of wave group velocity. Wave energy flux per unit width (also known as wave power) is given by (Dean and Dalrymple, 1991)

$$EF = C_g\left(\overline{E_k} + \overline{E_p}\right) \tag{4.6}$$

where $\overline{E_k} = \rho g H^2/16$ is kinetic energy per unit surface area and $\overline{E_p} = \rho g H^2/16$ is potential energy per unit surface area.

The energy flux of a measurement window per unit width was approximated by

$$EF_{mw} = C_g\left(\frac{E_{k_{mw}}}{w_{mw}} + \overline{E_p}\right) \tag{4.7}$$

where w_{mw} is the measurement window width. This method is only strictly true for a rectangular measurement window and for velocity fields where the rate of energy propagation is known i.e. a velocity field populated with an undisturbed wave. The equation is a discrete version of Equation (4.6) and will converge on the same result as Equation (4.6) (within discretisation error) when the measurement window extends from the wave crest to the full water depth when either averaged over a wave cycle for any window width or when the measurement window is an integer multiple of the wavelength. In this way it is an approximation for the instantaneous kinetic energy flux bound by the measurement window.

POTENTIAL ENERGY – WATER COLUMN HEAVE

Potential energy in the water column heave utilises the equivalent lumped mass model applied to the standard potential energy equation

$$E_p = mgh \tag{4.8}$$

where m is mass of the lump, g is gravitational acceleration, and h is the height above a reference (still water level in this case). The mass refers to the volume of water above the still water level or absent below the still water level. Assuming the chamber water level profile is constant perpendicular to the direction of wave propagation; the energy in water column heave per unit width is given by

$$E_h = \rho g A_{CS} z' \tag{4.9}$$

where A_{CS} is the cross-sectional area formed between the still water level and the free surface profile at the centreline of the model and z' is the vertical distance between the centroid of the

cross-section and the still water level. When the water level in the chamber is below the still water level both the cross-sectional area (A_{CS}) and the vertical distance (z') will be negative, so their product will be positive meaning that potential energy of water column heave is always positive.

POWER TAKE-OFF

At model scale it is convenient to ignore air compressibility (Forestier *et al.*, 2007) subsequently the power absorbed by the orifice is given by (Evans, 1982)

$$P_{PTO} = \Delta p \nabla$$
$$\Delta \mathrm{p} = p_{chamber} - p_{atm} \tag{4.10}$$

where $p_{chamber}$ is chamber pressure, p_{atm} is atmospheric pressure and ∇ is volumetric flow rate of air through the orifice.

By assuming a two-dimensional free-surface profile in cross-section, the power extracted by the PTO per unit wave crest width is

$$P_{PTO} = \Delta p \frac{dA_{cs}}{dT} \tag{4.11}$$

where $\frac{dA_{cs}}{dT}$ is volumetric flow rate per unit width (outflow being positive).

WATER COLUMN CROSS-SECTIONAL AREA

An array of wave probes were positioned inside the OWC chamber as described in (Fleming *et al.*, 2011). The cross-sectional area was calculated from the wave probe data by the following method:

Wave probe data was phase ensemble-averaged in 100 bins over a wave cycle. Calculations were performed for each phase to get cross-sectional area and all derivative calculations. The wave probe data was interpolated in three dimensions using a natural neighbour method based on Delauney triangulation (Hunter, 2007) to forty equally spaced data points along the centreline between the extents of the chamber. The interpolated data points were then fitted with a sixth order polynomial. The definite integral of the polynomial between the chamber extents gives the approximate cross-sectional area between the free surface and the datum. When the mean chamber water level was negative, the cross-sectional area was also negative which was interpreted as the absence of water.

Volumetric flow rate per unit width $\left(\frac{dA_{cs}}{dT}\right)$ as used in Equation (4.11) was calculated from the product of the gradient of the cross-sectional area with the model width divided by the phase interval $(\frac{dp}{f})$, where $dp = \left(\frac{t}{T}\right)_{n+1} - \left(\frac{t}{T}\right)_{n}$ is the phase width and f is wave frequency.

RESULTS AND DISCUSSION

Kinetic energy and potential energy per wave crest length are presented over a wave cycle for the various energy sources, stores and sinks in the follow section. The relationships between them are explained followed by a discussion on the conclusions that may be drawn from the observations.

UNDISTURBED WAVE ENERGY

The undisturbed wave was used to simulate a wave velocity field without the model in place. Figure 4.4 shows the total kinetic energy per surface area of the velocity fields in the measurement window calculated using Equation (4.7) (up to the instantaneous water level) divided by the measurement window width. All curves in the figure have a peak in the first half of the periodic cycle, while in the second half of the cycle there is a transition between the curves of a second peak for the lower frequencies to a single trough at the highest frequency. The flattening of the curve coincidentally occurs around the known resonant frequency of the OWC at 0.57Hz. Changing the lower extent of the measurement window changes the frequency at which the transition occurs and may have design implications in terms of setting the depth of the lower lip since the least fluctuation in energy flux occurs when at the transition zone. Examination of Figure 4.4 also shows that the kinetic energy flux in the measurement window is greater for higher frequency waves of the same height at any point in the wave cycle.

Since the measurement window vertically spans both crest and trough, all of the potential energy was considered to pass through the measurement window. Table 4.2 shows a summary of the energy in and propagating through the measurement window (c.f. Figure 4.2). This approach was useful for considering efficiency of the bent-duct oscillating water column because the physical arrangement of the lower lip essentially ‘cuts-off’ the energy near to the depth of the lower lip. Using this approach the proportion of energy exposure of the device correspondingly increases with wave frequency such that the device was exposed to proportionally less energy from the lower frequency waves as compared to the higher frequency waves.

Table 4.2 Energy content for waves of differing frequency using a measurement window approach averaged over n discrete phases in a wave cycle for 0.07m high monochromatic wave

Wave frequency (Hz)	Average kinetic energy per surface area integrated over depth (J/ m²)	Average kinetic energy in measurement window per surface area (J/ m²)	Ratio of kinetic energy exposure	Ratio of total energy exposure	Average energy flux exposure (W/m)
f	$\overline{E_k}$	$\overline{E_{k_{mw}}} = \frac{\sum_0^n E_{k_{mw}}}{nw_{mw}}$	$\frac{\overline{E_{k_{mw}}}}{\overline{E_k}}$	$\frac{\overline{E_{k_{mw}}} + \overline{E_p}}{\overline{E_k} + \overline{E_p}}$	$C_g\left(\overline{E_{k_{mw}}} + \overline{E_p}\right)$
0.44	3.00	1.52	0.51	0.75	9.63
0.50	3.00	1.70	0.57	0.78	8.50
0.57	3.00	1.90	0.63	0.82	7.40
0.77	3.00	2.35	0.78	0.89	5.48

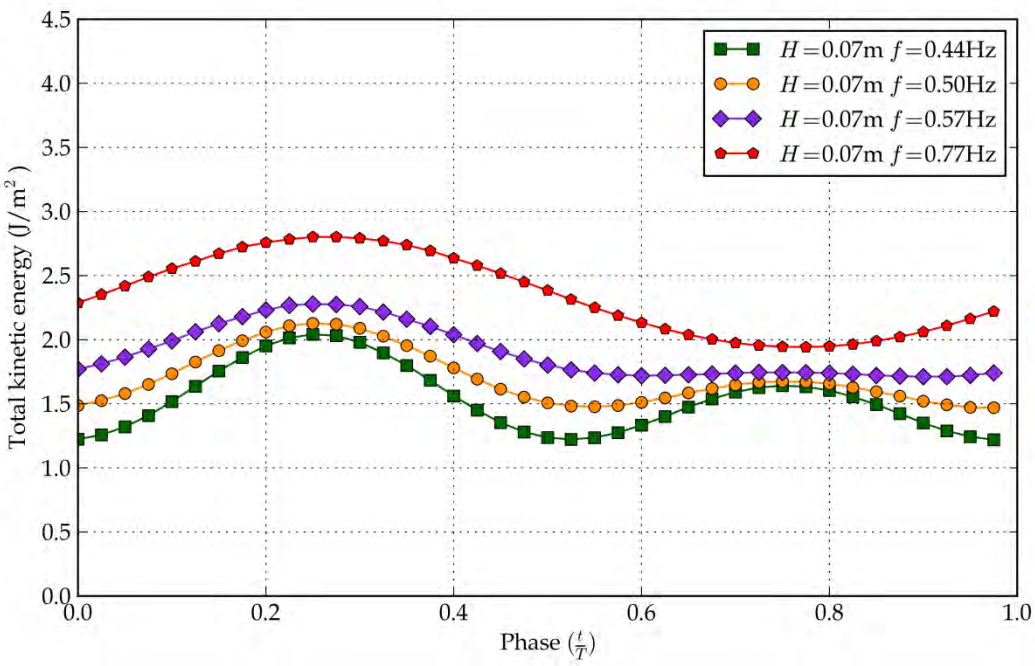

Figure 4.4 Total kinetic energy per surface area of undisturbed wave velocity fields in the measurement window over a wave cycle

EXPERIMENTAL ENERGY

Results presented in this section utilise phase-averaged velocity fields obtained experimentally as described in (Fleming *et al.*, 2011). The method of phase-averaging (curve fitting using B-splines) is detailed in (Fleming *et al.*, 2012). Figure 4.5 shows the total kinetic energy of the velocity fields for the measurement window (Figure 4.2) calculated by Equation (4.9) for all wave conditions tested.

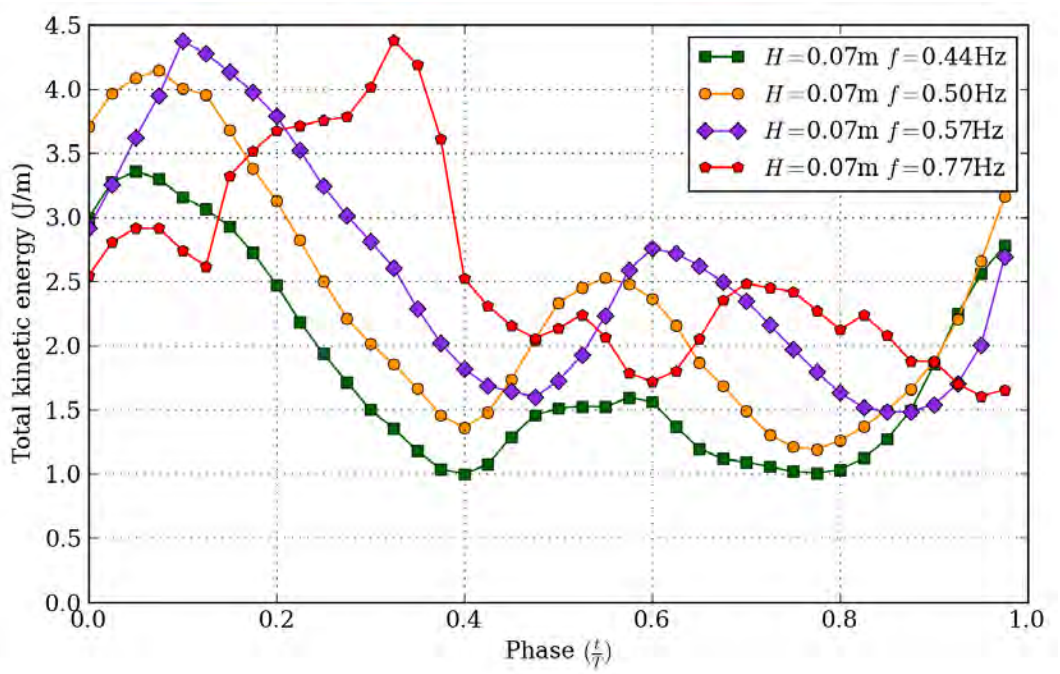

Figure 4.5 Total kinetic energy of phase-averaged PIV velocity fields in the measurement window

Several processes occur simultaneously inside the measurement window including: bulk flow, vortices, water column slosh, and water column swash and down wash. Consequently the energy of all processes was included in the curves of Figure 4.5. Generally the form of the curves was two peaks and two troughs, similar to that of the lower frequency undisturbed waves (Figure 4.4). The curve for the highest frequency wave was erratic due to the presence of significant amounts of both water column slosh, front wall swash and downwash which was reported in (Fleming *et al.*, 2012). The average magnitude of the experimental kinetic energy was at least double the average magnitude of the undisturbed wave kinetic energy (Figure 4.4). This was due to the overlap of multiple processes occurring simultaneously and demonstrates that energy is being stored. The lower second peak was primarily due to there being less water particles inside the OWC corresponding to outflow, which was the same reason for the different curve shapes in the second half of the wave cycle in the total kinetic energy plots for the undisturbed wave (Figure 4.4).

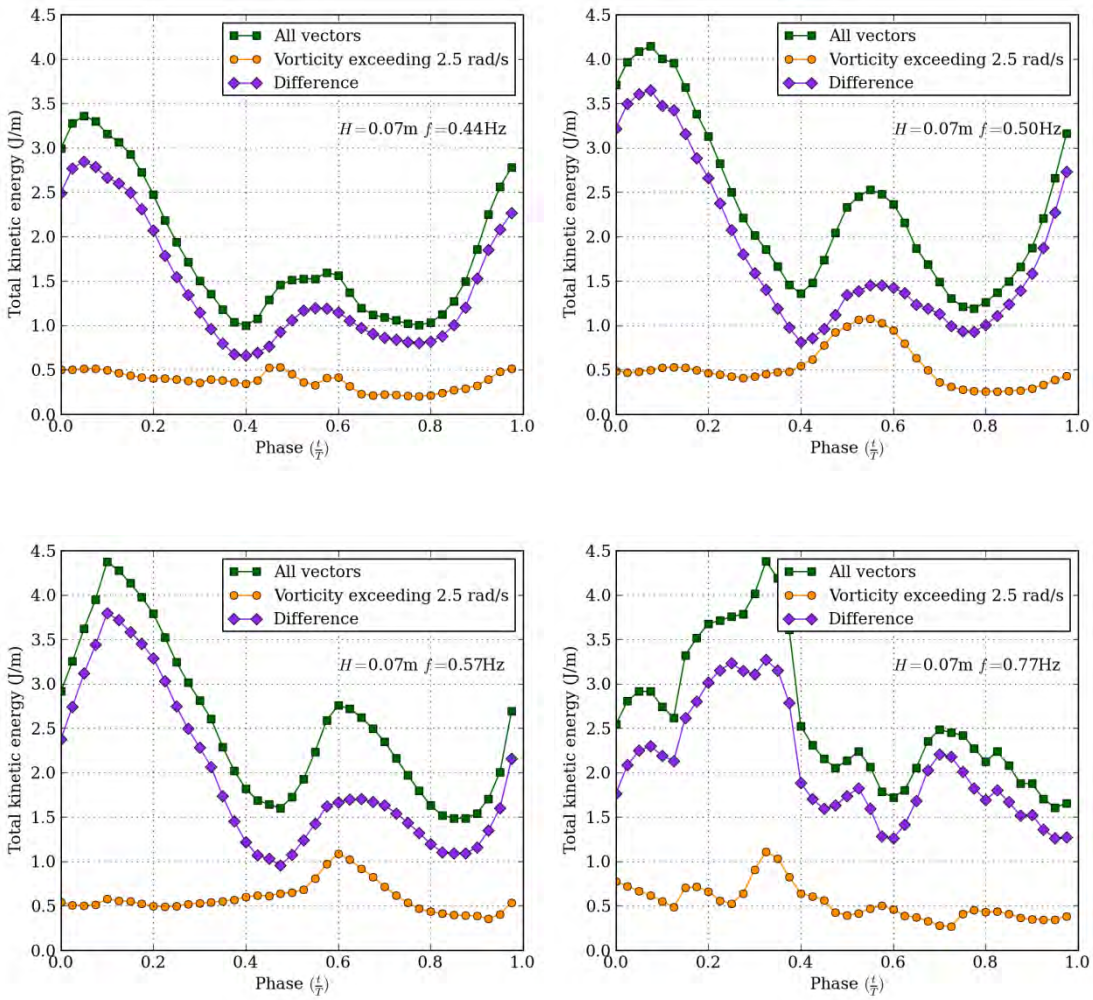

Figure 4.6 Total kinetic energy of velocity fields in the measurement window for vorticity exceeding 2.5rad/s and the difference

Velocity field vectors with a corresponding absolute vorticity exceeding the nominal value of $\omega_{lim} = 2.5$rad/s were identified. The total kinetic energy of the vectors is reported in Figure 4.6 and was representative of the kinetic energy of the water particles in a vortex. The arbitrary selection of the vorticity limit combined with the possibility that the vortex may be transported with the bulk flow prevents this from being a definitive value for the energy bound in vortices but was considered a reasonable estimate of wasteful processes (energy loss). The vorticity limit $\omega_{lim} = 2.5$rad/s was chosen by visual inspection of velocity fields made up of the isolated vectors. The curves of vortex kinetic energy were mostly flat with the exception of the two intermediate frequencies (0.50Hz and 0.57Hz) where there was a significant increase starting around the beginning of water outflow ($t/T = 0.5$) which was mostly associated with an outflow jet above the lower lip. On average, the proportion of energy in vectors with a vorticity exceeding 2.5rad/s to the total energy was 21.7% with a standard deviation of 0.011J/m.

Figure 4.7 shows the total kinetic energy of velocity vectors in the measurement window which have a corresponding absolute vorticity exceeding the minimum vorticity on the x-axis averaged over a wave cycle. For a minimum vorticity equal to zero all vectors are included, which is the same as the mean total kinetic energy in the measurement window over a wave cycle. It is postulated that the shape of the curves is a function of the 'efficiency' of the geometry in the energy conversion process. Comparison of the curves for differing geometry would then provide a quantitative means for the comparison of conversion performance of different underwater geometry.

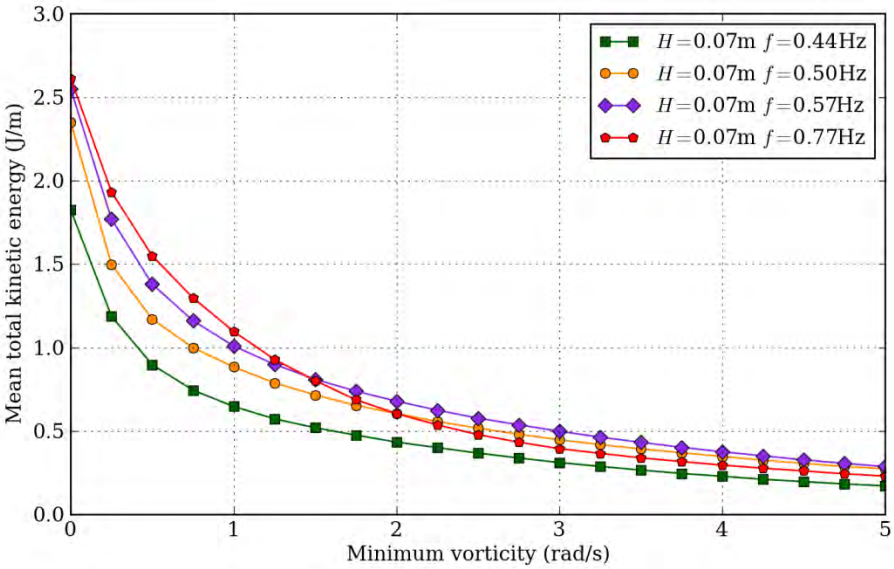

Figure 4.7 Mean total kinetic energy of vectors in the measurement window over a wave cycle with an absolute vorticity exceeding the x-axis value (vorticity)

Figure 4.8 shows the phase-averaged potential energy stored in water column heave over a wave cycle calculated using Equation (4.9). All but the highest frequency wave tested had comparable peaks of water column heave potential energy; in the range of 3.7 – 4.4J/m, while the highest frequency wave had a much lower peak of 2J/m.

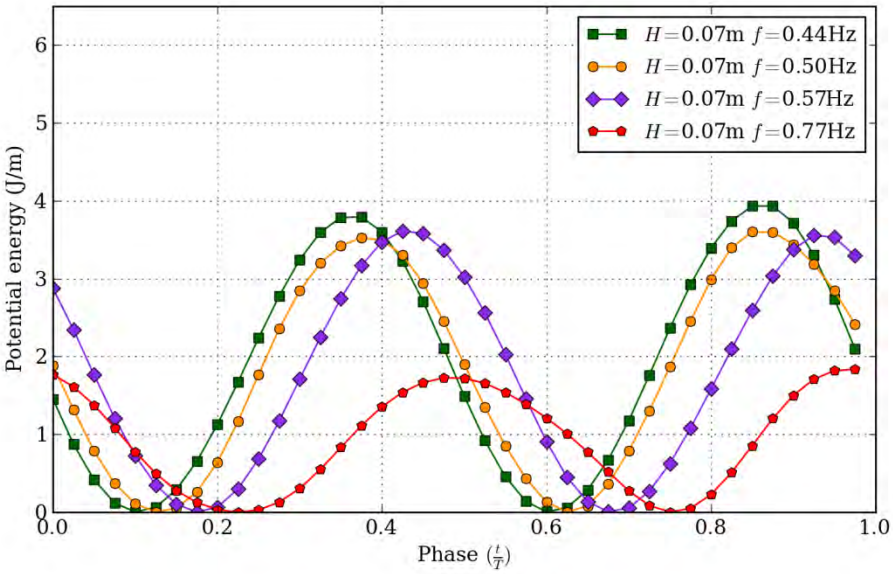

Figure 4.8 Potential energy stored in water column heave

POWER TAKE-OFF

Figure 4.9 shows the phase-averaged power consumed by the PTO over one wave cycle calculated using Equation (4.11). There were two peaks for each curve associated with the inflow and outflow. For all conditions the inflow peak was significantly lower than the outflow peak. The imbalance of energy consumed by the PTO between inflow and outflow suggests that the damping of the water column and power-take-off is causing wave energy to be diverted around the device during the water inflow phase of the wave cycle. Figure 4.9 is characteristic to the 58mm diameter orifice used during experimentation. Using a different sized orifice affects the damping of the device and will yield different power dissipation curves. The curves for the 0.57 and 0.77Hz waves are negative over a small proportion of the wave cycle which is an error associated with both fitting the free surface with a polynomial and air compressibility. 0.57Hz is the known resonant frequency of this OWC arrangement and the curve is most balanced when comparing the first half of the cycle with the second half.

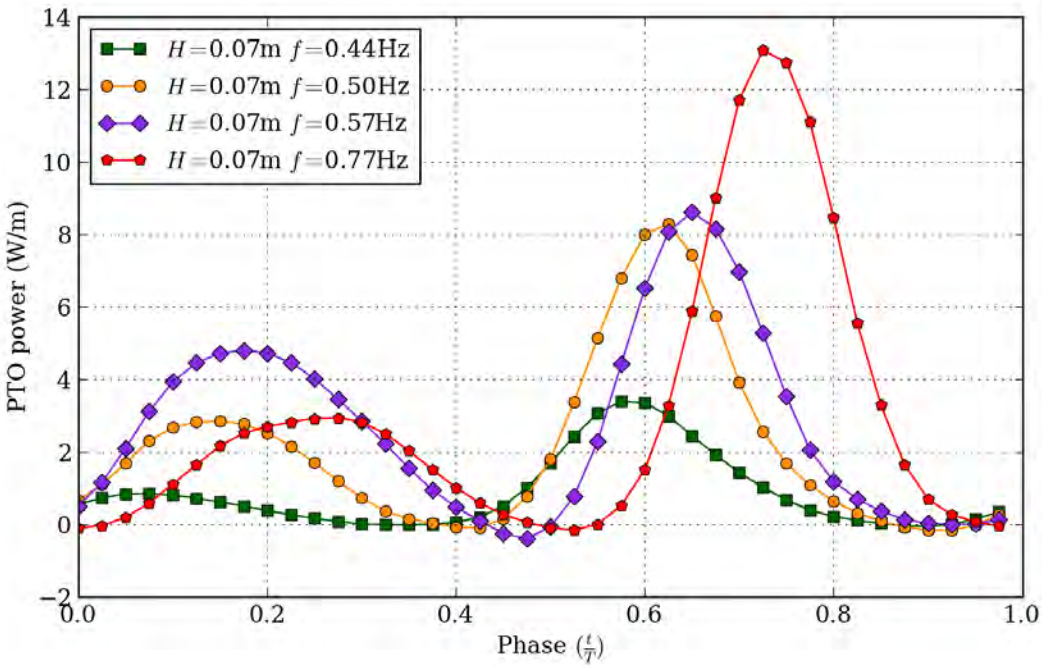

Figure 4.9 PTO power over one wave cycle

Figures 4.10 and 4.11 show the source data used to produce Figure 4.9. Figure 4.10 traces the phase-averaged pressure over a wave cycle for the wave conditions tested. All curves are similar in form but have both amplitude and phase differences. The magnitude of air pressure differential is more pronounced during water outflow in comparison to water inflow.

Figure 4.11 plots the phase-averaged air volumetric flow rate per unit width calculated for the cross-sectional area using wave probe data. Generally the curves are sinusoidal in form but differ by phase a retardation corresponding to an increase in wave frequency. Peak inflow rates were comparable, however, the peak outflow rate was most symmetric for the 0.57Hz wave (closest to the known resonant frequency of the OWC tested). The 0.77Hz wave and to a lesser extent the 0.50Hz wave were observed to experience water column slosh and may be the reason for the deviation of the corresponding curves from pure sinusoidal.

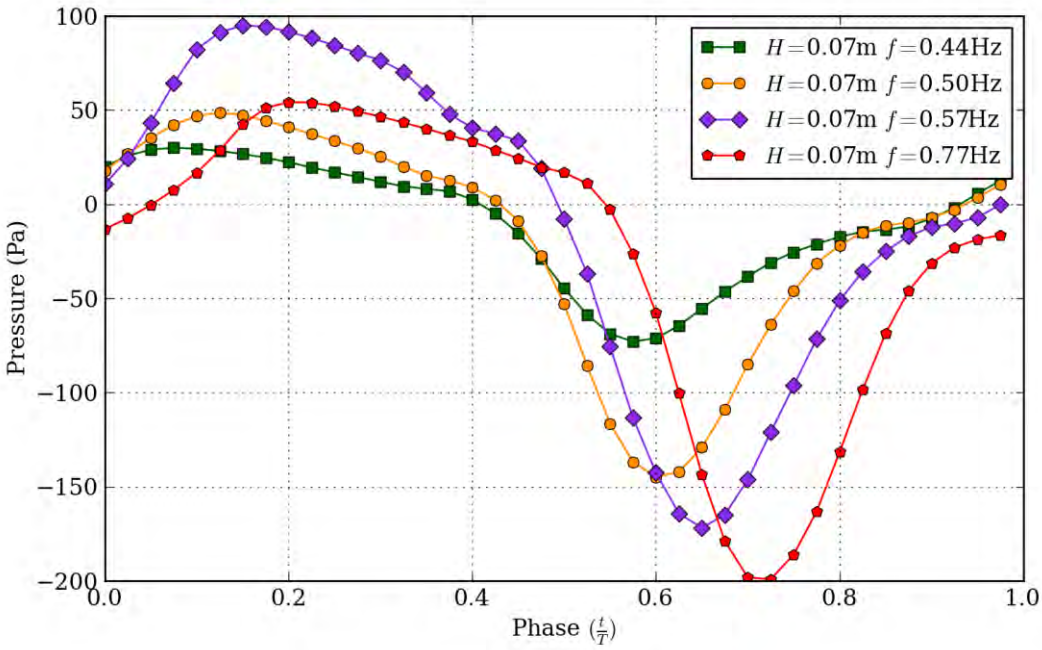

Figure 4.10 Phase-averaged pressure differential between chamber and atmospheric pressure over one wave cycle

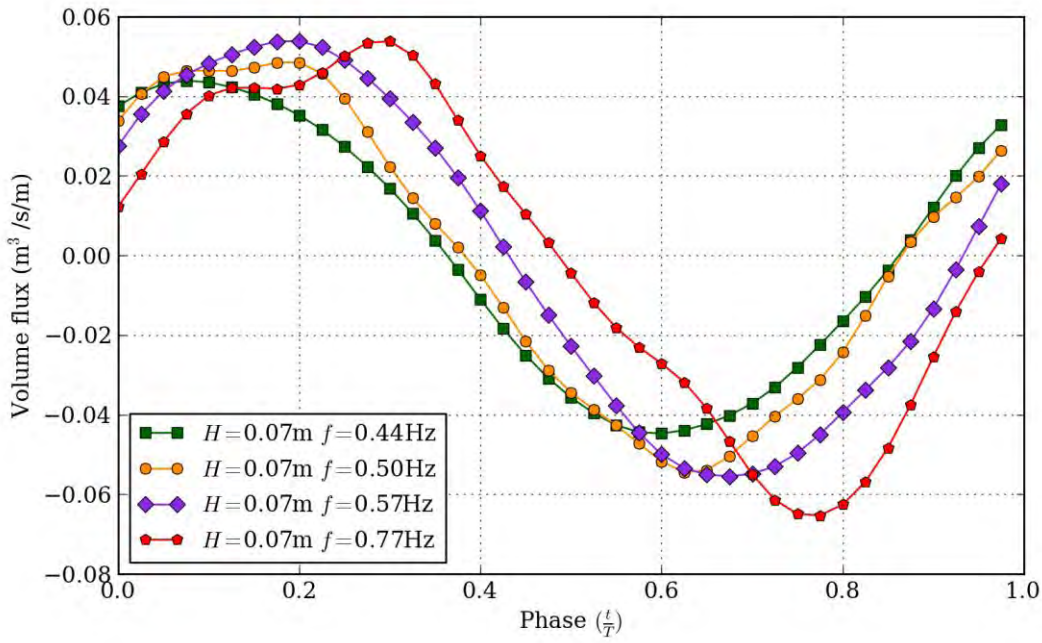

Figure 4.11 Phase-averaged volume flow rate in chamber per m model width over a wave cycle

DISCUSSION

The wave is the only energy source in this analysis. The energy of the incoming wave propagates as a continual transfer between gravitational potential and water particle kinetic energy. Figure 4.3 maps the flow of energy from the wave into and around the OWC as follows:

- Directly into outgoing waves by:
    - Wave diffraction;
    - Wave reflection – direct reflection off the OWC geometry but not including front wall swash/downwash.
- Into intermediate storage:
    - Stored as front wall swash/downwash - where water washes up the front face of the OWC;
    - Water column heave – is the rise and fall of water inside the water column and is the only major route for energy delivery to the power take-off;
    - Water column slosh – a higher order phenomenon caused by uneven flow through the device analogous to slosh in a tank. Water column slosh occurs about the instantaneous mean water level inside the chamber and does not cause a significant volumetric change/pressure differential.
- Vortices - produced at boundaries where flow rapidly changes direction, there are other strong connections to vortices from both front wall swash/downwash and water column heave.

Front wall slosh/downwash, water column heave and water column slosh are all forms of potential energy storage, but with different references in terms of the energy stored. Front wall slosh/downwash and water column heave are both with reference to the still water level while the water column slosh potential is with reference to the instantaneous mean water level inside the OWC chamber.

In Figure 4.3 there is no forward link between vortices and the power take-off, hence, the implication of this is that any energy *stored* in vortices cannot be extracted by the PTO so it is assumed here that all energy contained in a vortex is an energy loss, irrespective of the energy sink following on from the vortex (whether the energy is dissipated within the field of view, or transported away with outflow).

During inflow, wave energy far from the device is being transferred as potential and kinetic energy, but near and inside the device the energy is being transmitted as kinetic energy (motivated by pressured differences), but not as potential energy since the free surface outside the device is not directly connected to the free surface inside the device. The main energy transfer processes observed inside the OWC over a wave cycle are now described:

During inflow, while the mean water level inside the chamber is below the still water level, the primary energy transfer mechanism is from kinetic and potential energy in water column heave to extraction at PTO. When the mean water level inside the chamber is above the still water level the kinetic energy is divided between extraction at the PTO (via water column heave) and storage in water column heave while inflow continues. The secondary or unwanted stores and sinks are the remaining connections to the incoming wave on Figure 4.3 (outgoing waves, front wall swash and vortices). Maximum potential energy stored in water column heave corresponds to the end of inflow and the beginning of outflow. The energy stored as potential energy in the water column heave works in concert with the out flow kinetic energy until the mean water level inside the chamber drops to the still water level, at which time the kinetic energy is then divided between storage in water column heave and extraction at the PTO. The heave is below the still water level but is still seen as positive in magnitude. Again some of the kinetic energy is diverted into the secondary stores and sinks.

For a 100% efficient device we would expect that all of the incoming wave energy flux would be utilised as work performed at the power-take-off. We need to remember that this work involves a finite volumetric displacement which is provided by the displacement of water particles in and around the OWC. Furthermore the water particle displacement must not be transferred into intermediate stores which are not connected to the PTO. The only means of transferring energy to the PTO is via the pressure differential across the PTO which is produced by a volumetric change caused by the movement of the free-surface inside the OWC chamber. Finally, if the OWC system behaves as harmonic device then it has been shown that maximum energy extraction only occurs when kinetic energy and potential energy in the device are equal (Falnes, 2002) - a formidable challenge for the designer to find a geometry which balances kinetic and potential energy for different wave conditions.

The energy balance was used to conveniently identify energy sources, storage and sinks. Experimental data however, does not so conveniently permit the segregation of data because the same physical space is simultaneously occupied by energy storage and transmission of different processes. As a result, kinetic energy calculated for the experimental velocity fields contains all of the energy processes occurring in the measurement window at the same time/phase. From this we assume that proportions of the total kinetic energy of the measurement window are associated with different sources, stores and sinks.

We face a problem here in the velocity fields because we don’t know what energy is incoming and what energy is stored. However we can keep in mind that the device was tested in quasi-steady state conditions so that the current wave may retain residual energy from previous waves stored in one of the storage mechanisms in the energy balance (Figure 4.3) waves are embedded in it.

The presence of the OWC geometry means that there are multiple paths for the storage of potential energy: above the front lip, as swash; and inside the water column as heave and water column slosh. Problems associated with storage of energy in the front wall swash include: Phase differences with the water column heave which generally oppose energy extracting and introduce higher order phenomena namely water column slosh (Folley and Whittaker, 2002). Kinetic energy was returned from front wall swash before OWC bulk flow reversal occurred. The result being that the flow was directed into to the OWC causing water column slosh. Separation of flow also occurred at the upper lip causing the generation of clockwise rotating vortices.

CONCLUSIONS

Energy balance is a simple method to account for non-linear characteristics in wave energy conversion with particular relevance to the analysis of experimental velocity fields i.e. PIV data. To improve OWC geometry it is necessary to understand how the energy is being converted. Two-dimensional PIV phase-averaged analysis is a powerful tool to facilitate the understanding and quantification of some of these processes. We have used the energy balance to conclude that vortices are an energy loss mechanism regardless of how the energy is eventually lost. The kinetic energy of water particles with an absolute vorticity above 2.5rad/s accounted for on average 21.7% of the mean total kinetic energy in the measurement window and was found to be relatively constant over a wave cycle in contrast to large variations in the total kinetic energy.

The energy balance analysis has allowed us to draw some general considerations when designing the forward-facing bent-duct OWC:

- Sharp changes in direction of surfaces is undesirable because it inevitably causes vortex generation due to separation of the flow – remembering that vortices are an irreversible temporary storage process which for our purposes will be considered a loss;
- Front wall swash/downwash should be minimised. This can be achieved by redesign of the upper lip;

Phase-averaged air chamber pressure differential was observed to have a lower magnitude during water inflow compared to water outflow in the wave cycle for all wave frequencies tested and was concluded that for the forward-facing bent-duct OWC, the damping by the orifice (PTO) causes diversion of energy around the device during the water inflow part of the cycle.

REFERENCES

Dean, R.G., Dalrymple, R.A., 1991. Water Wave Mechanics for Engineers and Scientists, Advanced Series on Ocean Engineering. World Scientific.

Demirbilek, Z., Vincent, C.L., 2002. Water Wave Mechanics. Chapter II-1, in: Coastal Engineering Manual (EM 1110-2-1100). US Army Corps of Engineers, Washington, D.C., p. 121.

Evans, D.V., 1982. Wave-Power Absorption by Systems of Oscillating Surface Pressure Distributions. Journal of Fluid Mechanics 114, 481–499.

Falnes, J., 2002. Ocean Waves and Oscillating Systems. Cambridge University Press.

Fleming, A., Penesis, I., Goldsworthy, L., Macfarlane, G., Bose, N., Denniss, T., 2011. Phase Averaged Flow Analysis in an Oscillating Water Column Wave Energy Converter, in: Proceedings of the ASME 2011 30th International Conference on Ocean, Offshore and Arctic Engineering. Rotterdam, The Netherlands.

Fleming, A., Penesis, I., Macfarlane, G., Bose, N., Hunter, S., 2012. Phase-averaging of Velocity Fields in an Oscillating Water Column Using Splines. Proceedings of the Institution of Mechanical Engineers, Part M: Journal of Engineering for the Maritime Environment.

Folley, M., Whittaker, T., 2002. Identification of Non-Linear Flow Characteristics of the Limpet Shoreline OWC, in: Proceedings of the Twelfth (2002) International Offshore and Polar Engineering Conference, May 26,2002 - May 31,2002, Proceedings of the International Offshore and Polar Engineering Conference. International Society of Offshore and Polar Engineers, Kitakyushu, Japan, pp. 541–546.

Forestier, J.-M., Holmes, B., Barrett, S., Lewis, A.W., 2007. Value and Validation of Small Scale Physical Model Tests of Floating Wave Energy Converters, in: Proceedings of the 7th European Wave and Tidal Energy Conference (EWTEC 2007). Presented at the 7th European Wave and Tidal Energy Conference (EWTEC 2007), Porto, Portugal.

Graw, K.U., Schimmels, S., Lengricht, J., 2000. Quantifying Losses Around the Lip of an OWC by Use of Particle Image Velocimetry (PIV). Presented at the Fourth European Wave Energy Conference, LACER-Leipzig Annual Civil Engineering Report, Aalborg, Denmark.

Oliphant, T., Ascher, D., 2001. NumPy: Numerical Python. Lawrence Livermore National Laboratory, Livermore, California, USA. Available at: http://numpy.scipy.org/.

5

PHASE-AVERAGING ERROR ANALYSIS

This chapter is unpublished and not presently under consideration for publication. The premise of the chapter was to evaluate the performance of curve-fitting algorithm using splines and to introduce a new *hybrid* ensemble-averaging phase-averaging algorithm.

INTRODUCTION

An error analysis was conducted to test the performance of the curve-fitting phase-averaging algorithm which was described in detail in Chapter 3. To enable a performance comparison between curve-fitting and ensemble-averaging a new hybrid ensemble-phase-averaging algorithm was developed. In this chapter the characteristics of the new hybrid algorithm are described followed by results of the error analysis. The performance of the newly developed hybrid algorithm only exceeded the performance of curve-fitting algorithm in terms of maximum and average error when processing heavily phase clumped sample data. The original spline fitting method presented in Chapter 3 yielded lower maximum and average error for non-clumped test data and remains the recommended method for phase-averaging data which has the phase allocated with a synchronising signal.

HYBRID ENSEMBLE-PHASE-AVERAGING

Chapter 3 highlighted the deficiencies of the ensemble-averaging algorithm when using a synchronising signal on clumped periodic data notably:

- Phase bias error (if the data is clumped and away from the central frequency)
- Inability to differentiate between non-continuous regions and missing data
- Requirement for a fixed number of bins (phases)

The hybrid phase-averaging algorithm utilises modified ensemble-averaging techniques to generate phase-averaged data which is then interpolated to the desired phase using splines. The algorithm combines the stability of ensemble-averaging with the flexibility of splines and providing the following characteristics:

- Automatic bin selection
- Phase bias error correction
- Automatic interpolation of fit in the phase range $0 < \frac{t}{T} < 1$
- Automatic interpolation of uncertainty in the phase range $0 < \frac{t}{T} < 1$
- Identification of non-continuous regions
- Specification of the minimum number of samples permitted for averaging in a bin
- Control over smoothing

Input parameters for the algorithm are shown in Table 5.1 while input data was the same as in Chapter 3 of the type:

- Phase sorted instantaneous velocity fields (v): shape = (frames, ny, nx)
- Phase corresponding to velocity field: shape (p) = (frames)

Table 5.1 Input parameters for hybrid ensemble-averaging

Parameter	Option	Description
$pmode$	'central' or 'average' Default = 'average'	Mode to determine phase, 'central' specifies the centre of the bin, 'average' specifies the average phase of the data in the corresponding bin
$nmin$	Integer > 2 Default=14	Minimum number of data points in a bin to ensemble average. Insufficient data points are populated with the value 'nan'
$bins$	None or integer > 15 Default = None	Option to override the number of bins
s	None or 0	If None, automatic smoothing is used. If 0, No smoothing is used

Automatic bin selection was performed once per phase sorted velocity field, meaning the number of bins was also constant for a velocity field. The number of bins was chosen by iterating over the range $15 > \text{bins} > \max(\frac{\text{frames}}{\text{nmin}}, 16)$ and selecting the histogram with corresponding maximum number of bins which exceeded $nmin$. The purpose being to maximise the number of bins with valid data points provided for spline interpolation which minimises bin width as well as minimising spline instability.

Data was phase-averaged on a pixel by pixel basis using the number of bins previously calculated. When the input parameter $pmode$ was set to "average" the ensemble average was performed on the phase in addition to the magnitude – essentially eliminating phase bias error. However the phase for each bin is then unique meaning interpolation was necessary to ensure phase consistency between pixels (which was performed by spline interpolation).

An array of uncertainty values was produced at the same time as the array of ensemble-averaged values. The uncertainty was calculated as:

$$u = \frac{k\sigma}{\sqrt{n}} \tag{5.1}$$

where $k = 2$ corresponds to a 95% confidence interval, σ is the standard deviation of the magnitude of the data points in the bin and n is the number of data points in the bin. The inverse of the uncertainty values were used as weightings for spline interpolation when smoothing (s) was set to 'None' (automatic).

The same B-spline functions were used as in Chapter 3 to interpolate the ensemble-averaged phases and magnitudes. Invalid data was considered as a bin containing fewer than $nmin$ data points and was invalidated using the quantity 'nan', these datapoints were removed prior to spline interpolation. The periodic mode was disabled since it was not possible to ensure start and finish overlap and data range was extended to the phase range $-0.3 < \frac{t}{T} < 1.3$ by repeating data at each end. A cubic spline fit was specified except when the number of data points was less than the order of the spline; the order was then reduced to match the number of data points. Non-continuous data was identified from the ensemble-averaged data using the same method as described in Chapter 3. However contiguous regions were considered as three adjacent regions of valid data rather than two adjacent regions.

RESULTS

ERROR ANALYSIS

The operational characteristics of the phase-averaging algorithms were tested by obtaining the difference between a known signal and the phase-averaged fit to the simulated sample. Simulated data was produced according to the test matrix shown as Table 5.2. Test data was randomised in phase with maximum deviations of 0.3 (error ratio) from real signal and randomised in amplitude using a Gaussian randomisation of standard deviation of 0.15. Axes 'y' was populated with sinusoidal data of the corresponding harmonic randomised in phase. A es ' ' was populated with the superposition of the 'y' harmonic components up to the corresponding harmonic. Only the error for the superposition harmonics are reported here which most closely resembles real world data.

Table 5.2 Error analysis test matrix

Parameter	Value	Conditions
(Clumps, Clump width)	(1, 1), (8, 0.8), (0, 0.2)	3
Harmonics	0-10	11
Samples	200, 600, 1200, 2000,2800	5
Axes	x, y	2
Repeats		10
Product		3300

Table 5.3 Labels and parameters used for phase average error analysis

Nickname	Phase-averaging class	Parameters
Spline	VecPolyBSpline	s=None nmin=0.07 conditioners=('b','d')
EA average	VecEA	pmode='average' nmin=7 s=None
EA central	VecEA	pmode='central' nmin=17 s=0

A typical fit of clumped sample data is shown in Figure 5.1; details of the source of the curves are provided in Table 5.3. The sample shown is of a second-harmonic superposition with 600 samples clumped around eight phases. *EA average* provides the best visual fit, while *EA central* and *Spline* deviate from the original curve. *EA average* deviates due to phase bias error while *Spline* deviates due to incorrect assumptions made about trends in the data. It follows in the results presented here that *EA average* produces the lowest error for heavily phase clumped data with when zero or more than one harmonic components are present and less than 800 samples are provided, which is most representative of the experimental data used in this thesis.

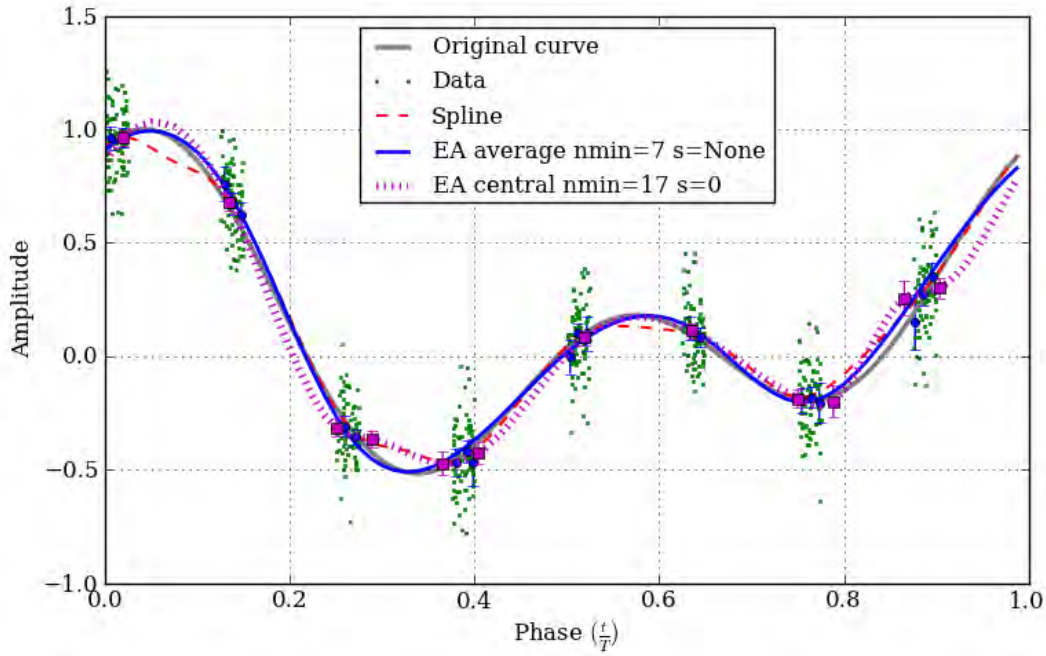

Figure 5.1 Curve-fitting applied to a second-harmonic superposition sample with 8 clumps, 0.2 clump width and 600 data points

Maximum and mean error values were obtained for each point on the original curve (80 points were used). Error was taken as the difference in magnitude between the original curve and the phase-averaged result. Performance characteristics will now be presented based on various scenarios extracted from results error analysis in accordance with the test matrix shown in Table 5. 2.

Figure 5.2 shows the maximum errors for 0.8 width clump data. Up to two harmonics both *Spline* and *EA average* have a reduction in maximum error when the number of samples is increased. *EA central* has the greatest error which increases with an increased number of samples; the error is due to phase bias error.

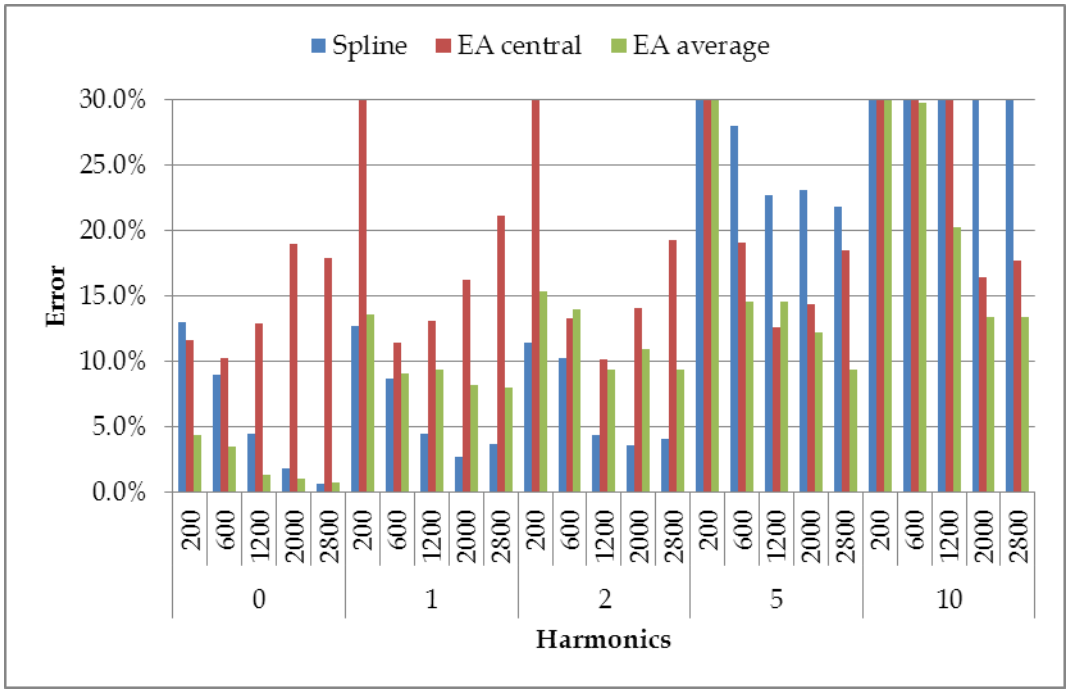

Figure 5.2 Maximum error for 8 clumps, 0.8 clump width, superposition of harmonic components (x-component)

Figure 5.3 shows the maximum errors for 0.2 width clumped data. There was a reduction in error for all algorithms when less than two harmonics were considered. When more than one harmonic was used the error was greater than in Figure 5.2 which was due to the absence of information between data clumps necessary for the algorithms to identify the higher order components. Which emphasises the negative effect phase-clumping has on data analysis quality when a synchronising signal is used. *EA average* has the lowest error when more than two harmonics are considered however at two harmonics the error is approaching ten percent.

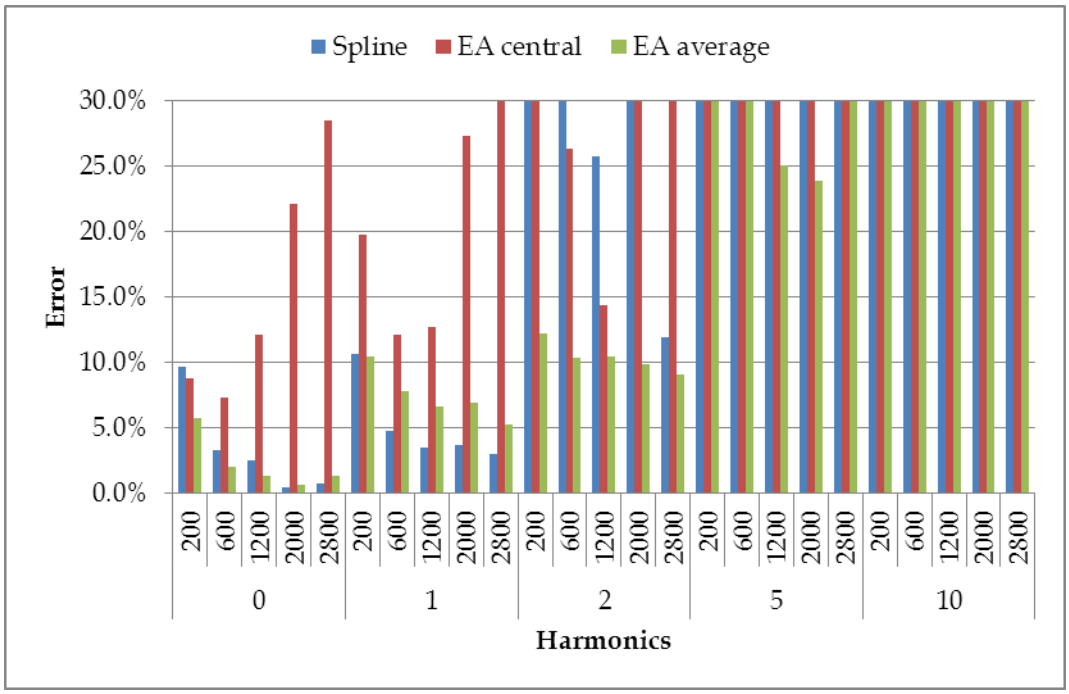

Figure 5.3 Maximum error for 8 clumps, 0.2 clump width, superposition of harmonic components (x-component)

Figure 5.4 shows the maximum error for the algorithms applied to non-clumped data. *EA average* has the lowest error for 0th harmonic signal (analogous to nothing happening) which has lower importance in terms of data analysis for periodic flows since the presence of at least one harmonic component is expected. S*pline* produces the lowest error when more than one harmonic is considered and has a reduction in error corresponding to an increase in the number of samples up to 2000 samples.

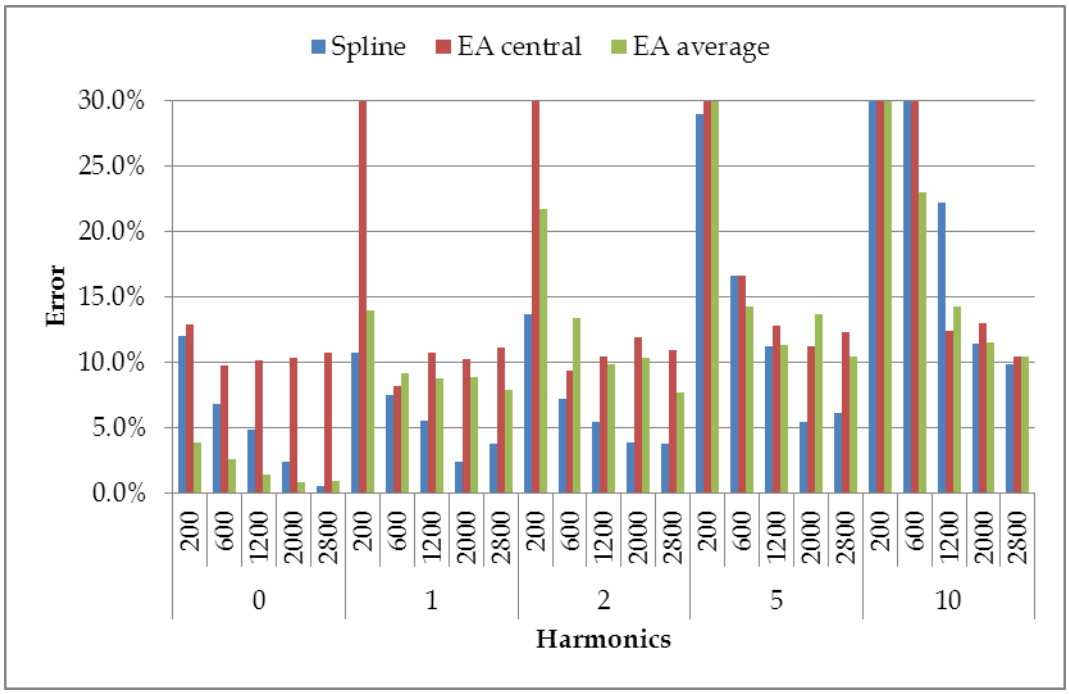

Figure 5.4 Maximum error for 1 clump, 1.0 clump width, 'x' component

Figure 5.5 shows the **average** error for the algorithms tested applied to non-clumped data. *Spline* (with few exceptions) yields the lowest average error for between 1 and 5 harmonics. The reason for this is that the trend of the data is used in addition to the average values and uncertainty and therefore most efficiently uses the data. Spline however, presently uses 41 bins for phase averaging which limits the number of harmonics that can be investigated.

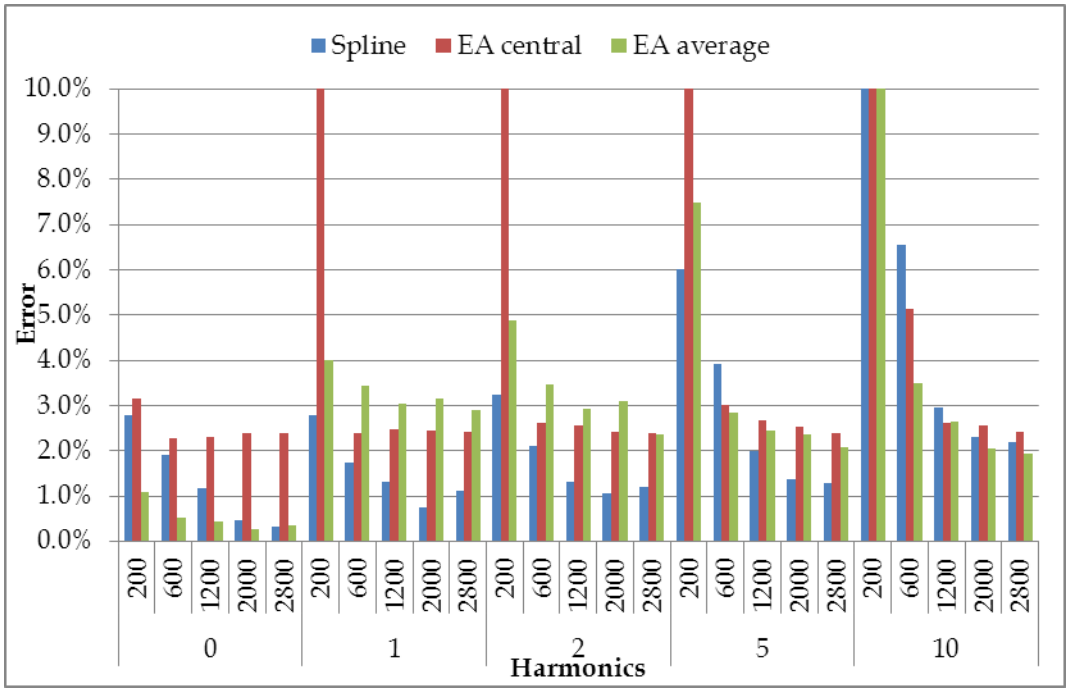

Figure 5.5 Average error for 1 clump, 1.0 clump width, superposition of harmonic components (x-component)

CURVE-FITTING PERFORMANCE COMPARISON

This section applies the same phase-averaging algorithms defined in the previous section (as detailed in Table 5.3) to the same samples from Chapter 3 (Fleming *et al.*, 2012) (see Table 3.3) to enable a qualitative performance comparison of the phase-averaging algorithms. Magenta squares mark the ensemble-average and uncertainty used for *EA central* and blue circles mark the ensemble-average and uncertainty for *EA average*.

Figure 5.6 is the vortex transit sample which has eight data clumps. Visually *EA Average* and *Spline* provide consistent results while *EA central* shows phase bias error, apparent where the marker does not coincide with the data points which causes its curve to overshoot at $\frac{t}{T} = 0.3$ & 0.5.

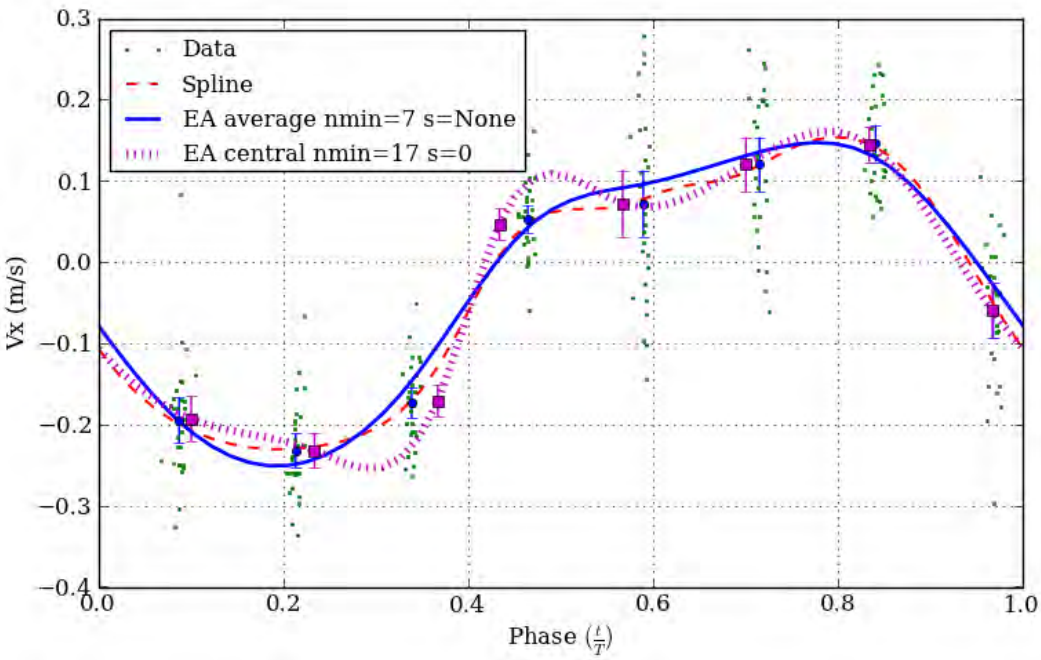

Figure 5.6 Vortex transit (sample 1) Spline average and ensemble average fit (horizontal component)

The discontinuous data sample is shown in Figure 5.7. All curves are in general agreement and successfully identify the discontinuous region. *Spline* exhibits some instability due the clumped data which is present as a *wobble* between the clumps. *EA central* exhibits minor phase bias error at $\frac{t}{T} = 0.4$. *EA average* is smooth and visually provides the best fit to the data.

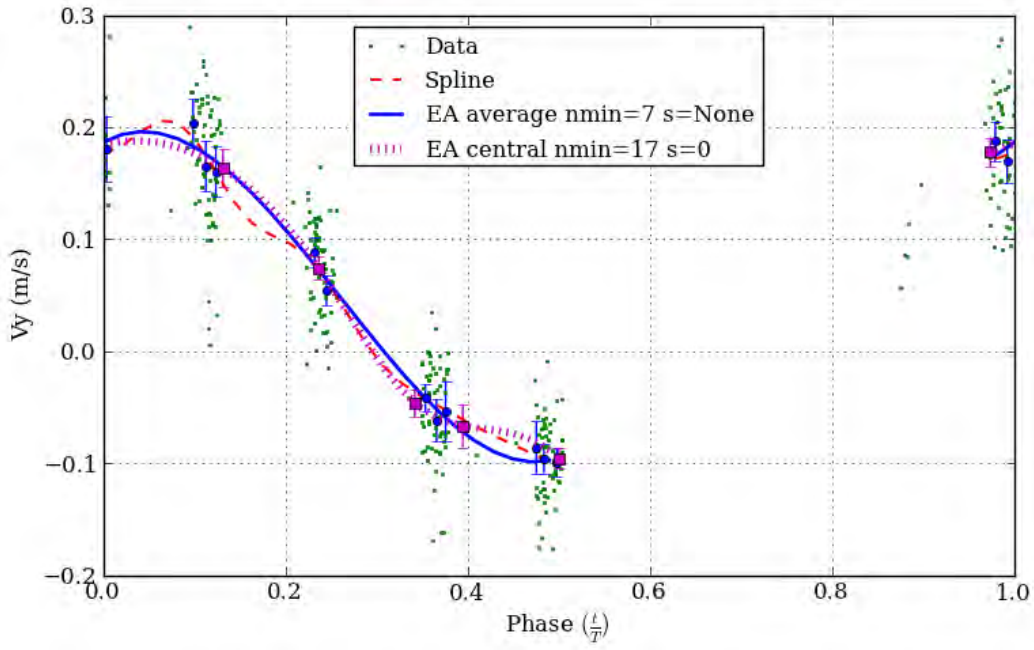

Figure 5.7 Discontinuous data (sample 2) spline average and ensemble average fit (vertical component)

The water column slosh sample is shown in Figure 5.8 which uses 915 data points (Table 3.3) with a reduced amount of clumping compared to the other two examples. All curves are in general agreement; *EA Average* is smooth while *EA Central* is jagged due to the absence of smoothing meaning that a greater $nmin$ would be required for classical ensemble averaging. *Spline* was smooth and appears to follow the trend of the data.

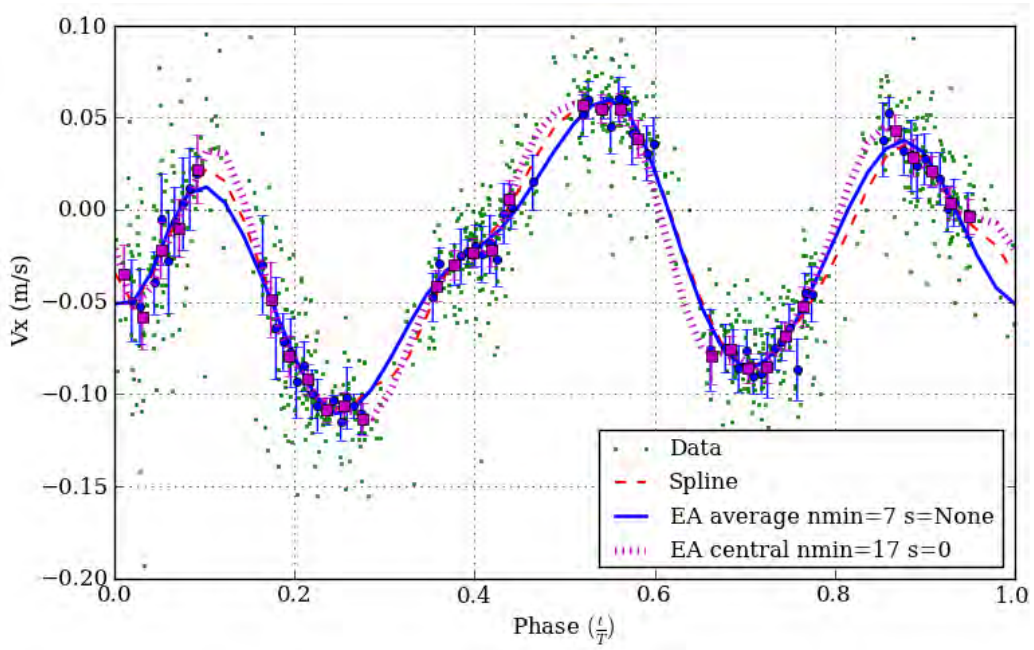

Figure 5.8 Water column slosh (sample 3) spline average and ensemble average fit (horizontal component)

CONCLUSIONS

The error analysis shows that *EA average* with automatic smoothing ($s = None$) was superior to *Spline* when fitting heavily clumped periodic data (8 clumps with clump width of 0.2) for all harmonics tested except the first harmonic signal. Since most of the experimental data was heavily phase clumped the velocity fields have been produced for the four wave frequencies tested using the *EA average* using nmin = 7 and automatic smoothing and are provided in Appendix B for reference. *EA average* is a more generic algorithm for phase averaging and is best applied to non-clumped data using the parameters $s = 0$ and $nmin \geq 17$ or to heavily clumped data using the parameters $s = None$ and $nmin = 7$.

Clumping of data in phase should be avoided when data is acquired for phase-averaging with a synchronisation signal (not encoder base). Clumping is avoided by selecting a data acquisition rate which is not an integer fraction of the phase frequency. This is especially important for PIV type data where the acquisition rate is low compared to other data acquisition rates (5Hz for PIV compared to 100 or 1000Hz for wave probe and pressure transducer data).

Phase-averaging of between one and five harmonics of non-clumped periodic data will produce lower error when using S*pline* compared to *EA average* and *EA central* when up to 2000 samples are used. Spline however does not presently provide uncertainty information and should be incorporated into future versions of the algorithm.

For PIV data in OWCs the first and second harmonics will contain the bulk flow information (including vortices), whilst the higher harmonics will contain turbulence information. Since turbulence is random by its very nature then phase-averaging should concentrate on the lower harmonics. Based on this assumption and the test data with an error ratio of 0.3 it was found that phase-averaging using *Spline* has notable reduction in error when up to 1200 samples and to continues to improve in accuracy up to 2000 samples, above which the reduction in error is minimal (Figure 5.4 and Figure 5.5).

6

CONCLUSIONS AND FURTHER WORK

CONCLUSIONS

In this thesis, phase-averaging has been applied to experimental data involving a three-dimensional model of a forward-facing bent-duct OWC exposed to monochromatic waves. Phase-averaged 2D PIV data was explored qualitatively using vector representation of the velocity fields to show the average 2D flow field inside and around the OWC at its centreline. Quantitative analysis was conducted in the form of an energy balance analysis which utilised phase-averaged 2D velocity fields, wave probe and pressure transducer data to explore the flow of energy from the incoming waves, into stores and sinks.

Results presented in this thesis can be used in validation of CFD numerical wave tanks (replicating this geometry and the conditions tested). The methods for phase-averaging using splines presented in Chapter 3, or the hybrid ensemble-averaging method presented in Chapter 5 are both superior to ensemble-averaging in the instance where a synchronising signal is used and there is limited data available (less than 2000 data points). The energy balance method presented in Chapter 4 is convenient for combining data of different types, is compatible with the phase averaging techniques, and gives a clear graphical representation of the flow of energy through the system. From the incoming wave, through the wave energy converter, to the various stores and sinks.

Visualisation of the velocity fields revealed import details about the average flow inside the device at different wave frequencies (Chapters 2&3). A constant theme between the frequencies was the presence of vortices generated by the sharp edges of the upper lip, lower lip and corner between the front wall of the OWC chamber and the upper lip. Comparing the total kinetic energy of a velocity field with the kinetic energy of the water particles coinciding with vortices was proposed as a measure of the energy not available for extraction by the power-take-off. However it was conceded that this was an overestimate since not all of the kinetic energy was associated with the vortex (generally the water particle is also involved in bulk flow) hence explicit values should not be reported. Using this information - new geometry can be designed to avoid the generation of vortices from the sharp edges. The proportion of kinetic energy in vortices can then be compared between the new and old geometry.

Other flow field phenomena observed was an outflow jet which occurred above the lip and was associated with the vortex at the same location. The outflow from the OWC combined with the anti-clockwise rotating vortex beginning at $\frac{t}{T}$=0.5 and continuing until approximately $\frac{t}{T}$=0.62. The outflow jet had lowest intensity for the highest frequency wave tested. The outflow jet was considered to be associated with an inefficiency of the geometry and would be absent at optimal operation of the OWC.

A large amount of the data in the raw velocity fields was reduced by means of phase-averaging which enabled the following enhancements for data interpretation:

- Combination of velocity fields from separate positions using wave-phase of the same wave conditions to create a mosaic of velocity fields;
- Visualisation of velocity fields over a wave cycle to represent the average 2D flow in the measurement plane;
- Combine quantitative analysis of phase-averaged velocity fields with phase-averaged wave probe and pressure transducer data to perform an energy balance analysis;
- Comparison of any phase-averaged data from different wave conditions on a phase by phase basis or mean over wave cycle basis including: Amplitude of oscillation, chamber pressure, kinetic energy and power.

Experimental data destined for phase-averaging using a synchronisation signal (as opposed to encoder based synchronisation) should be acquired so as to avoid phase clumping. It is recommended to use curve-fitting phase-averaging which will yield the lowest error to sample ratio (assuming the data is similar to that tested) with a recommended minimum of 200 samples over a periodic cycle. The reader can refer to Figure 5.4 for estimates of maximum phase-averaged error and Figure 5.5 for average phase-averaged error, based on the number of samples, harmonic components for an error ratio of 0.3. Increasing the number of samples provided for phase-averaging up to 2000 samples will produce reduced uncertainty in phase averaged results when using the curve fitting algorithm detailed in Chapter 3.

Dissipation should not be directly calculated from PIV velocity fields because PIV velocity fields are spatially averaged, and are normally acquired at much larger scale than the scale at which dissipation takes place (Taylor's microscale). It may be possible to estimate the dissipation using various methods (for example see Huang *et al*. (2009)), however; the methods require calibration and validation for each separate experiment and the value of knowing dissipation in the context of wave energy conversion is questionable.

The PTO power was observed to be lower during water inflow into the OWC compared to water outflow. This was attributed to the damping in the PTO (orifice) causing the diversion of energy around the OWC during the water inflow part of the wave cycle. The implication being that the OWC device may achieve better operational efficiency if designed to minimise damping during water inflow. This may be achieved through the implementation of OWC chamber venting in combination with a unidirectional turbine. In my opinion the use of a unidirectional turbine offers several advantages compared to a bi-directional turbine including: off the shelf machines (cheaper), higher operational efficiency, lower exposure to atomised water since the turbine

would operate on air inflow. The concept however does require validation (experimental or numerical) and assumes the future design of a high volume low pressure chamber venting system is achievable.

FURTHER WORK

There are several avenues for further work. The most important of these is to investigate the magnitude of the third velocity component (crosswise) of the PIV velocity fields, which was assumed to be negligible in this study. Ideally for this study, all three velocity components should have been acquired simultaneously (3D PIV). Practical limitations including: equipment cost/availability, experimental complication and optical access are all barriers to the implementation of 3D PIV. The alternative being to use 2D PIV on a different plane which is what is recommended here.

The effect of differing geometry is also of great interest and was one of the reasons for this investigation. An ARC linkage grant involving Oceanlinx and the Australian Maritime College (UTAS) has recently been created for the purpose of investigating the effect of changing OWC underwater geometry using experimental and numerical methods.

In this study the raw 2D PIV velocity fields were decomposed using phase-averaging. Other decomposition techniques are available and should be investigated including Proper Orthogonal Decomposition. The phase averaged data can also be used in other analyses for example dividing the velocity fields into harmonic components.

The phase-averaging techniques can also be extended to the investigation of polychromatic (periodic) seas but issues will need to be addressed surrounding how to conduct the experiment and how to apply the instantaneous phase. Using polychromatic seas is a step towards real world conditions.

It may be possible to gain better insight into the mechanism of added mass in terms of the OWC and how this impacts on the response of the OWC on the incoming wave field. This information would be useful in terms of OWC design and numerical modelling (in both the time and frequency domain). The added mass is considered the mass of the water that acts as a solid body and should exhibit behaviour similar to a solid body.

7

BIBLIOGRAPHY

Adrian, R.J., 1997. Dynamic Ranges of Velocity and Spatial Resolution of Particle Image Velocimetry. Measurement Science and Technology 8, 1393–1398.

Aqua-RET, 2009. Aquatic Renewable Energy Technologies [WWW Document]. URL http://www.aquaret.com

Ariyarathne, H., 2007. Efficiency of Perforated Breakwater and Associated Energy Dissipation (Masters thesis).

Barstow, S.F., Falnes, J., 1996. Ocean Wave Energy in the South Pacific: The Resource and its Utilisation. South Pacific Applied Geoscience Commission in conjunction with the Government of Norway.

Brooke, J. (Ed.), 2003. Wave Energy Conversion, 1st ed, Elsevier Ocean Engineering Book Series. Elsevier, Boston, MA, United states.

Clément, A., McCullen, P., Falcão, A., Fiorentino, A., Gardner, F., Hammarlund, K., Lemonis, G., Lewis, T., Nielsen, K., Petroncini, S., Pontes, M.-T., Schild, P., Sjöström, B.-O., Sørensen, H.C., Thorpe, T., 2002. Wave energy in Europe: current status and perspectives. Renewable and Sustainable Energy Reviews 6, 405–431.

Cruz, J. (Ed.), 2008. Ocean Wave Energy: Current Status and Future Perspectives. Springer Verlag.

Dean, R.G., Dalrymple, R.A., 1991. Water Wave Mechanics for Engineers and Scientists, Advanced Series on Ocean Engineering. World Scientific.

Demirbilek, Z., Vincent, C.L., 2002. Water Wave Mechanics. Chapter II-1, in: Coastal Engineering Manual (EM 1110-2-1100). US Army Corps of Engineers, Washington, D.C., p. 121.

Dierckx, P., 1993. Curve and surface fitting with splines. Oxford University Press, USA.

Emarat, N., Christensen, E.D., Forehand, D.I.M., Mayer, S., 2000. A Study of plunging breaker mechanics by PIV measurements and a Navier-Stokes solver, in: Coastal Engineering 2000 - Proceedings of the 27th International Conference on Coastal Engineering, ICCE 2000. pp. 891–901.

EMEC, 2009. EMEC: European Marine Energy Centre - Orkney [WWW Document]. URL http://www.emec.org.uk/index.asp

Evans, D.V., 1978. The Oscillating Water Column Wave-energy Device. IMA Journal of Applied Mathematics 22, 423 –433.

Evans, D.V., 1982. Wave-Power Absorption by Systems of Oscillating Surface Pressure Distributions. Journal of Fluid Mechanics 114, 481–499.

Falcão, A.F. d. O., 2010. Wave energy utilization: A review of the technologies. Renewable and Sustainable Energy Reviews 14, 899–918.

Falnes, J., 2002. Ocean Waves and Oscillating Systems. Cambridge University Press.

Falnes, J., 2007. A Review of Wave-Energy Extraction. Marine Structures 20, 185–201.

Di Felice, F., De Gregorio, F., Felli, M., 2000. Ship model wake analysis by means of PIV in large circulating water channel, in: Proceedings of the International Offshore and Polar Engineering Conference. pp. 392–397.

Felli, M., Falchi, M., Pereira, F., 2010. Distance effect on the behavior of an impinging swirling jet by PIV and flow visualizations. Experiments in Fluids 48, 197–209.

Felli, M., Pereira, F., Calcagno, G., Di Felice, F., 2002. Application of Stereo-PIV: Propeller Wake Analysis in a Large Circulating Water Channel, in: 11th International Symposium on Applications of Laser Techniques to Fluid Mechanics. Lisbon, Portugal.

Felli, M., Roberto, C., Guj, G., 2009. Experimental analysis of the flow field around a propeller–rudder configuration. Experiments in Fluids 46, 147–164.

Filianoti, P., Camporeale, S.M., 2008. A linearized model for estimating the performance of submerged resonant wave energy converters. Renewable Energy 33, 631–641.

Fleming, A., Penesis, I., Macfarlane, G., Bose, N., Denniss, T., 2012. Energy balance analysis for an oscillating water column wave energy converter. Ocean Engineering 54, 26–33.

Fleming, A., Penesis, I., Goldsworthy, L., Macfarlane, G., Bose, N., Denniss, T., 2011. Phase Averaged Flow Analysis in an Oscillating Water Column Wave Energy Converter, in: Proceedings of the ASME 2011 30th International Conference on Ocean, Offshore and Arctic Engineering. Presented at the OMAE 2011, Rotterdam, The Netherlands.

Fleming, A., Penesis, I., Macfarlane, G., Bose, N., Hunter, S., 2012. Phase Averaging of Velocity Fields in an Oscillating Water Column Using Splines. Proceedings of the Institution of Mechanical Engineers, Part M: Journal of Engineering for the Maritime Environment.

Folley, M., Whittaker, T., 2002. Identification of Non-Linear Flow Characteristics of the Limpet Shoreline OWC, in: Proceedings of the Twelfth (2002) International Offshore and Polar Engineering Conference, May 26,2002 - May 31,2002, Proceedings of the International Offshore and Polar Engineering Conference. International Society of Offshore and Polar Engineers, Kitakyushu, Japan, pp. 541–546.

Folley, M., Whittaker, T., 2009. The effect of sub-optimal control and the spectral wave climate on the performance of wave energy converter arrays. Applied Ocean Research 31, 260–266.

Forestier, J.-M., Holmes, B., Barrett, S., Lewis, A.W., 2007. Value and Validation of Small Scale Physical Model Tests of Floating Wave Energy Converters, in: Proceedings of the 7th European Wave and Tidal Energy Conference (EWTEC 2007). Presented at the 7th European Wave and Tidal Energy Conference (EWTEC 2007), Porto, Portugal.

Graw, K.U., Schimmels, S., Lengricht, J., 2000. Quantifying Losses Around the Lip of an OWC by Use of Particle Image Velocimetry (PIV). Presented at the Fourth European Wave

Energy Conference, LACER-Leipzig Annual Civil Engineering Report, Aalborg, Denmark.

Gray, C., Greated, C.A., 1988. The application of particle image velocimetry to the study of water waves. Optics and Lasers in Engineering 9, 265–276.

Greated C A, Emarat N, 2000. Optical Studies of Wave Kinematics, in: Liu P L F (Ed.), Advances in Coastal and Ocean Engineering, Volume 6. World Scientific.

Grue, J., Liu, P.L.F., Pedersen, G.K. (Eds.), 2004. PIV and water waves, Advances in coastal and ocean engineering. World Scientific, New Jersey, London.

Hals, J., 2010. Modelling and phase control of wave-energy converters (PhD thesis).

Hals, J., Falnes, J., Moan, T., 2011. A Comparison of Selected Strategies for Adaptive Control of Wave Energy Converters. Journal of Offshore Mechanics and Arctic Engineering 133, 031101.

Hong, K., Shin, S.-H., Hong, D.-C., Choi, H.-S., Hong, S.-W., 2007. Effects of Shape Parameters of OWC Chamber in Wave Energy Absorption, in: 17th 2007 International Offshore and Polar Engineering Conference, ISOPE 2007, July 01,2007 - July 06,2007, Proceedings of the International Offshore and Polar Engineering Conference. International Society of Offshore and Polar Engineers, Lisbon, Portugal, pp. 428–433.

Horko, M., 2007. CFD optimisation of an oscillating water column wave energy converter (Masters thesis).

Huang, Z.-C., Hsiao, S.-C., Hwung, H.-H., Chang, K.-A., 2009. Turbulence and energy dissipations of surf-zone spilling breakers. Coastal Engineering 56, 733–746.

Imai, Y., Toyota, K., Nagata, S., Setoguchi, T., Oda, J., Matsunaga, N., Shimozono, T., 2008. An Experimental Study of Negative Drift Force Acting on a Floating OWC "Backward Bent-duct Buoy", in: Proceedings of the ASME 27th International Conference on Offshore Mechanics and Arctic Engineering, June 15-20, 2008, Estoril, Portugal. Presented at the OMAE 2008, pp. 871–879.

International Energy Agency, 2008. World Energy Outlook 2008. Organisation for Economic Co-operation and Development (OECD).

ITTC, 2008a. Guide to the Expression of Uncertainty in Experimental Hydrodynamics, ITTC Guide 7.5-02-01-01, Revision 01, ITTC – Recommended Procedures and Guidelines.

ITTC, 2008b. Uncertainty Analysis: Particle Imaging Velocimetry, ITTC Procedure 7.5-01-03-03, ITTC – Recommended Procedures and Guidelines.

Jones, E., Oliphant, T., Peterson, P., others, 2001. SciPy: Open source scientific tools for Python.

Jung, K., Chang, K., Huang, E., 2005. Two-dimensional flow characteristics of wave interactions with a free-rolling rectangular structure. Ocean Engineering 32, 1–20.

Kimmoun, O., Branger, H., 2007. A particle image velocimetry investigation on laboratory surf-zone breaking waves over a sloping beach. J. Fluid Mech. 588.

Korde, U.A., 1991a. A power take-off mechanism for maximizing the performance of an oscillating water column wave energy device. Applied Ocean Research 13, 75–81.

Korde, U.A., 1991b. Development of a reactive control apparatus for a fixed two-dimensional oscillating water column wave energy device. Ocean Engineering 18, 465–483.

Korde, U.A., 2002. Active control in wave energy conversion. Sea Technology 43, 47.

Lam, K.M., Leung, M.Y.H.,Asymmetric vortex shedding flow past an inclined flat plate at high incidence. European Journal of Mechanics - B/Fluids 24, 33–48.

LaVision GmbH, 2009. Product-Manual for DaVis 7.2. LaVision GmbH, Göttingen, Germany.

Lavoie, P., Avallone, G., De Gregorio, F., Romano, G., Antonia, R., 2007. Spatial resolution of PIV for the measurement of turbulence. Experiments in Fluids 43, 39–51.

Longo, J., Shao, J., Irvine, M., Stern, F., 2007. Phase-Averaged PIV for the Nominal Wake of a Surface Ship in Regular Head Waves. J. Fluids Eng. 129, 524–540.

Longo, J., Stern, F., 2005. Uncertainty assessment for towing tank tests with example for surface combatant DTMB model 5415. Journal of ship research 49, 55–68.

McComb, W.D., 1991. The Physics of Fluid Turbulence, New ed. ed, Oxford engineering science series. Clarendon, Oxford.

Molyneux, D., Xu, J., Bose, N., 2007. Commissioning a stereoscopic particle image velocimeter system for application in a towing tank. Presented at the 28th American Towing Tank Conference.

Morrison, I.G., 1995. The Hydrodynamic Performance of an Oscillating Water Column Wave Energy Converter (PhD thesis).

Morrison, I.G., Greated, C.A., 1992. Oscillating Water Column Modelling, in: Proceedings of the Coastal Engineering Conference. pp. 502–511.

Mueller, M., Wallace, R., 2008. Enabling Science and Technology for Marine Renewable Energy. Energy Policy 36, 4376–4382.

Müller, G., Whittaker, T., 1995. Visualisation of Flow Conditions Inside a Shoreline Wave Power-Station. Ocean engineering 22, 629–641.

Muthanna, C., Stansberg, C.T., Baarholm, R., 2009. Experimental Study of the Local Wave Velocity Field During a Wave impact Occurrence, in: 28th International Conference on Offshore Mechanics and Arctic Engineering 2007, OMAE2009, May 31, 2009 - June 5, 2009, Proceedings of the International Conference on Offshore Mechanics and Arctic Engineering - OMAE. American Society of Mechanical Engineers, Honolulu, HI, United states.

Oliphant, T., Ascher, D., 2001. NumPy: Numerical Python. Lawrence Livermore National Laboratory, Livermore, California, USA. Available at: http://numpy.scipy.org/.

Osawa, H., Miyazaki, T., 2005. Technical manual for oscillating water column type wave power device, in: Proceedings of the International Offshore and Polar Engineering Conference. pp. 549–556.

Palmer, C., 2008. Wave Energy in the UK - The lessons of 30 Years, in: The Royal Institution of Naval Architects Marine Renewable Energy Conference 2008. London.

Price, A.A.E., Dent, C.J., Wallace, A.R., 2009. On the capture width of wave energy converters. Applied Ocean Research 31, 251–259.

Raffel, M., Wereley, S., Willert, C., Kompenhans, J., 2007. Particle image velocimetry : a practical guide, 2nd ed. Springer, Heidelberg, New York.

Van Rossum, G., Drake, F.L. (Eds.), 1995. Python reference manual. PythonLabs, Virginia, USA.

Ryu, Y., Chang, K.-A., Mercier, R., 2007. Runup and green water velocities due to breaking wave impinging and overtopping. Experiments in Fluids 43, 555–567.

Saarenrinne, P., Piirto, M., 2000. Turbulent kinetic energy dissipation rate estimation from PIV velocity vector fields. Experiments in Fluids 29, 300–307.

Sarmento, A., Brito-Melo, A., 1996. An Experiment-Based Time-Domain Mathematical Model of OWC Power Plants. International Journal of Offshore and Polar Engineering 6, 227–233.

Sheng, J., Meng, H., Fox, R.O., 2000. A large eddy PIV method for turbulence dissipation rate estimation. Chemical Engineering Science 55, 4423–4434.

Stagonas, D., Müller, G., 2007. Wave field mapping with particle image velocimetry. Ocean Engineering 34, 1781–1785.

Stappenbelt, B., Massimo, F., Cooper, P., Zhu, S.-P., Nader, J.-R., 2011. System Identification of a Floating Oscillating Water Column Wave Energy Converter, in: Proceedings of the ASME 2011 30th International Conference on Ocean, Offshore and Arctic Engineering. Presented at the OMAE 2011, Rotterdam, The Netherlands.

Sung, J., Yoo, J.Y., 2001. Three-dimensional phase averaging of time-resolved PIV measurement data. Measurement Science & Technology 12, 655–662.

Sveen, J.K., Cowen, E.A., 2004. Quantitative Imaging Techniques and Their Application to Wavy Flows, in: PIV and Water Waves. World Scientific.

Toyota, K., Nagata, S., Imai, Y., Setoguchi, T., 2009. Research for evaluating performance of OWC-type Wave Energy Converter "Backward Bent-duct Buoy", in: Proceeding of the 8th European Wave and Tidal Energy Conference. Presented at the 8th European Wave and Tidal Energy Conference, Uppsala, Sweden.

Turney, D.E., Anderer, A., Banerjee, S., 2009. A Method for Three-Dimensional Interfacial Particle Image Velocimetry (3D-IPIV) of an Air-Water Interface. Measurement Science and Technology 20.

Wallace, M.J., 2009. Twenty years of experimental and direct numerical simulation access to the velocity gradient tensor: What have we learned about turbulence? Physics of Fluids 21.

Warner, J.M., 1997. Wave energy conversion in a random sea (PhD thesis).

Waters, R., 2008. Energy from Ocean Waves, Full Scale Experimental Verification of a Wave Energy Converter (PhD).

Yavuz, H., McCabe, A., Aggidis, G., Widden, M.B., 2006. Calculation of the performance of resonant wave energy converters in real seas. Proceedings of the Institution of Mechanical Engineers, Part M: Journal of Engineering for the Maritime Environment 220, 117–128.

Zeff, B., Wolf, 2002. Three-dimensional dissipation scale measurements of turbulent flows (PhD thesis).

APPENDIX A

TYPE B UNCERTAINTY FOR 2D PIV MEASUREMENT SYSTEM

The principle values for the uncertainty analysis are presented here which was conducted in accordance with the ITTC guidelines (ITTC, 2008a) and the procedure for PIV uncertainty assessment (ITTC, 2008b). The data reduction equations $\left[f\left(x_{1,}\, x_2, x_3, \ldots, x_n\right)\right]$ and sensitivity coefficients $\left[c_i = \frac{\partial f}{\partial x_i}\right]$ are the same as those provided in (ITTC, 2008b). The first table (Principal dimensions of PIV measurement) lists the principal dimensions of the PIV setup, the second table (Summary of uncertainties for velocity $V_{(x,y)}$) is a summary of the uncertainties for velocities and the third table (Summary of uncertainties for velocity $V_{(x,y)}$) is a summary of the uncertainties for position and time.

Principal dimensions of PIV measurement

		Target Flow of Measurement	
Target flow		2-D water flow	
Measurement facility		AMC Towing tank (100m long, 3.5m wide, 1.5m deep)	
Measurement area		345 x 257	mm^2
Uniform flow speed		0.0	m/s
Max flow speed		0.5	m/s
		Calibration	
3rd order polynomial mapping			
	l_r	212	mm
	L_r	846	pixels
Magnification factor	α	0.25	mm/pixel
		Flow Visualisation	
Tracer particle		Spherical Carnauba	
Average diameter	d_p	0.13	mm
Standard deviation of diameter	s_p	0.06	mm
Average specific gravity		1.01	
Light source		Double pulse Nd:Yag Laser	
Laser power		120	mJ
Thickness of laser light sheet		6	mm
Time interval	Δt	15	ms
		Image Detection	
Camera			
Spatial resolution		1024 x1076	pixels
Sampling frequency		2.8 - 6.2	Hz
Gray scale resolution		12	bit
Cell size		6.45 x 6.45	micron
Optical System			
Distance from the target	l_t	1850	mm
Length of focus		35	mm
Aperture (f number of lens)		8	
Perspective angle	θ	7.916	deg
		Data Processing	
Image masking		Position C: above water surface from wave probe data	
		Position F: Manual masking per phase group (16 phases per wave)	
Image correction		3rd order polynomial mapping	
Image pre-processing		High Pass(64) + Subtract(10)	
Pixel unit analysis		Cross correlation method	
Multi pass mode		1x(64x64,50%), 2x(32x32,25%)	
Vector post-processing		Median filter (5)	
		Fill missing	
		Smoothing	

Summary of uncertainties for velocity $V_{(x,y)}$

Parameter	Category	Error sources	$u(x_i)$	(unit)	c_i	(unit)	$c_i u_i(x_i)$	u_c
α (mm/pix)	Calibration	Reference image	0.7	(pix)	2.96E-04	(mm/pix^2)	2.07E-04	
		Physical distance	0.5	(mm)	0.001182	(1/pix)	5.91E-04	
		Image distortion by lens	4.11	(pix)	2.96E-04	(mm/pix^2)	1.22E-03	
		Image distortion by CCD	0.0056	(pix)	2.96E-04	(mm/pix^2)	1.66E-06	
		Board position	2.0	(mm)	1.35E-04	(1/pix)	2.71E-04	
		Parallel board	0.035	(rad)	8.77E-03	(mm/pix)	3.07E-04	0.00143
ΔX (pix)	Acquisition	Laser power fluctuation	0.0056	(mm)	4.0	(pix/mm)	2.24E-02	
		Image distortion by CCD	0.0056	(pix)	1.0		5.60E-03	
		Normal view angle	0.035	(rad)	0.008747	(mm/pix)	3.06E-04	
	Reduction	Mis-matching error	0.2	(pix)	1.0		2.00E-01	
		Sub-pixel analysis	0.03	(pix)	1.0		3.00E-02	0.20355
Δt (s)	Acquisition	Delay generator	2.00E-09	(s)	1.0		2.00E-09	
		Pulse generator	5.00E-09	(s)	1.0		5.00E-09	5.39E-09
δu (mm/s)	Experiment	Particle trajectory	0.05	(mm/s)	1.0		5.00E-02	
		3-D effects	0.346	(mm/s)	1.0		3.46E-01	0.350

Parameter	Category	Error sources	$u(x_i)$	unit	c_i	unit	$c_i u_i(x_i)$	(unit)
α		Magnification factor	0.00143	(mm/pix)	2000.0	(pix/s)	2.86	
ΔX		Image displacement	0.20355	(pix)	16.7	(mm/pix/s)	3.39	
Δt		Image interval	5.39E-09	(s)	33333	(mm/s^2)	0.00	
δu		Experiment	0.350	(mm/s)	1		0.35	
		Combined uncertainty	u_u				**4.45**	**(mm/s)**

Summary of uncertainties for position and time

Parameter	Category	Error sources	$u(x_i)$	(unit)	c_i	(unit)	$c_i u_i(x_i)$	(unit)
X_s, X_e	Acquisition	Digital error	0.5	(pix)	0.25	(pix/mm)	0.125	
		Non-uniformity of distribution	8.0	(pix)	0.25	(pix/mm)	2	
	Calibration	Origin correlation	6	(pix)	0.25	(pix/mm)	1.5	
		Magnification factor	0.001429	(mm/pix)	846	(pix)	1.2089242	
			Combined uncertainty	u_x			2.78	(mm)

Parameter	Category	Error sources	$u(x_i)$	(unit)	c_i	(unit)	$c_i u_i(x_i)$	(unit)
t_s, t_e	Acquisition	Delay generator	2.00E-09	(s)	1		2.00E-09	
		Pulse time	5.00E-09	(s)	1		5.00E-09	
			Combined uncertainty	u_t			5.39E-09	(s)

APPENDIX B

PHASE-AVERAGED VELOCITY FIELDS OVER ONE WAVE CYCLE

This appendix presents the phase-averaged velocity fields for all four experimental wave conditions tested (f=0.44, 0.50 0.57 and 0.77Hz all at H=0.07m). Phase-averaging was performed using the hybrid ensemble-averaging algorithm described in Chapter 5 on all available velocity fields and any overlaps velocity fields (where available) with the following parameters: $\mathrm{nmin} = 7$ and $\mathrm{s} = \mathrm{None}$ (as described in Chapter 5). The velocity fields from different positions were merged using the technique described in Chapter 4. Only 1/8 of the available vectors are shown for clarity.

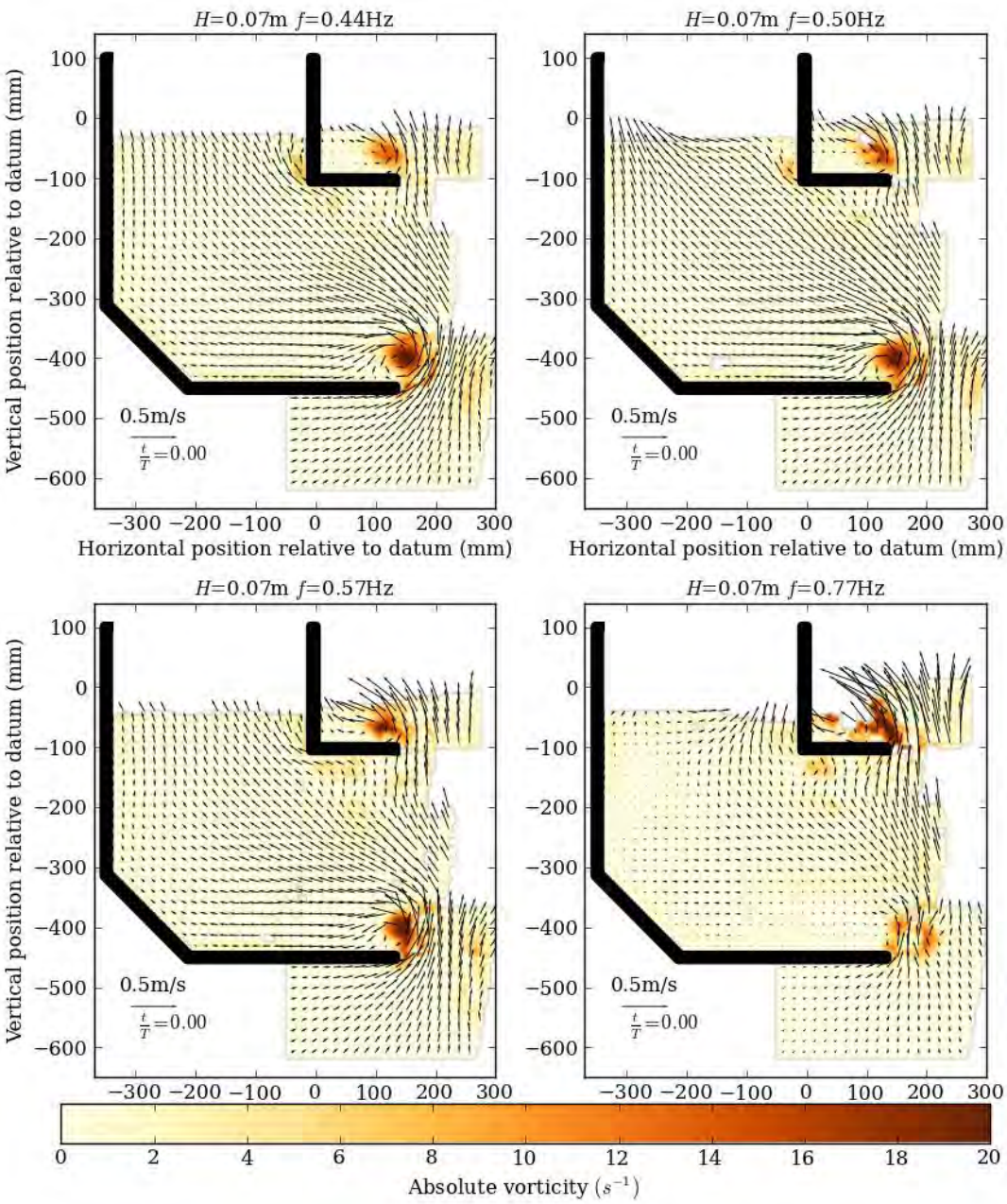
H=0.07m f=0.44Hz
H=0.07m f=0.50Hz
H=0.07m f=0.57Hz
H=0.07m f=0.77Hz
Vertical position relative to datum (mm)
Horizontal position relative to datum (mm)
0.5m/s
t/T=0.00
Absolute vorticity (s^-1)

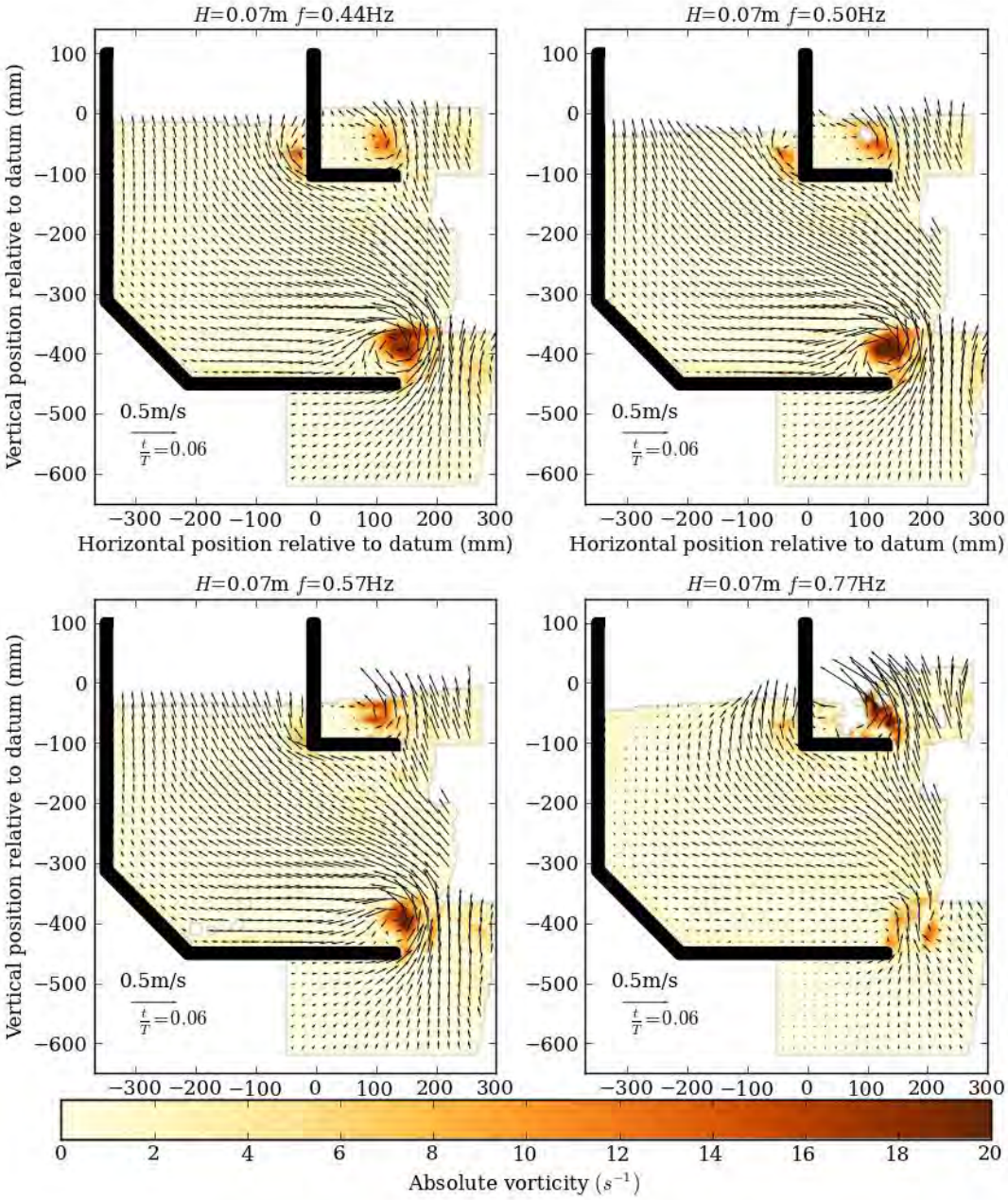
H=0.07m f=0.44Hz
H=0.07m f=0.50Hz
H=0.07m f=0.57Hz
H=0.07m f=0.77Hz
Vertical position relative to datum (mm)
Horizontal position relative to datum (mm)
0.5m/s
t/T=0.06
Absolute vorticity (s^-1)

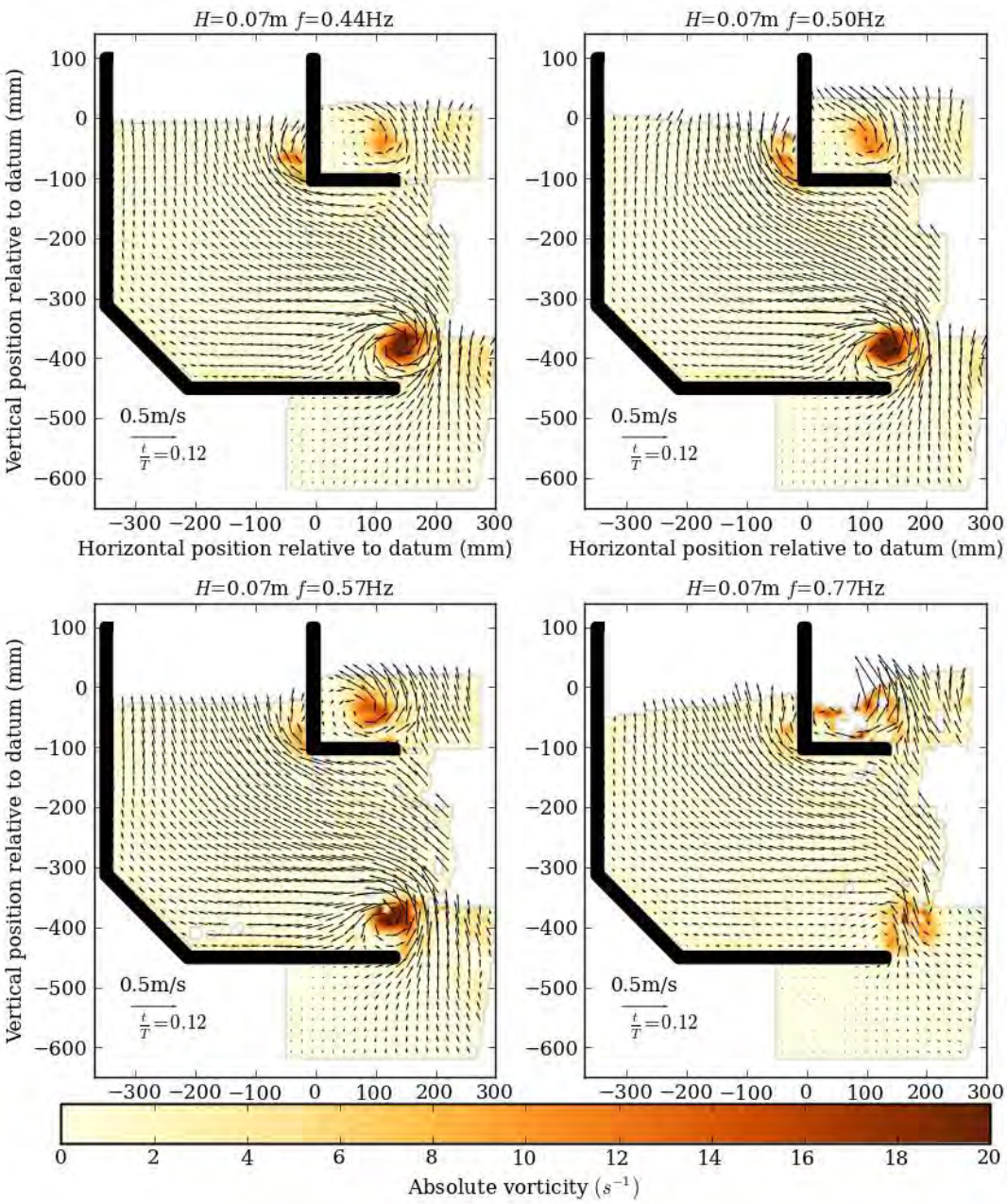
H=0.07m f=0.44Hz
H=0.07m f=0.50Hz
H=0.07m f=0.57Hz
H=0.07m f=0.77Hz
Vertical position relative to datum (mm)
Horizontal position relative to datum (mm)
0.5m/s
t/T=0.12
Absolute vorticity (s^-1)

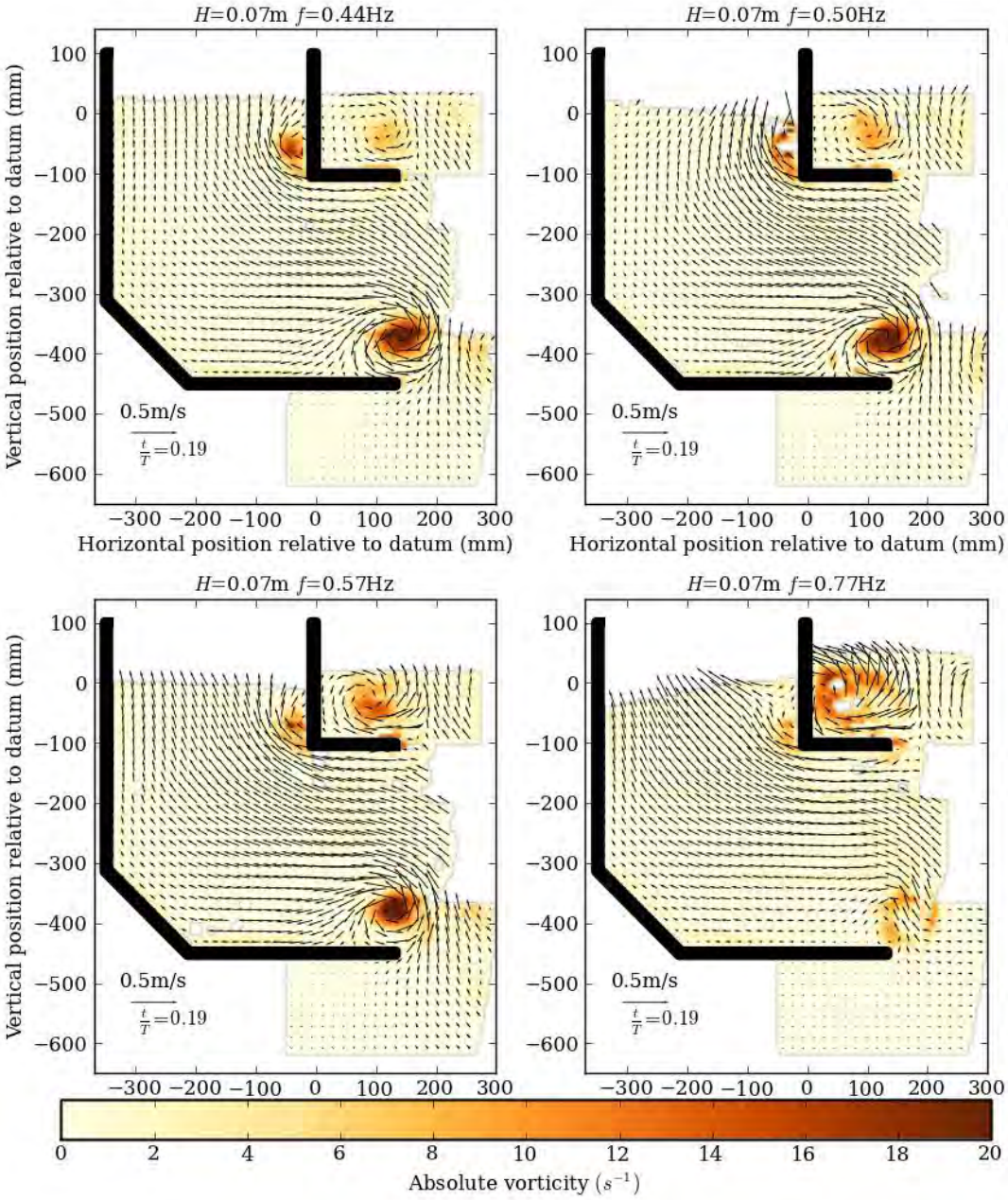
H=0.07m f=0.44Hz
H=0.07m f=0.50Hz
H=0.07m f=0.57Hz
H=0.07m f=0.77Hz
Vertical position relative to datum (mm)
Horizontal position relative to datum (mm)
0.5m/s
t/T=0.19
Absolute vorticity (s^-1)

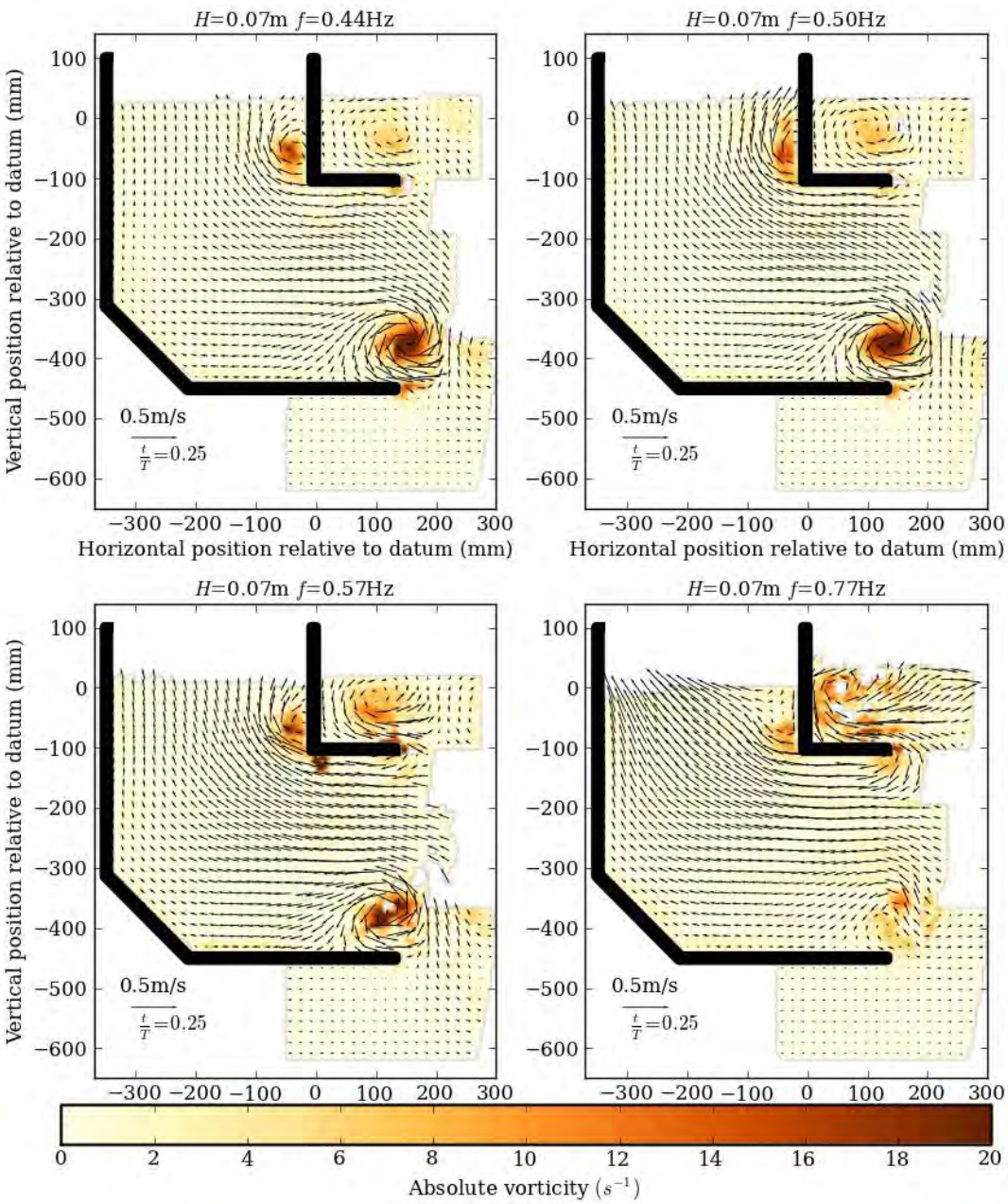
H=0.07m f=0.44Hz
H=0.07m f=0.50Hz
H=0.07m f=0.57Hz
H=0.07m f=0.77Hz
Vertical position relative to datum (mm)
Horizontal position relative to datum (mm)
0.5m/s
t/T=0.25
Absolute vorticity (s^-1)

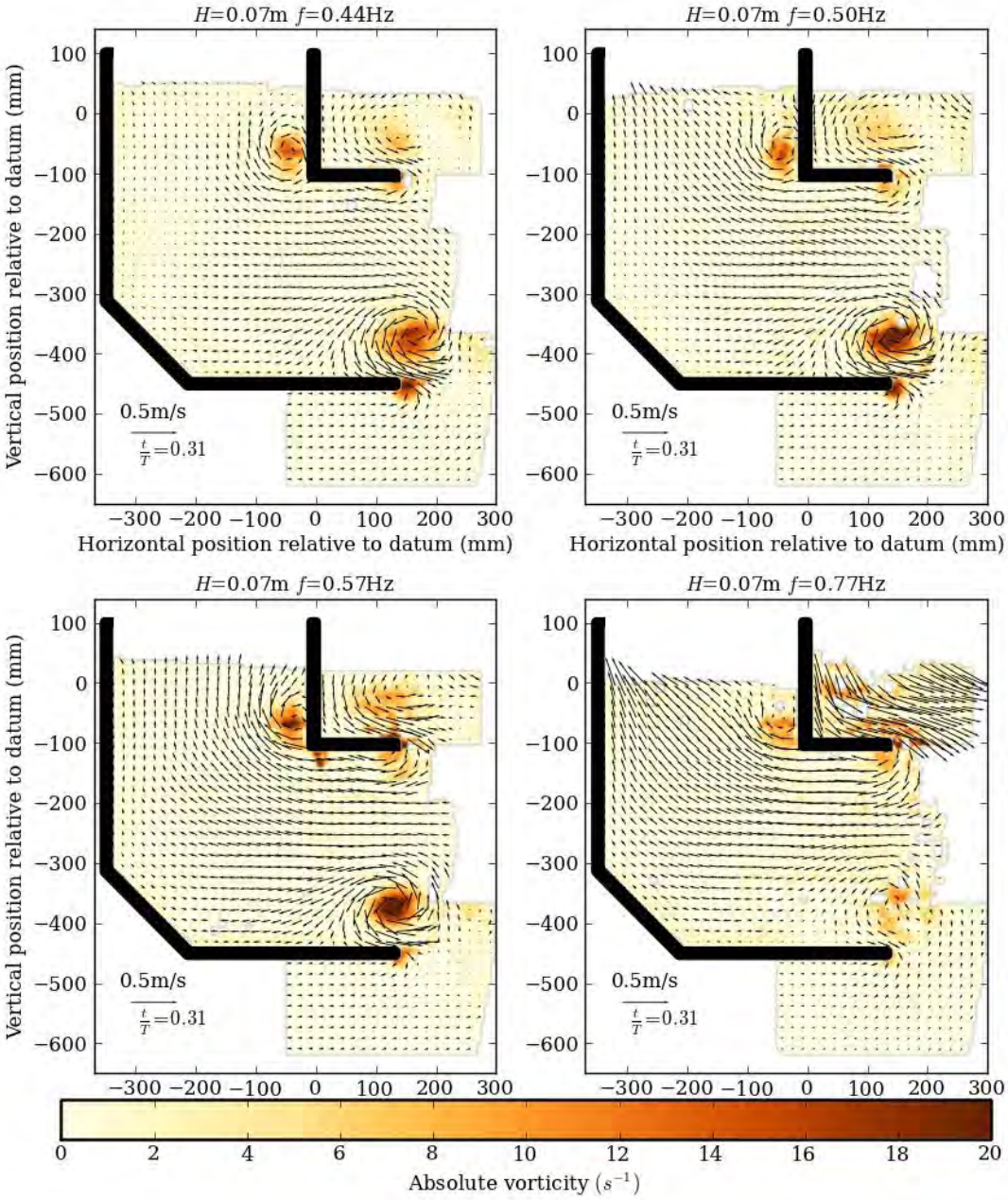
H=0.07m f=0.44Hz
H=0.07m f=0.50Hz
H=0.07m f=0.57Hz
H=0.07m f=0.77Hz
Vertical position relative to datum (mm)
Horizontal position relative to datum (mm)
0.5m/s
t/T=0.31
Absolute vorticity (s^-1)

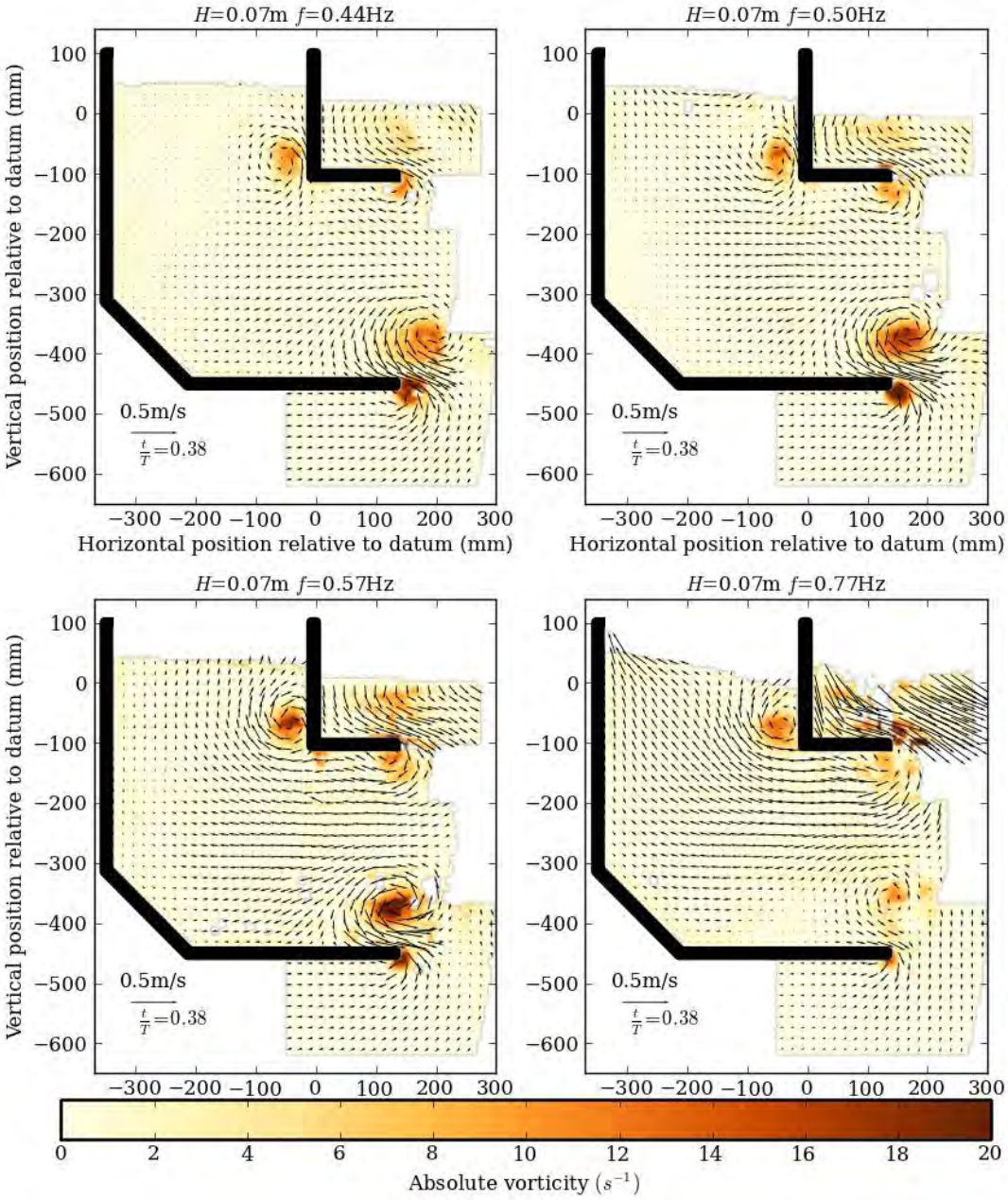
H=0.07m f=0.44Hz
H=0.07m f=0.50Hz
H=0.07m f=0.57Hz
H=0.07m f=0.77Hz
Vertical position relative to datum (mm)
Horizontal position relative to datum (mm)
0.5m/s
t/T=0.38
Absolute vorticity (s^-1)

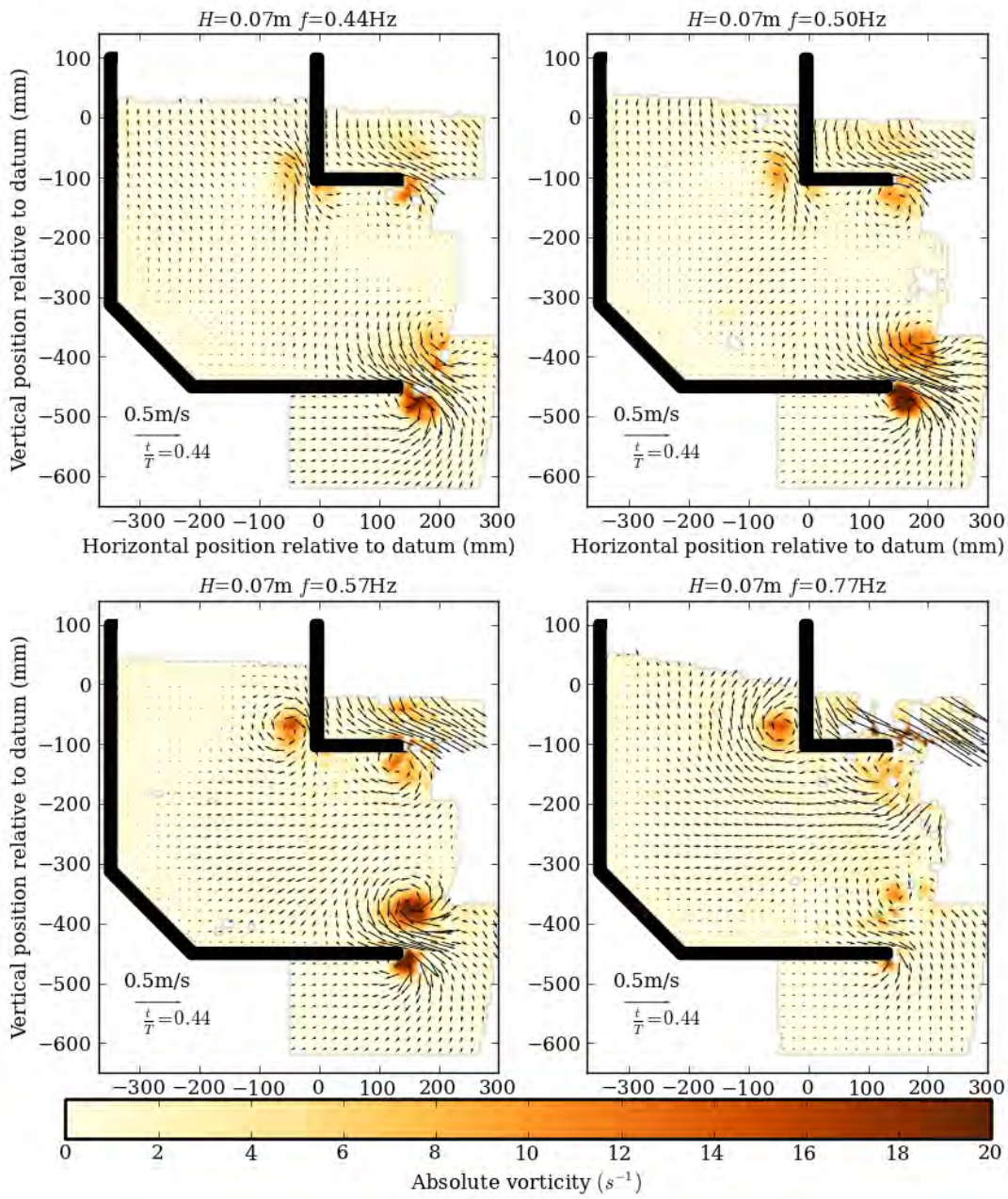
H=0.07m f=0.44Hz
H=0.07m f=0.50Hz
H=0.07m f=0.57Hz
H=0.07m f=0.77Hz
Vertical position relative to datum (mm)
Horizontal position relative to datum (mm)
0.5m/s
t/T=0.44
Absolute vorticity (s^-1)

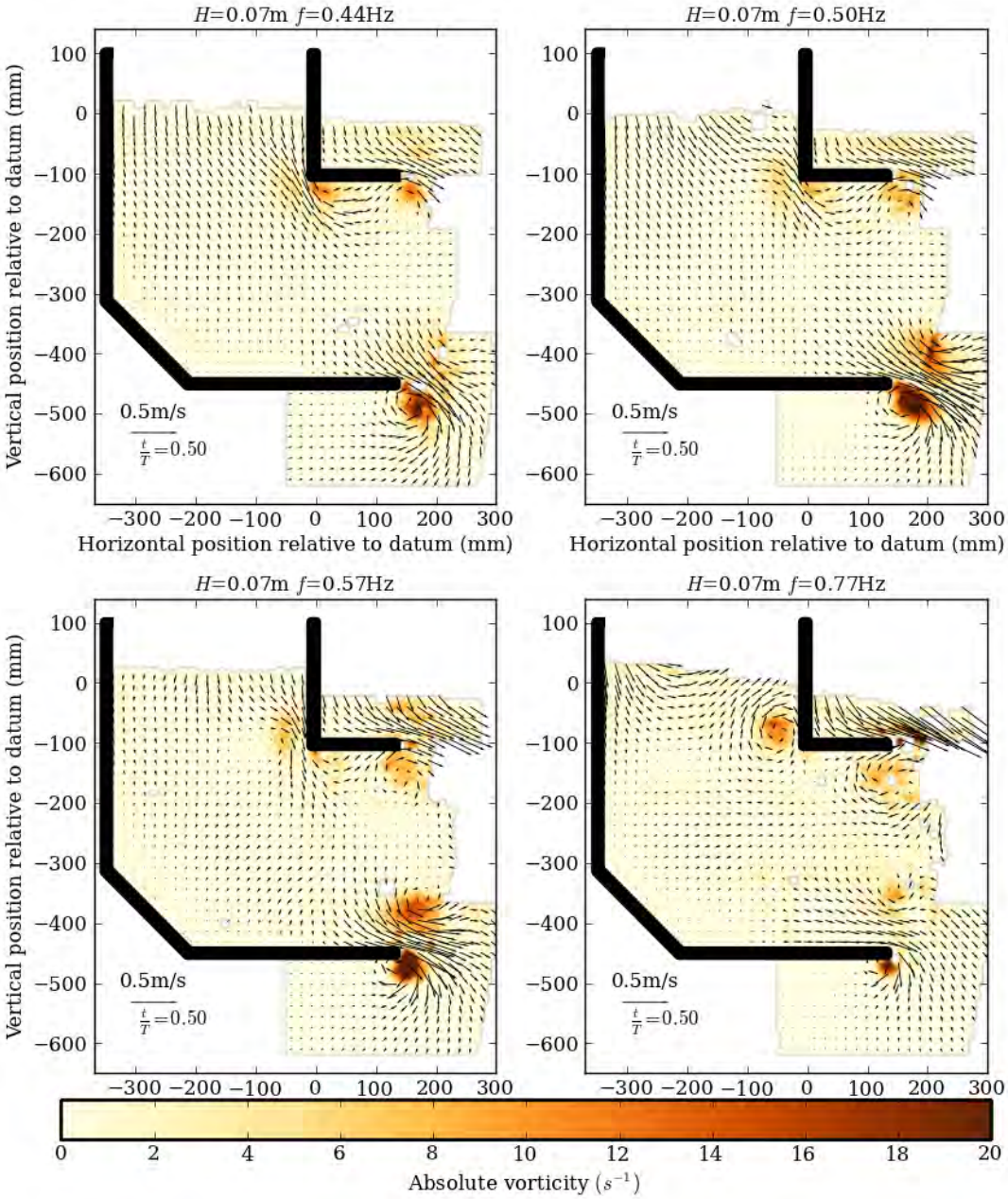
H=0.07m f=0.44Hz
H=0.07m f=0.50Hz
H=0.07m f=0.57Hz
H=0.07m f=0.77Hz
Vertical position relative to datum (mm)
Horizontal position relative to datum (mm)
0.5m/s
t/T=0.50
Absolute vorticity (s^-1)

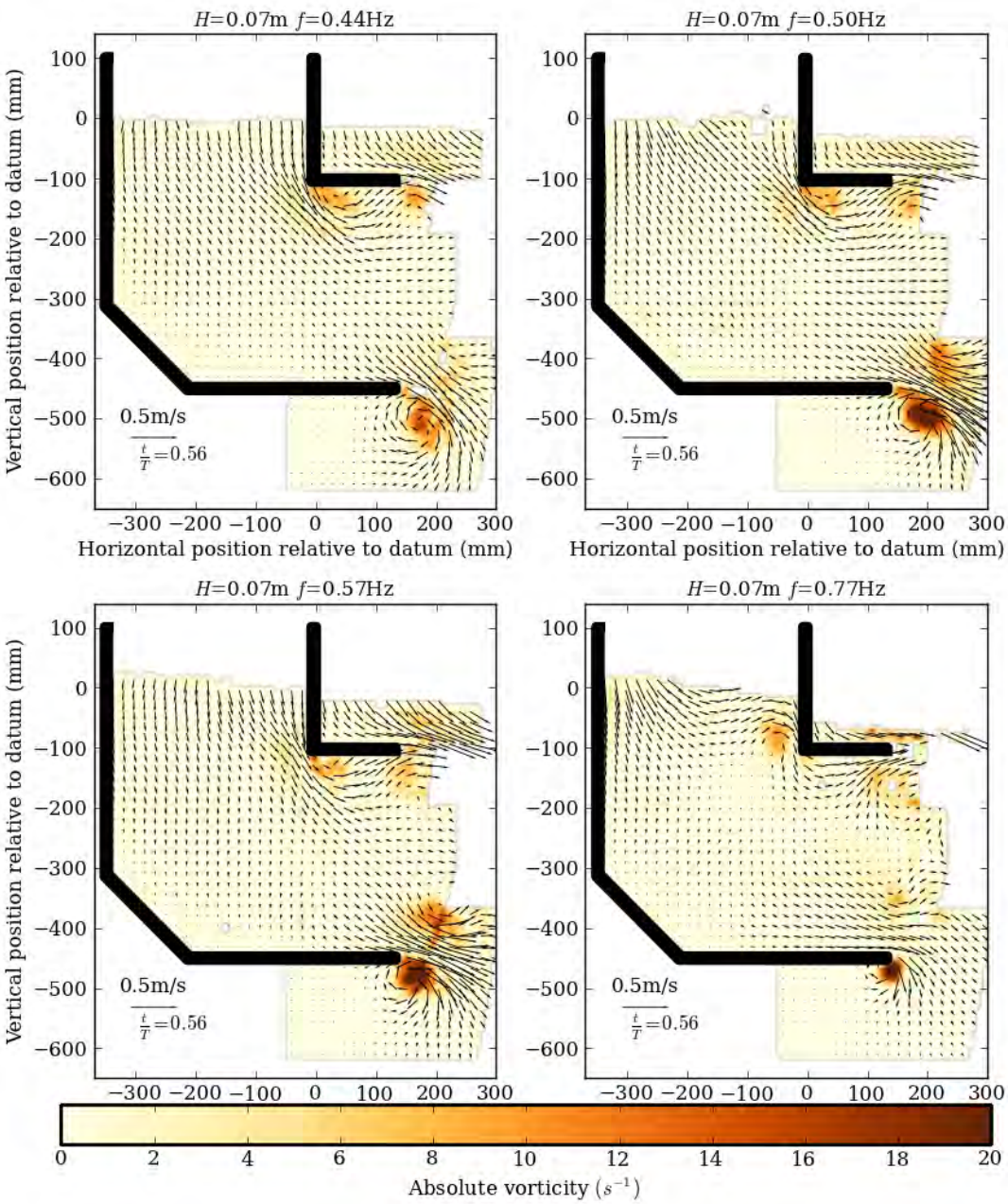
H=0.07m f=0.44Hz
H=0.07m f=0.50Hz
H=0.07m f=0.57Hz
H=0.07m f=0.77Hz
Vertical position relative to datum (mm)
Horizontal position relative to datum (mm)
0.5m/s
t/T=0.56
Absolute vorticity (s^-1)

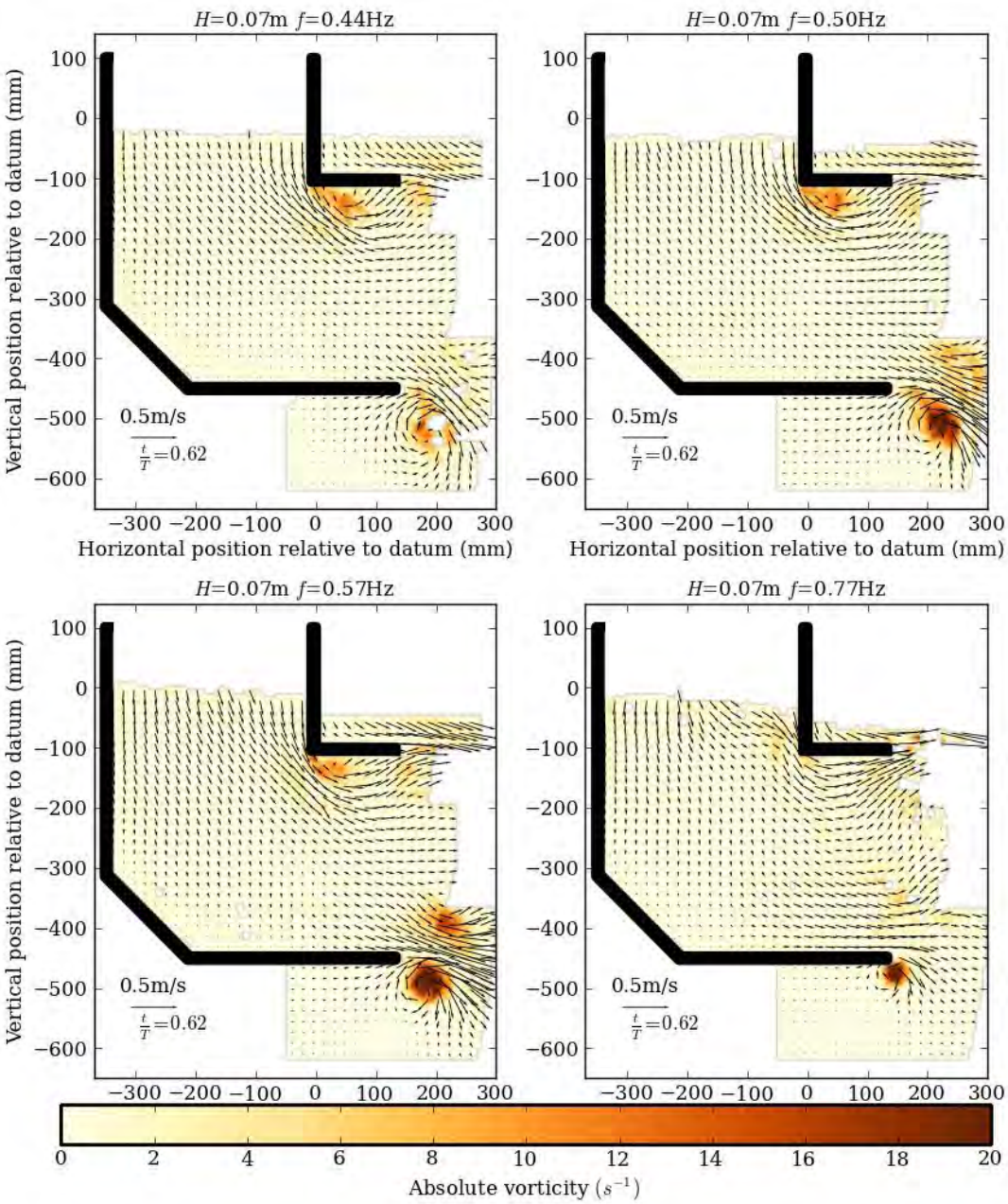
H=0.07m f=0.44Hz
H=0.07m f=0.50Hz
H=0.07m f=0.57Hz
H=0.07m f=0.77Hz
Vertical position relative to datum (mm)
Horizontal position relative to datum (mm)
0.5m/s
t/T=0.62
Absolute vorticity (s^-1)

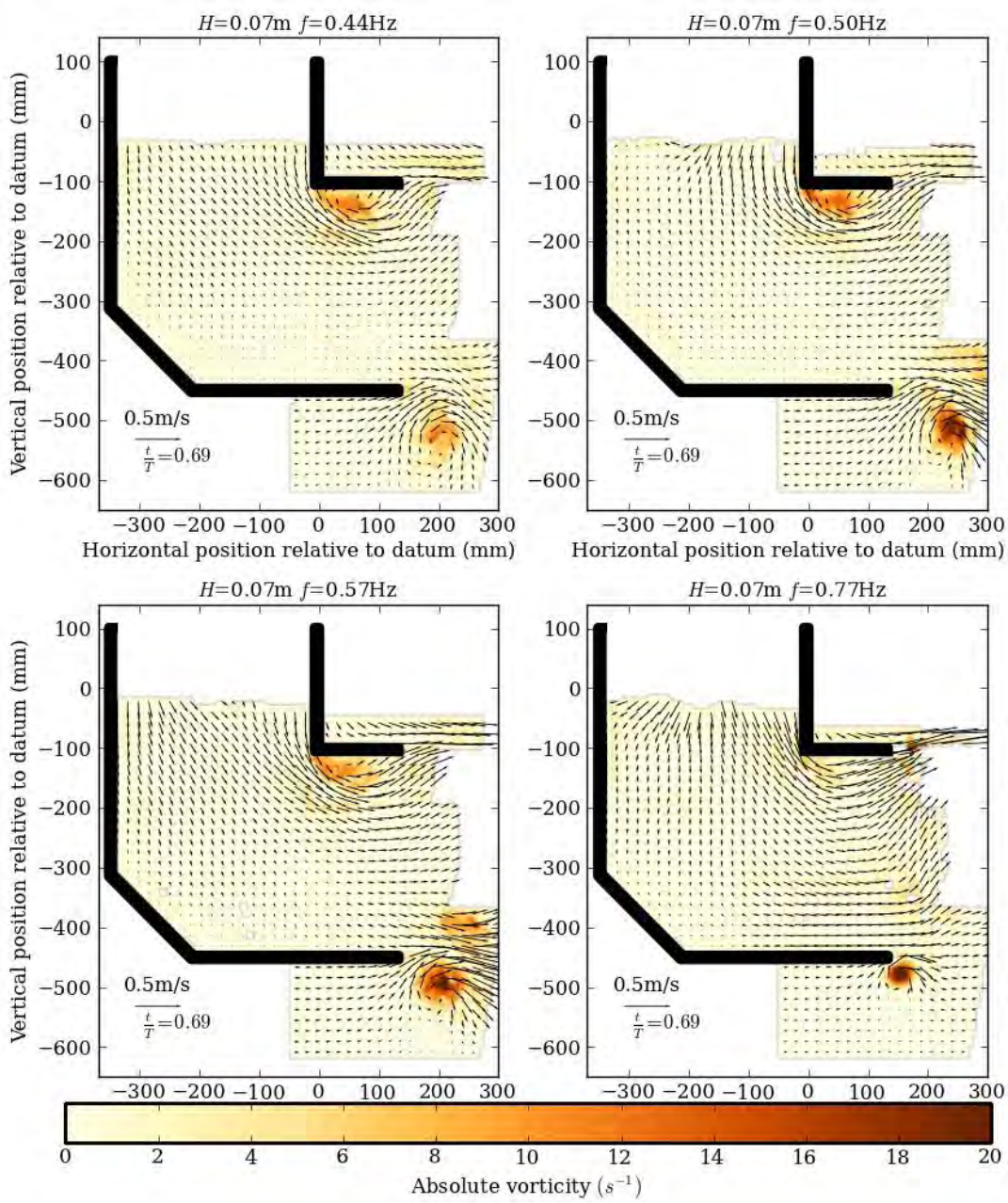
H=0.07m f=0.44Hz
H=0.07m f=0.50Hz
H=0.07m f=0.57Hz
H=0.07m f=0.77Hz
Vertical position relative to datum (mm)
Horizontal position relative to datum (mm)
0.5m/s
t/T=0.69
Absolute vorticity (s^-1)

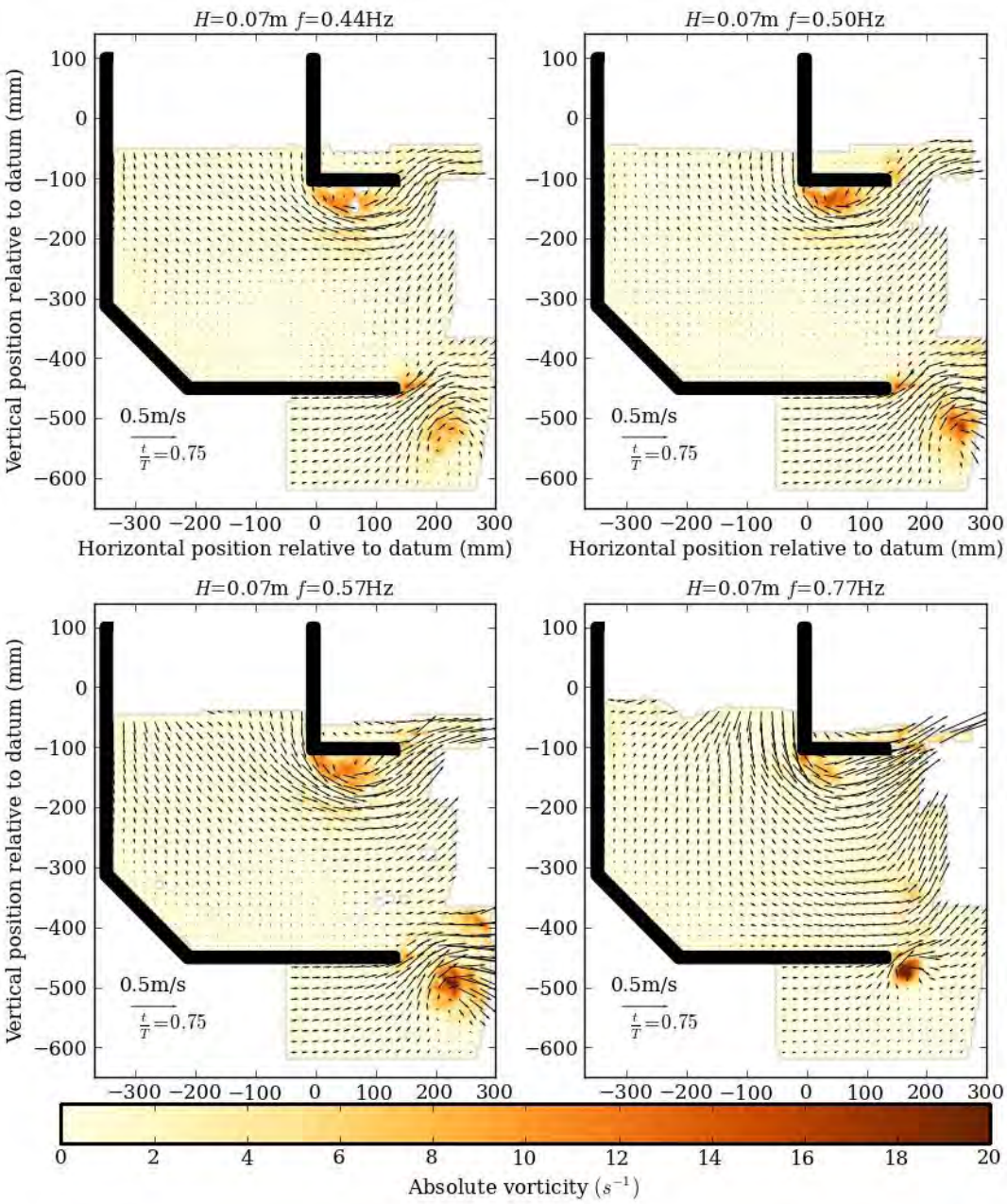
H=0.07m f=0.44Hz
H=0.07m f=0.50Hz
H=0.07m f=0.57Hz
H=0.07m f=0.77Hz
Vertical position relative to datum (mm)
Horizontal position relative to datum (mm)
0.5m/s
t/T=0.75
Absolute vorticity (s^-1)

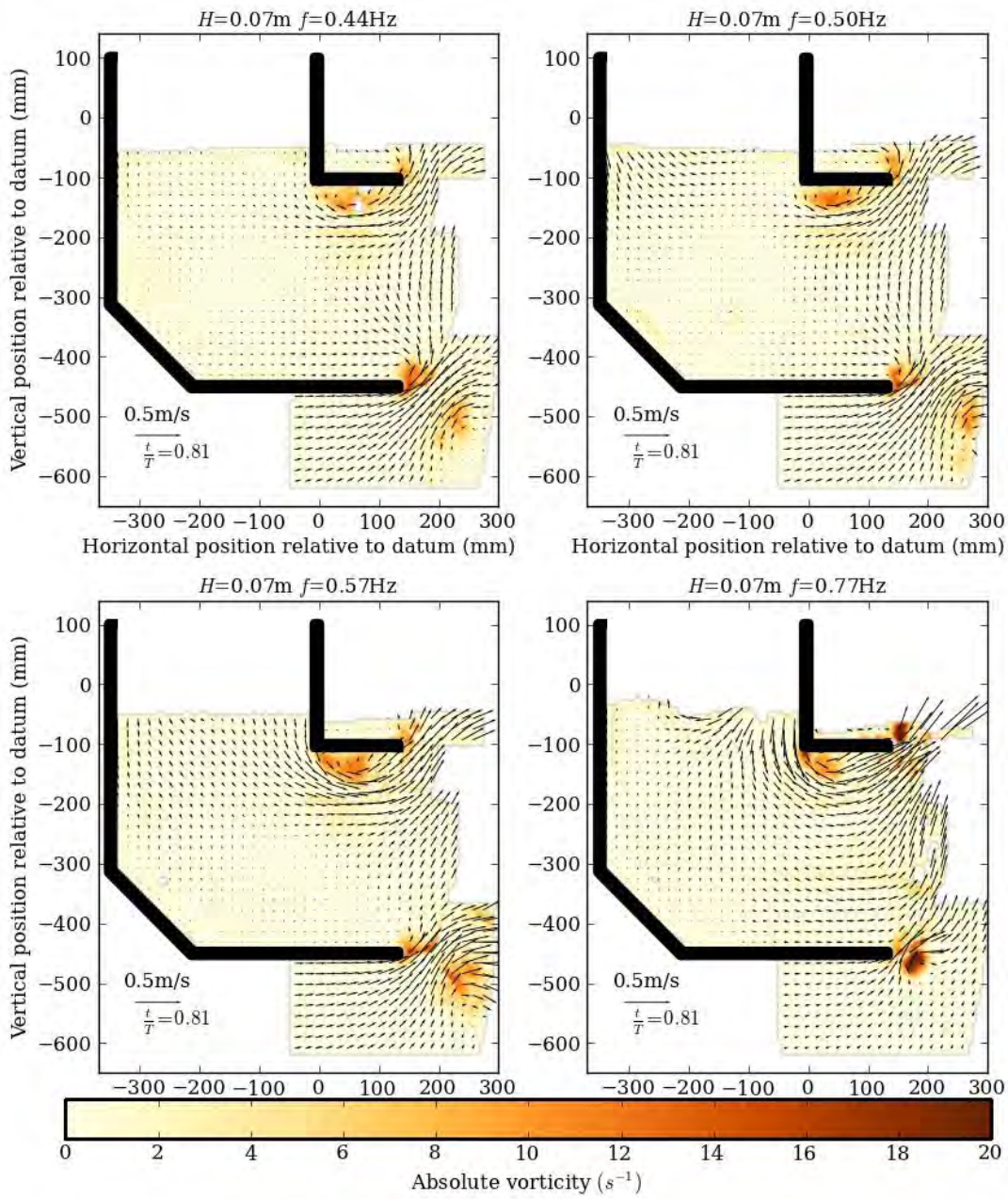
H=0.07m f=0.44Hz
H=0.07m f=0.50Hz
H=0.07m f=0.57Hz
H=0.07m f=0.77Hz
Vertical position relative to datum (mm)
Horizontal position relative to datum (mm)
0.5m/s
t/T=0.81
Absolute vorticity (s^-1)

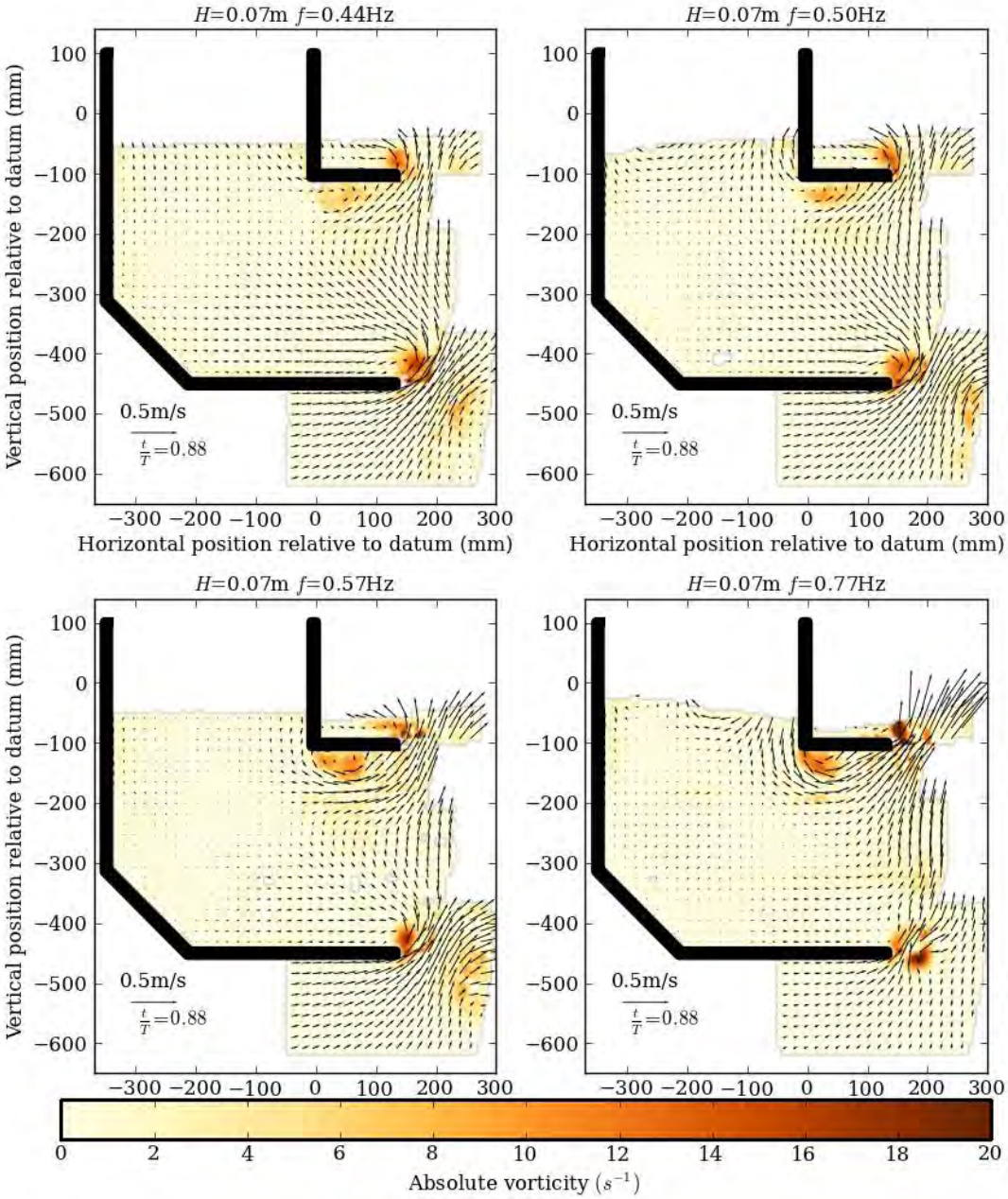
H=0.07m f=0.44Hz
H=0.07m f=0.50Hz
H=0.07m f=0.57Hz
H=0.07m f=0.77Hz
Vertical position relative to datum (mm)
Horizontal position relative to datum (mm)
0.5m/s
t/T=0.88
Absolute vorticity (s^-1)

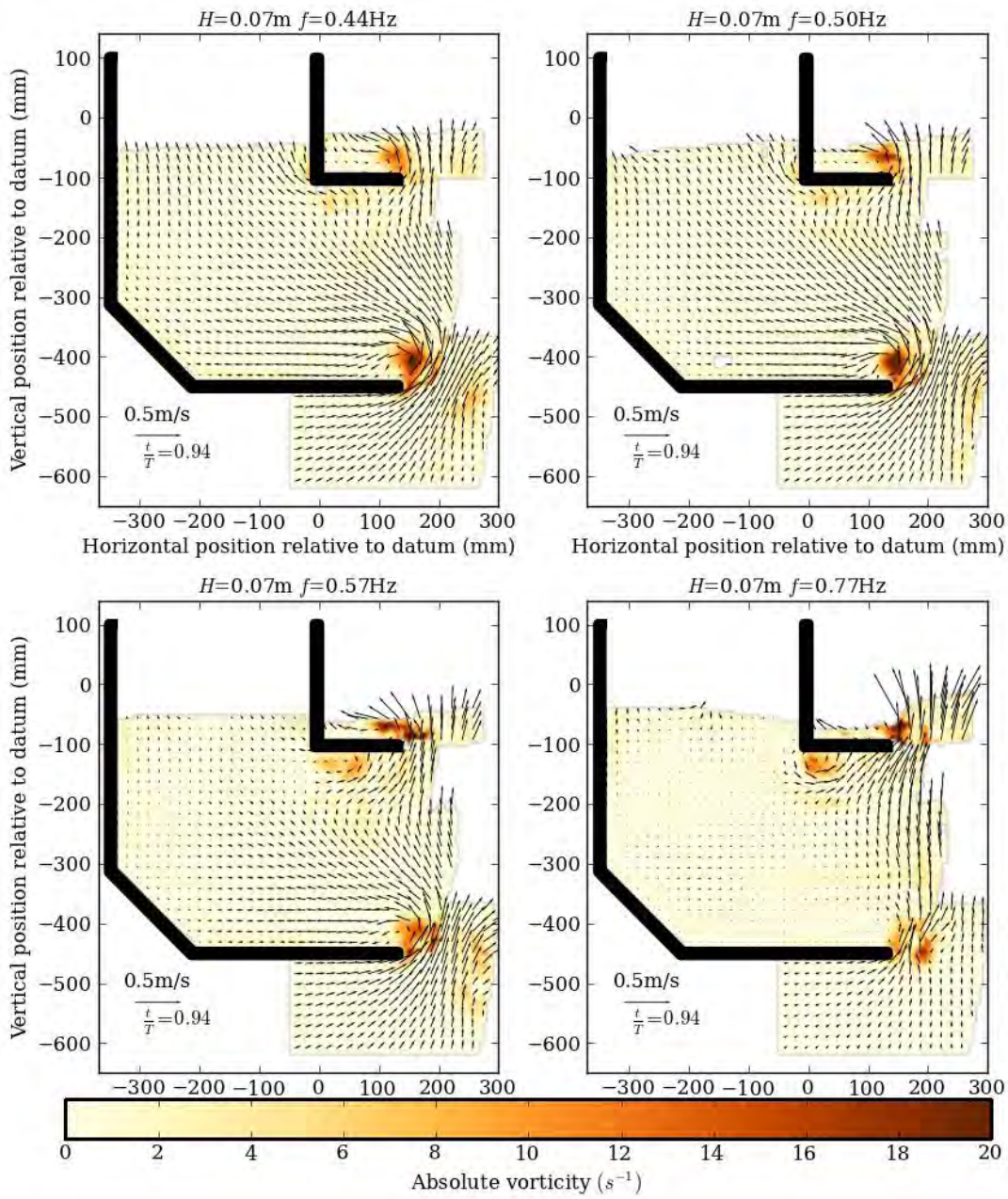
H=0.07m f=0.44Hz
H=0.07m f=0.50Hz
H=0.07m f=0.57Hz
H=0.07m f=0.77Hz
Vertical position relative to datum (mm)
Horizontal position relative to datum (mm)
0.5m/s
t/T=0.94
Absolute vorticity (s^-1)

[Page intentionally left blank]